UNIVERSITÀ DEGLI STUDI DI TRIESTE

UNIVERSITÀ DEGLI STUDI DI TRIESTE

XXXV Ciclo del Dottorato di Ricerca in
Fisica

Magnetic configuration at ferromagnet-semiconductor interfaces: static and dynamic studies

Settore scientifico-disciplinare: FIS03 FISICA DELLA MATERIA

Dottorando:
Simone Laterza

Coordinatore:
Prof. Francesco Longo

Supervisore di tesi:
Dott. Marco Malvestuto

"[...] I invented a word. It was called POETRY. I don't know what it is, but I like it."

David Mycroft, *Next wave three*, 1971

Abstract

This doctoral research investigates the captivating realm of metal/semiconductor heterostructures, with a focus on the manipulation and transport of electron spin in solid-state systems for potential application in Spintronics. At the heart of this study lies a Ni/Si heterostructure, which is explored through ultrafast demagnetization, unveiling the dynamics of spin-polarized superdiffusive currents.

The development of a suitable Ni/Si heterostructure has been the first step to build the scientific case of the generation of a laser-induced spin-polarized superdiffusive current and its propagation in a solid, with the experimental conditions that demanded the realization of an EUV polarimeter for detecting the reflected beam polarization. The thesis investigates magnetodynamics at both the Ni $M_{2,3}$ and Si $L_{2,3}$ absorption edges, revealing an effective spin current propagation velocity of 0.2 nm/fs, supporting theoretical predictions.

A significant observation was the presence of an equilibrium magnetization state in the proximal silicon layer of the Ni/Si heterostructure, which was unanticipated due to silicon's weakly diamagnetic nature. A systematic analysis, using samples with varying semiconductor dopings and applying the static XMCD technique, demonstrated a complex interplay at the interface.

The implications of this study are momentous for Spintronics, particularly because of the verified magnetic coupling between the ferromagnetic layer and the underlying semiconductor. The results of this study represent an important step in advancing silicon-based spintronic systems and pave the way for the design of energy-efficient and faster electronic devices leveraging the spin degree of an electron.

Contents

IV

Introduction

Metal/semiconductor heterostructures are intriguing systems due to the possibility to integrate optical, magnetic and electric properties in the same device. These systems have been extensively studied as they contribute significantly to the current CMOS technology. However, in more recent years, a renewed interest has risen as they still offer attracting insights on both fundamental and applied physics due to the increased ability to tailor their properties *ad libitum*. Lately, effort has been devoted to further expand their capabilities in the realm of spintronic devices.

The integration of magnetic properties into silicon-based materials has been a long-standing goal in the field of Spintronics. Spintronics, or SPIN TRansport electrONICS, involves the study of the detection, control, manipulation and transport of the spin degree of freedom in solid-state systems. Spin is a peculiar quantity that allows both improvements on charge-based electronics and novel computing possibilities. In fact, the potential of adding the spin degree of freedom of an electron in charge-based devices is the development of more energy-efficient and faster electronic devices. Furthermore, spin currents - the spintronic equivalent of electrical currents - are suggested to flow with almost no dissipation [1, 2], while spin coherence time is larger than the charge confinement lifetime [3]. However, due to the inherently non-magnetic nature of silicon, the realization of silicon-based spintronic systems has been hampered to date. Nonetheless, recent experimental and theoretical advancements have opened new avenues to induce and control magnetic properties in silicon, preparing the ground for a new generation of spintronic devices. In any spintronic device the generation and transport of a spin current is fundamental. Silicon is worthy of attention, as it features an efficient spin transport because of the small spin–orbit interaction, the reduced nuclear spin, and the crystal inversion symmetry [2, 4, 5]. However, we are left with the problem of generating spin currents in silicon.

This thesis falls in part within the field of ultrafast demagnetization, as the mechanism employed to generate spin currents in silicon involves the

demagnetization of a magnetic thin film. In his seminal work, Battiato outlined the superdiffusive spin currents as a competing mechanism involved in the ultrafast demagnetization [6]. In this picture, the excitation from an ultrafast pulse in a ferromagnet can trigger a superdiffusive or ballistic motion that displaces spin-polarized electrons and thus subtracts spin moment locally. The electrons that have been displaced maintain their spin polarization, thereby facilitating their propagation as spin currents. This model has been put forward as an effective method of injecting spin currents. It is interesting the possibility to inject spins from a thin nickel film into silicon [7], a mechanism which has been posited to be chargeless, boasting up to 80% spin polarization, and possessing an ultra-short duration. This finding is especially remarkable given that spin injection at interfaces has long posed significant challenges. Indeed, originally, the problem was presumed to be insurmountable due to the so-called conductivity-mismatch problem [8] which capped the maximum attainable induced spin polarization in the semiconductor at a mere 0.1%. The issue of the vast difference in conductivity between metal and semiconductor was ultimately addressed by introducing a tunnel barrier at the interface, thereby facilitating efficient spin injection in the diffusive regime [9, 10].

As could be anticipated, the presence of defects and other structural anomalies at the interface is likely to impede the spin injection mechanism, making it necessary to devote part of the experimental verification task to the creation of a system with minimal defects. Regrettably, it is a well-established fact that nickel, when deposited on silicon, forms a nickel silicide alloy even at room temperature [11, 12], which implies the need to develop a barrier that is resistant to diffusion. The nitridation process on the Si (111) surface, which forms a crystalline bilayer of Si_3N_4 via a self-terminating reaction [13, 14], has been chosen as a passivating procedure. As a corollary, the subsequent low-temperature epitaxial deposition of a metallic layer ensue without any incursion of metal-silicon intermixing [15]. Consequently, we utilized a $Ag(2nm)/Ni(7nm)/Si_3N_4/Si$ heterostructure as our case-study system. Subsequent characterization of the developed samples through transmission electron microscopy unveiled the presence of some discontinuous silicide areas just beneath the nitride layer [16], presumably as a result of thermal strain-induced microfractures during the low-temperature nickel deposition.

In respect to Battiato's work, under the assumption that an ultrafast optical excitation could generate a spin-polarized superdiffusive current, the propagation of the displaced electrons into the substrate was investigated in a nickel/silicon heterostructure. The empirical validation of the spin injection

presents a considerable challenge from various perspectives. The superdiffusive current is generated synchronously with the ultrafast optical excitation and then undergoes ballistic diffusion at a mean velocity of 0.5 nm/fs, an order of magnitude greater than its sound velocity. Secondly, we are compelled to scrutinize the inner layers of the system, and the probe must be capable of selectively resolving the dynamics both within the metallic layer and the semiconductor, demanding the application of resonant spectroscopy techniques. Lastly, it is vital for the probe to be sensitive to magnetic variations. The FERMI FEL2 laser source [17] meets all these requirements, as it provides ultrashort polarized EUV pulses in an energy range that covers the Ni $M_{2,3}$ and Si $L_{2,3}$ absorption edges. To acquire magnetic sensitivity we decided to employ a time-resolved resonant MOKE technique, for which a suitable detection device had to be developed. Accordingly, none of the time-resolved measurements that can be found in this thesis could be achieved without the design, construction and characterization of an EUV polarimeter [18, 19] to reconstruct the reflected beam polarization.

At the heart of this thesis lies the evaluation of a time-resolved resonant Magneto-Optic Kerr Effect (MOKE) signal within both metal and semiconductor subsystems [20]. The distinct magnetodynamics observed at the nickel (Ni) $M_{2,3}$ and silicon (Si) $L_{2,3}$ absorption edges indicate that upon the arrival of the pump, Ni demagnetization initiates the emergence and subsequent propagation of a spin-polarized superdiffusive current, as can be discerned from the variable magnetic signals at these two edges.

Specifically, the magnetization dynamics of the substrate are decelerated as its demagnetization competes with the transient spin current injection from the metal. Then, over an extended temporal scale, following the propagation of the spin current pulse within the substrate, the observed contribution progressively diminishes in significance. Consequently, we deduced the spin current propagation velocity to be 0.2 nm/fs, an estimation that aligns with theoretical predictions proposed for the ideal Ni/Si system.

Through the accurate decoupling of the magnetodynamic response of the Si support from the Ni overlayer, we interpret these results as an experimental confirmation of photoinduced spin currents.

The magnetic dynamics displayed by the Ni/Si heterostructure revealed an equilibrium state that was non-trivial to address. Surprisingly, the static magnetization in the proximal silicon layer was non-zero, notwithstanding the expectation of silicon exhibiting weak diamagnetism. In response to this unforeseen result, we not only sought to replicate the dynamic studies on slightly varied samples but also investigated the behavior of the proximal silicon layer using the static XMCD technique.

Given that the magnetic field engendered by the ferromagnetic film was likely to induce the static magnetization within the semiconductor substrate via proximity effects, we contemplated the implications of altering the semiconductor substrate's doping. Indeed, as the Ni/Si device essentially constitutes a Schottky barrier, modifying the doping consequently transformed the depletion layer, presumed to be the residence of spin-polarized silicon electrons.

Notably, the observed magnetic dichroic signal of silicon was found to be inverse for the two different dopings, suggesting a more intricate behavior of the heterostructure at the interface. Despite this complexity, the study offered unequivocal evidence of the presence of a direct magnetic coupling between the ferromagnetic layer and the underlying semiconductor, holding significant implications for the burgeoning field of Spintronics.

This thesis is divided into seven chapters. The second chapter provides the theoretical background to the the main techniques that were involved in this study, mainly the insurgence of magneto-optical effects, the MOKE technique and the XMCD technique. Furthermore, an overall description of the experimental conditions under which the measurements have been collected, as well as the presentation of the beamline end-stations, will be introduced. Chapter 3 covers an in-depth description of the system under investigation, specifically a Schottky barrier. Furthermore, the characterization of the samples by means of XPS and TEM will also be reported. Chapter 4 covers the results presented in Ref. [20], as well as the following results obtained on similar samples with different semiconductor dopings. Chapter 5 deals with the XMCD static investigation of the whole Ni $M_{2,3}$ edge and Si $L_{2,3}$ edges performed in reflection. Despite the fact that XMCD represents a standard technique, as only limited data were available in literature at the Si edge, the obtained results have the potential to hold significant value in the field of Spintronics, especially because of the dependence on the doping concentration. Chapter 6 introduces the main tools for calculating the reflectivity of an arbitrary stack by the transfer matrix method and the effects of magnetization on the intensity and the polarization of a reflected beam. Using these tools, the XMCD and MOKE signal on the interface is then calculated. Finally, by considering the retrieved XMCD signal at the Si $L_{2,3}$ edge, a reasonable form of the out-of-diagonal component of the dielectric tensor has been retrieved, which in turn has allowed the computation of the MOKE signal across the edge.

Experimental techniques

In 1845 Faraday [21] discovered that the light polarization traveling in a solid rotated when it was exposed to the-newly discovered magnetic field. The transparent substance he used imposed a rotation of the linearly polarized light by an amount proportional to the distance traveled in the solid and the intensity of the magnetic field along the light direction. This finding corroborated the idea that electric and magnetic fields and light were different facets of the same theory. This was just the first explored interaction of light with magnetism in matter; in 1877 Kerr [22] found that a similar effect materialized upon reflection from a magnetic surface. As the penetration of light in a non-transparent solid was already known at the time to occur on extremely thin scales, this implied a magnitude of the effect greater by several orders. Then, at the end of the nineteenth century, Voigt [23] discovered magnetic birefringent effects on surfaces and later Zeeman [24] discovered the splitting of some emission lines of gases in magnetic fields. This latter finding was particularly puzzling at the time, as the effect induced lines to split in two and to emit opposite circularly polarized light when they are observed along the direction of an applied magnetic field. If the field was instead perpendicular, the spectral lines split into three components emitting linear polarized light, namely one along the magnetic axis and two perpendicular to it. Only the advent of quantum mechanics could finally fully describe the observed effect.

The magnetic ordering of the material - either induced or spontaneous - unites all these effects, but until the nineteenth century, investigations were limited to the optical range. After the advent of X-rays, more targeted investigations were started, although only thanks to the development of tunable monochromated X-ray sources reliable techniques could be established. As an example, Hulme realized in the 1930s that the spin-orbit coupling was responsible for the Voigt effect [25], but only in 1975 Erskine and Stern were able to realize the first *ab-initio* calculation of magneto-optical properties [26] at the Ni $M_{2,3}$ absorption edge. The presence of a large difference in

the absorption of circularly polarized light - then known as X-ray Magnetic Circular Dichroism (XMCD) - was confirmed in the following decade [27]. The magnitude of the effect in the X-rays stood out from the very outset; whereas in the visible range the magneto-optical absorption is in the order of 10^{-3} with respect to the optical counterpart, in the X-ray regime due to the strong spin-orbit coupling the anticipated and then measured effect was considerably larger [28].

During the nineties other technical developments allowed the observation of circular dichroism [29], Faraday [30] and Kerr effects [31] in the x-ray regime, just to name a few. Furthermore, these effects were observed at different edges, as K, $L_{2,3}$ and even the low-energy EUV $M_{2,3}$ edge excitations [32]. These findings provided element-sensitive - both surface and bulk-sensitive - spectroscopic tools for investigating magnetism as well as probing magnetic aspects of electronic structure, such as the exchange splitting. These techniques allowed precise magnetic characterization of complex structures, in particular after the advent of time-resolved resonant techniques .

2.1   Out-of-diagonal terms of the dielectric tensor

In a simple picture, the insurgence of magneto-optical effects can be explained by means of the optical anisotropy induced by the applied magnetic field. In fact, the presence of ordered arrays of spins breaks the time-inversion symmetry in the crystal. To link time-inversion breaking to optical anisotropy it is possible to start from the Onsager reciprocal relations [33] in a general solid, which arise as a consequence of time-inversion symmetry on the microscopic scale. Let us consider the quantities $x_1, x_2 \ldots$ describing the body in any point as the deviations from their average values. As the derivatives $X_i = \partial S / \partial x_i$, where S is the entropy of the system, are linear with respect to x_i for states close to equilibrium [34, 35], they can be defined as

$$\dot{x}_i = \rho_{ik} X_k$$

Therefore, the classical Onsager relations are given as

$$\rho_{ik} = \rho_{ki}$$

If the time symmetry is a symmetry operator of the system, the correlation between any two variable is invariant to which of the two variables is averaged in a later moment, so that

$$\overline{x_i(t)x_k(t+\tau)} = \overline{x_i(t+\tau)x_k(t)}$$

Now, differentiating with respect to τ at t $= 0$ so to get

$$\overline{x_i\dot{x}_k} = \overline{x_i\rho_{kl}X_l} = \overline{\rho_{il}X_lx_k} = \overline{\dot{x}_ix_k}$$

However, the variables x_i are orthogonal, so $x_iX_k = \delta_{ik}$, thus proving the Onsager relations. Now, the correlation process is a second rank tensor in the variables x_i and taking the mean does not affect the symmetry of the product x_ix_k. If R is a symmetry operator of the system that composes a spatial transformation and a time inversion $x'_i = R_{im}x_m$, the correlation becomes

$$\overline{x_i\dot{x}_k} = \rho_{ki} = R_{im}R_{kn}\rho_{mn} = R_{im}R_{kn}\overline{\dot{x}_mx_n}$$

This relation is general and is always respected, but the symmetry operators of the system allow us to further develop it. In fact, if the transformation R transforms only space and leaves the time invariant, the relation turns into

$$\rho_{ki} = R_{im}R_{kn}\rho_{nm}$$

Broadly speaking, the crystals can be divided in two classes based on symmetry; the first class contains the time-inversion symmetry, as is the case for para- and diamagnetic systems, whereas the second does not contain the time invariant operator, as in ferro- and antiferromagnetic systems. In the first case, in particular, $R_{ij} = \delta_{ij}$, whilst in the second case the tensor ρ_{ij} takes the form of a 2-rank non-symmetric tensor. If instead the transport properties of electrical conductivity have to be evaluated, x_i can be associate to the current density, so that X_i is proportional to the electric field (divided by the temperature). As a result, the conductivity tensor, and therefore the dielectric tensor, can be taken as symmetric for magnetically unordered systems. If instead the magnetic field M is nonzero, the dielectric tensor results antisymmetric and the following expression holds.

$$\epsilon_{ij}(\boldsymbol{M}) = \epsilon_{ji}(-\boldsymbol{M})$$

Consequently, assuming a magnetic material whose magnetic field lies in the z direction - which removes the degeneracy in the x-y plane - the dielectric tensor assumes the form

$$\epsilon = \epsilon_0 \begin{pmatrix} \epsilon_{xx} & \epsilon_{xy} & 0 \\ -\epsilon_{xy} & \epsilon_{xx} & 0 \\ 0 & 0 & \epsilon_{zz} \end{pmatrix}$$

Now, the effect of the interaction of light with a magnetic material having a dielectric tensor of this kind can be addressed. The Maxwell relations determine the propagation of electromagnetic waves in a medium, and the constitutive equations in a homogeneous solid can be written as

$$\nabla \times \boldsymbol{E} = \partial \boldsymbol{B}/\partial t$$
$$\nabla \times \boldsymbol{H} = \partial \boldsymbol{D}/\partial t$$
$$\boldsymbol{B} = \mu_0 \boldsymbol{H} + \boldsymbol{M} = \boldsymbol{\mu} \boldsymbol{H}$$
$$\boldsymbol{D} = \epsilon_0 \boldsymbol{E} + \boldsymbol{P} \quad = \boldsymbol{\epsilon} \boldsymbol{E}$$

Where $\boldsymbol{E}$ and $\boldsymbol{H}$ are respectively the electric and magnetic vectors, and $\boldsymbol{B}$ and $\boldsymbol{D}$ the electric displacement and the magnetic induction. Even at optical frequencies, the relative permittivity is equal to 1, so that $\boldsymbol{B} = \boldsymbol{H}$ [36]. Restricting to only linear effects - $\boldsymbol{\epsilon}$ is a 2-rank tensor - any electric and magnetic vector in plane wave components can be decomposed and the system can be solved at a given frequency. Therefore, as the general solution of the electric vector (and analogously for the magnetic vector) will be

$$\boldsymbol{E} = \boldsymbol{E_0} e^{i(\omega t - \boldsymbol{k} \cdot \boldsymbol{r})}$$

Applying the rotor to the first equation and obtain

$$\nabla \times \nabla \times \boldsymbol{E} = \frac{\partial}{\partial t}(\nabla \times \boldsymbol{H}) = \boldsymbol{\epsilon} \frac{\partial^2}{\partial t^2} \boldsymbol{E}$$

Then, using the rotor identity and substituting the plane wave solution, the Fresnel equation can be finally obtained

$$\boldsymbol{\epsilon} \boldsymbol{E} = \frac{c^2 k^2}{\omega^2}(\boldsymbol{E} - \hat{\boldsymbol{k}}(\hat{\boldsymbol{k}} \cdot \boldsymbol{E}))$$

The refractive index is defined in a solid as $n = ck/\omega$, so that the Fresnel equation reduces to

$$\boldsymbol{E} \cdot [n^2 \boldsymbol{1} - \boldsymbol{\epsilon} - \boldsymbol{n} : \boldsymbol{n}] = 0$$

where $\boldsymbol{n} : \boldsymbol{n}$ is the dyadic product $n_i n_j$. The Fresnel equation describes the normal modes of an electromagnetic wave propagating in a solid. To

obtain a solution, the determinant $det[n^2 \mathbf{1} - \boldsymbol{\epsilon} - \boldsymbol{n} : \boldsymbol{n}] = 0$ has to be solved. The peculiarity of the Fresnel equation is that in general there are not 3 independent eigenmodes, but only 2 for $\boldsymbol{n}$.

The simplest solution for the Fresnel equation is the isotropic non-magnetic medium, or $\boldsymbol{\epsilon} = \epsilon_0 \mathbf{1}$, for which the solution is $n^2 = \epsilon_0$. Let us consider again the dielectric tensor for a magnetic material with the field on the z-axis. If the light is impinging on the sample at normal incidence, the σ- and π- polarizations are equivalent. As the incident wave is propagating in the z-direction, $\hat{\boldsymbol{k}}$ can be set equal to $\boldsymbol{e_z}$; this simplifies the equation, as the term turns out to be $\boldsymbol{n} = (0, 0, n)$, causing the z-term of the electric field to vanish. The equation reduces to

$$\begin{vmatrix} \epsilon_{xx} - n^2 & \epsilon_{xy} & 0 \\ -\epsilon_{xy} & \epsilon_{xx} - n^2 & 0 \\ 0 & 0 & \epsilon_{zz} \end{vmatrix} \begin{vmatrix} E_x \\ E_y \\ E_z \end{vmatrix} = 0$$

whose solutions are

$$n_\pm = \sqrt{\epsilon_{xx} \pm i\epsilon_{xy}}$$

And the electric field conditions for the components E_x and E_y are

$$E_x = \pm i E_y$$

This means that the normal modes of the lights are pure circularly polarized light.

2.2 MOKE effect

From the last consideration, it can be promptly affirmed that the interaction of light with magnetized matter can result both in the change of phase (rotation of the polarization) and in the change of absorption rates for the two modes (ellipticity change). The effect is a consequence of the out-of-diagonal term having both real and imaginary components. The interacting beam, either by reflection (Kerr effect) or transmission (Voigt effect) generally retain the magnetic information of the whole magnetic stack. In fact, light interaction in a multilayered material depends on the whole stack, as can be inferred in the transfer-matrix method approach [37].

Accordingly, the observed magneto-optical effects will depend on the considered geometry. In the general case, the result depends on the configuration of the magnetic vector $\boldsymbol{M}$ with respect to the incident wave vector

k. Correspondingly, three different MOKE geometries are presented. In the following, the axis perpendicular to the surface will be called as z and the beam wave vector will lie on the z-y plane with a certain angle θ with respect to the surface.

Name	(a) Polar	(b) Longitudinal	(c) Transverse
Geometry			
Detection	Out-of-plane	in-plane	in-plane
Polarization Variation	Rotation Ellipticity		None
Measurement	Polarization Analysis		Intensity measurement

Figure 2.1:   Schematic diagram of MOKE measurement geometry for p-polarized incident light. The dashed line in the geometry row expresses the incident plane. In the polarization variation row, the changes in the polarization states that are projected in the plane that lies perpendicular to the direction of the travel of the light are shown for both incident (left) and reflected light (right). Reprinted from [38].

In the *polar* configuration, the magnetic vector points perpendicular to the surface. This is the case for magnetic materials with high anisotropy. The dielectric tensor will have the previously shown shape. In this case, near normal incidence is usually employed to yield the maximum effect. In the *longitudinal* configuration, instead, the magnetization lies in the plane of the sample surface and the incident plane. Here a high incidence angle is rather employed in a linear polarized beam so as to bind the change in polarization directly to the component of magnetization along the surface. Finally, in the *transverse* configuration, the magnetization vector lies in the plane of the sample but is perpendicular to the incidence plane. This configuration is in part exceptional, as it does not cause change of rotation, but instead change of intensity [39]. By the same symmetry argument which allowed us to obtain the dielectric tensor in the polar configuration, the general dielectric tensor for an arbitrary magnetization vector $\boldsymbol{M} = M\left[\sin(\phi)\cos(\gamma), \sin(\phi)\sin(\gamma), \cos(\phi)\right]$ can be written with the polar angles ϕ and γ as

$$\boldsymbol{\epsilon} = \epsilon \begin{pmatrix} 1 & i \, \cos(\phi)Q & -i \, \sin(\gamma)\sin(\phi)Q \\ -i \, \cos(\phi)Q & 1 & i \, \cos(\gamma)\sin(\phi)Q \\ i \, \sin(\gamma)\sin(\phi)Q & -i \, \cos(\gamma)\sin(\phi)Q & 1 \end{pmatrix}$$

Here a further simplification has been made by taking the symmetry of the system as cubic. As a result, the dielectric tensor has only two independent components, the in-diagonal component $\epsilon_{kk} = \epsilon$ and an out-of-diagonal one ϵ_{kj}. Further, it is possible to define the magneto-optical constant, or Voigt constant, $Q = i \, \epsilon_{kk}/\epsilon_{kj}$. The dependence on the magnetization vector is hidden in the Voigt constant, as it is (at the first order) linear with the magnetization module M.

Solving the Maxwell equations at the interface with this expression for the dielectric tensor allows to obtain the Fresnel equivalent equations for the s- and p-polarized components of the reflected beam at a magnetic surface. The notable fact is that instead of having only the terms r_s and r_p, because of the change of phase and intensity of the reflected beam, the reflection matrix R is no longer diagonal. The derivation of the general expression for the four components of the reflectivity matrix for the general case can be particularly complex, as it implies working with multiple refracted beams. This is the result of having multiple modes for the transmitted waves in magnetic media, since the Snell equation involves a complex angle [40, 41, 42]. In turn, this stems from the existence of two modes for any linearly polarized beam, as previously shown. As a consequence, the effect of the reflection from a surface can be written as

$$\begin{pmatrix} E_s^r \\ E_p^r \end{pmatrix} = \begin{bmatrix} r_{ss} & r_{sp} \\ r_{ps} & r_{pp} \end{bmatrix} \begin{pmatrix} E_s^i \\ E_p^r \end{pmatrix}$$

Therefore, when for example the p-component is incident, the reflected beam shows an s-component in addition to the p-component due to the existence of magnetization. The induced s-component is not in phase with the p-component and as a result in the general case the light becomes elliptically polarized with a principal axis rotated with respect to the incident beam. The usual employed incident beam is either fully s- or p-polarized in order to simplify the analysis. In either of the two cases the complex Kerr angle can be obtained as [41, 40]

$$r_{ps}/r_{ss} = \theta_{K,s} + i \, \eta_{K,s}$$
$$r_{sp}/r_{pp} = -\theta_{K,p} + i \, \eta_{K,p}$$

where the real part θ_K is the Kerr rotation, whereas the imaginary part η_K is the ellipticity of the reflected beam.

2.2.1   Time-resolved MOKE and resonant-MOKE

After the realization of the first X-ray magneto-optical techniques, the next revolution in magnetic studies came when the time scale at which the magnetic dynamics in systems occur was first investigated. Using a time-resolved MOKE apparatus, in his seminal study Beaurepaire [43] discovered that the timescale of the demagnetization in nickel occurred within 0.5 ps from the excitation. This came in part as a surprise, as the hot electron distribution relaxes with the lattice on the 1-10 picoseconds time scale due to electron-phonon coupling and it was known that optical excitations preserve the spin degree of freedom. As a result, some additional coupling was responsible to the ultrafast demagnetization. It is worth noticing that up until then the faster devices could achieve a switch of magnetization on a sub-nanosecond scale; the promise of ultrafast magnetic recording technology consequently aroused wide interest in the topic. In Beaurepaire's model a three-temperature system was considered; electrons, spins and the lattice act as three different thermal baths with three different temperatures and exchange energy via couplings between the baths.

Nonetheless, the ultrafast demagnetization faced the challenge of explaining where the spin angular momentum was transferring to, since it was removed from the system but still had to be conserved. As an example, since the Einstein-De Haas effect discovery [44], it was known that spin momentum and angular momentum could be transferred between each other, but as the phenomenon was widely studied in the following years it became clear that the timescale of this dissipation was on the tens of picoseconds. This evidence seemed in contrast with Beaurepaire's and the following works. As a consequence, further mechanisms were proposed, such as the Elliot-Yafet electron-phonon spin-flip scattering between an electron bath not thermalized with the lattice one [45], some spin-lattice coupling enhanced by the hot-electron distribution [46], electron-electron scattering [47] or ultrafast spin diffusion [48]. At present, there is still debate on the contribution and the timescale upon which any of these different phenomena occur. This quote from Koopmans is in part enlightening which relates similar frustration on the experimental side: "in general the probe only provides a limited access to the multidimensional character of the strongly nonequilibrium magnetic state, which makes interpretation of such experiments an art itself"[49].

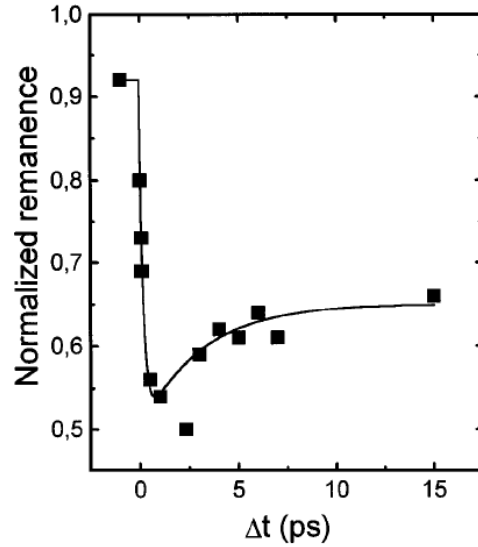After Beaurepaire, due to the large availability of table-top ultrafast laser

Figure 2.2: Transient remanent longitudinal MOKE signal of a Ni(20 nm)/MgF$_2$(100 nm) film for 7 mJ cm^{-2} pump fluence. The signal is normalized to the signal measured in the absence of pump beam. The line is a guide to the eye. Reprinted from [43].

setups and even more sensitive magneto-optical setups, the field of ultrafast magnetic dynamics greatly expanded. In addition to the pure demagnetization loss upon the pump pulse excitation, on longer timescales the system recovers with an additional precessional dynamics term. As a matter of fact, the induced ultrafast dynamics has been proven to induce changes in magnetic anisotropy as well as the magnetic couplings on the same timescale. The modification of these structural magnetic properties can be qualitatively interpreted by considering both the classical limit dynamics and the nonequilibrium thermodynamics of the system. In the classical limit, the simplest is the precessional dynamics; an external field induces a splitting between spin-up and spin-down states of $\Delta_s = \gamma \mu_B H$ - where H is the external driving field - causing the superposed states to precess at a frequency $\omega_L = \Delta_s/\hbar$. This is valid also for an ensemble of spins $\boldsymbol{M}$. Introducing a second term accounting for the damping of the perturbed system into the new final state, the elemental dynamics of the spin precession can be described from the Landau-Lifshitz-Gilbert equation

$$\frac{d\boldsymbol{M}}{dt} = -\gamma\boldsymbol{M} \times \boldsymbol{H_{eff}} - \lambda\boldsymbol{M} \times (\boldsymbol{M} \times \boldsymbol{H_{eff}})$$

where the external driving field has been substituted with the effective field $\boldsymbol{H_{eff}}$ inside the material (which takes into account the magnetic anisotropy, ...). The nonequilibrium thermodynamics of the system considers the well-known fact that the equilibrium magnetism M_{eq} is a function of the temperature T of the system, given that at the Curie temperature the long-range magnetic ordering vanishes. The three-temperature model attempts to answer the problem by having three thermal baths - electron, phonon and spin - with three different heating constants - C_e, C_p and C_s - and three coupling constants accounting for the energy exchange between them, or G_{ep}, G_{es} and G_{ps}. The result is a system of three coupled differential equations

$$C_e\frac{dT_e}{dt} = -G_{ep}(T_e - T_p) - G_{es}(T_e - T_s) + P(t)$$
$$C_p\frac{dT_p}{dt} = -G_{ep}(T_p - T_e) - G_{ps}(T_p - T_s)$$
$$C_s\frac{dT_s}{dt} = -G_{es}(T_s - T_e) - G_{ps}(T_s - T_p)$$

where the optical excitation $P(t)$ acts only on the electron term. Therefore within the first femtoseconds, the electron system is heated, even by thousands of K, and then it thermalizes on different timescales with the two other thermal baths. After tens of picoseconds, the system is thermalized to a new temperature, for which the magnetization can be considered as at equilibrium, except for its higher temperature. Unfortunately, this phenomenological model does not provide any insight into the mechanisms involved in the demagnetization and it does not conserve the total momentum $\boldsymbol{J}$ [50]. In fact, the total angular momentum for the system is

$$\boldsymbol{J} = \boldsymbol{L_e} + \boldsymbol{S_e} + \boldsymbol{L_p} + \boldsymbol{L_\omega}$$

Where the orbital and spin momentum carried by the electronic system has been considered, as well as the phonon system and the photon system angular momentum. The magnetic moment is instead

$$\boldsymbol{M} = \mu_B(\boldsymbol{L_e} + g\boldsymbol{S_e})$$

with $g \approx 2$. Claiming the conservation of the total momentum would require that the total variation of any of the terms composing it would equal

0. The phonon term can be safely neglected on small timescales, as the lattice interactions are slower, as well as the photon term, since the number of photons involved is small. Therefore only the two electronic terms are left, implying a redistribution between the orbital and the spin momentums by the spin-orbit coupling. However, in magnetic systems the spin momentum accounts for almost the entirety of the magnetic moment, hence the total loss of magnetic moment can be reduced up to 50%. The limitations derived from the momentum conservation are however not accounted for in the three temperature model. A second limitation to the model is the fact that the optical excitation can change the magneto-optical response of the system, even if it conserves the spins, due to the filling of the excitation channels, in a phenomenon known as "dichroic bleaching" [51].

The lifetime of the excited electrons is very short, in the order of up to few tens of femtoseconds. Due to electron-electron scattering, the hot electrons thermalize fast and after a cascade of e-e scattering they reach equilibrium temperature. The final electron temperature $T_{e,F}$ is the thermal temperature that the electron gas will reach within this small timescale. To account for this fact, a second electron population which is not affected by the optical excitation is often introduced. Within this model, after the excitation the electron gas will be composed of a hot component at a temperature $T_{e,E}$ and a component at equilibrium temperature; the temporal evolution of the electronic temperature will follow an exponential decay as

$$T_e(t) = \Delta T_1 \Big[1 - exp\Big(\frac{-t}{\tau_T}\Big) \Big]$$

where ΔT_1 is the final induced temperature rise and τ_T is material-dependent.

Electron-phonon scattering it is usually caused by elastic deformations of the potential; assuming a constant electron and lattice heat capacities, the thermalization dynamics of the electronic and lattice systems can be implemented by solving analytically the separate electron-phonon two-temperature system which converges exponentially with a time constant

$$\tau_E = \frac{C_e C_p}{C_e + C_p} \frac{1}{G_{ep}}$$

As a result, it is obtained

$$T_e(t) = \Delta T_1 \Big[1 - exp\Big(\frac{-t}{\tau_T}\Big) \Big] exp\Big(\frac{-t}{\tau_E}\Big) + \Delta T_2 \Big[1 - exp\Big(\frac{-t}{\tau_E}\Big) \Big]$$

where ΔT_2 is the final temperature of the system. This equation takes into account that the thermalization of the electronic system occurs at a shorter timescale if compared to the lattice one, so that the electronic gas is taken in a quasistatic approximation.

As a last step, having found that indeed the ultrafast spin relaxation acts on a subpicosecond time scale, its relationship with the electron temperature has been left left to be found. Several studies on T_e and T_s concluded that already after 300 femtoseconds [52] the spin system is closely following the electronic system, so that $T_s(t) \sim T_e(t)$; only at higher temperatures electrons and lattice equilibrate [50]. This has been further confirmed with the first ultrafast experiments with X-ray magnetic circular dichroism [53]. As a result, with a good fidelity, the ultrafast demagnetization can be qualitatively described with the empirical two-exponential curve

$$M(t) = M_0(1 - e^{-t/t_r})e^{-t/t_d}$$

where the demagnetization and recovery times are taken into account.

The recent progress towards new-generation light sources, such as the x-ray free-electron laser (FEL) and the high-harmonic generation (HHG) lasers, allowed to extend the time-resolved domain to the low-energy absorption edges. Indeed, these novel monochromatic sources with ultrashort pulses revolutionized magnetic studies with the development of time-resolved resonant magnetic techniques. Among them, resonant MOKE techniques hold a leading position, inasmuchas they show giant effects when compared to conventional visible MOKE due to the inner shell resonance effect [54, 55] and allow the extraction of the intrinsic magnetization dynamics on a subpicosecond timescale through the measurement of both the rotation and the ellipticity. Moreover, measurements using linearly-polarized light are straightforward to use in analysis of the magnetic response, as they need no accurate preliminary determination of the degree of polarization [38].

The M absorption edge for magnetic transition metals is particularly suited to the RMOKE technique, as the reflectivity around these edges is sizable for a wide range of angles. This in turn ensures a better signal-to-noise ratio, as well as depth dependent studies of the magnetization profiles. As a result, if below the UV energy range magnetization probing techniques detect the average information of target materials, RMOKE adds element sensitivity to magnetic dynamic studies, as these.core level states are relatively localized to the element atoms. Finally, in complex magnetic structures this allows to investigate the individual dynamics of each magnetic element.

2.2.2   MagneDyn beamline

The MagneDyn beamline has been developed to study the electronic states and the local magnetic properties of the excited systems in the EUV range [56, 57]. Exploiting the unique features of the FERMI Free Electron Laser (FEL) [17], the beamline can achieve the study on the ultrafast magnetic dynamics in a pump-probe arrangement by using the FEL and synchronized optical laser pulses in a pump-probe setup. The FERMI scheme is an externally-seeded FEL, meaning that the electron bunch is seeded with an external laser pulse, allowing full control of the wavelength and bandwidth of the FEL pulses by varying the parameters of the seed. As a result, the FEL pulses generated by the APPLE-II type undulators can be widely tuned in terms of energy, intensity, polarization and duration. Moreover, because of the seeding process, the FEL pulses inherit both the temporal and the spatial coherence of the seeding laser.
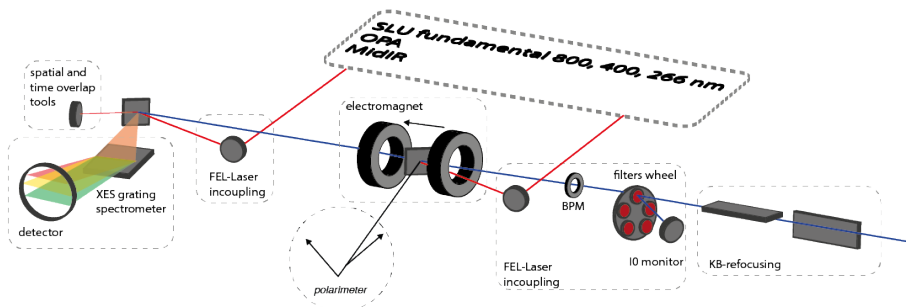

Figure 2.3: Optical layout of the experimental area of MagneDyn. From the right: the FEL beam can be focused and shaped along the beam direction in either the magnet or the RXES chambers by the KAOS refocusing mirror system. The SLU is manipulated in a dedicated optical breadboard and then driven into the experimental chambers through two dedicated in-coupling high-vacuum chamber where piezo-motorized collecting mirrors are placed. In the first in-coupling vessel, a beam positioning monitor, two solid state filter wheels, and an I0 detector are installed. The electromagnet is coupled to an XUV polarimeter. The RXES chamber has an XES355 spectrometer available. Reprinted from [57].

The transport branch of the beamline comprises an online spectrometer, vertical and horizontal focusing mirrors based on the Kirkpatrick–Baez active optics (KAOS) system, and a set of solid-state filters (thin submicron thick free-standing films of metals). The 2° angle of incidence of the gold-

coated mirrors allow a transport of 70% for the long wavelengths (7–30 nm) range, which comprises the $M_{2,3}$ absorption edge of the transition metals and in particular the $M_{2,3}$ edge of the magnetic elements Fe, Co, Ni. The intensity of the incoming pulses is monitored on a shot-to-shot base by intensity monitors along the delivery system both in the form of photoionization chambers from noble gases and drain currents from the beamline mirrors. The beamline spectrometer, which collects the first order of diffraction from a grating on a shot-to-shot base, enables the complete characterization of each probe pulse arriving to the sample.

The optical pump pulses arriving in the experimental chamber is intrinsically synchronized with the FEL pulses, enabling a 6 fs jitter. The optical pulses are delivered to the beamline through a dedicated low-vacuum laser transport beamline terminated by a quartz window. The beam pointing instability is corrected by camera feedbacks acting on active mirrors. The dedicated bemline optical table allows the control of the polarization state, harmonic conversion pulse compression, intensity change, beam steering, pointing stabilization, and focusing. The standard parameters of the first harmonics pump pulses are a duration of 55 fs and a central wavelength of 780 nm, although a setup for the generation of the second and the third harmonic is also available. The optical laser, which is delivered to the sample through an in-vacuum mirror, and the FEL pulses arrive on the sample in the experimental chambers in a quasi-collinear geometry, having a 1.5° angle between the beam directions. This configuration allows an optimal pump-probe spatial overlap while moving or rotating the sample. The optical laser-fel pulse timing can be set in the range 1 fs - 1 ns range, whereas the temporal overlap is finely measured by monitoring the transient reflectivity on a Si substrate in a pump (FEL) - probe (IR) scheme.

The experimental chamber is equipped with a four-axes manipulator with stepper motors for precise sample adjustment. The sample can be cooled down up to 25 K by means of a helium closed-cycle, as well as heated up to 450 K by a heating stage. The sample is placed in a 1.6 T electromagnet providing a magnetic field collinear to the FEL beam direction. MagneDyn employs the longitudinal-MOKE configuration in a time-resolved fashion. The optical pulses delivered to the sample act as a pump and the FEL beam propagating in the magnet scattering chamber, where is then reflected from the sample, is used as a probe. The reflected beam from the sample, which holds the magnetic information as a rotation of the polarization, is then recollected and analyzed by the TONIX polarimeter.

2.2.3 TONIX polarimeter

Polarization analysis in reflection was carried out by the TONIX polarimeter. The polarimeter works in a scheme resembling the Wollaston balanced-photodetection design. The TONIX (wollasTON polarImeter for X-ray) is composed of a set of mirrors to decompose the incoming beam as well as detection devices to simultaneously measure the beams intensity. To infer the angle of polarization of the incoming beam, it is necessary to infer the degree of polarization along at least two noncollinear axes. This is achieved by using two distinct features: (i) placing the two mirrors M1 and M2 at the Brewster angle and (ii) placing these mirrors on orthogonal mounts. At the Brewster angle any incoming beam will result in being mainly s-polarized with respect to the mirror incidence plane as the extinction ratio r_s/r_p is maximized (at the Brewster angle r_p still deviates from 0, as in the EUV range the absorption is not negligible). Having two mirrors, the reflected beams will be s-polarized along two orthogonal planes, and thereby can act as the basis to reconstruct the polarization angle of the incoming beam.
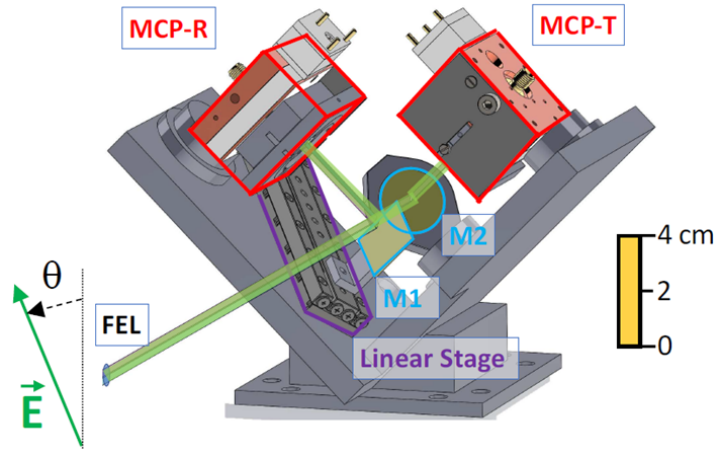

Figure 2.4: TONIX 3D technical drawing, front side view. The schematic of the beam splitting and the MCP mounts are also displayed. A ruler is plotted on the right side to display the TONIX size. The green arrow represents the electric field vector $\boldsymbol{E}$ of the incoming x-ray pulse, and h is the angular deviation from the vertical or horizontal axis. Adapted from [18].

Some critical aspects must be taken into consideration to maximize the sensitivity. The intensities of the two beams undergoing the reflections on

the two mirrors must be balanced. This is achieved by employing one of the mirrors - M1 - as a beam splitter; M1 is in fact mounted on a motorized stage that allows it to intercept the beam reflected from the sample. By changing its position it is therefore possible to switch from blocking entirely the beam to letting it pass completely. The unaffected component of the beam is then intercepted by the mirror M2, which is fixed instead. Hence, balancing the two beams intensities is a matter of balancing the position of the mirror M1. Further, to increase the sensitivity, a material with the highest r_s/r_p extinction ratio has been chosen; for the energy range 55-75 eV a good material is Niobium, having a sizable r_s reflectivity in the order of 3% and a good extinction ratio in the order of 50-100. The Brewster angle has a weak dependence on energy in this range, which makes it possible to use mirrors at fixed angles (at the Brewster angle corresponding to the central energy) without losing much sensitivity. Finally, by having the incoming FEL beam p-polarized and the two mirror mountings placed ortogonally, the geometry allows to have the best sensitivity to the rotation of the polarization angle, which will cause antagonist effects on the two branches. The intensity of the beams reflected from M1 and M2 are then collected from two microchannel plates (MCPs). It is possible to reconstruct the angle of the polarized beam and the reflectivity from the intensities I_1 and I_2 measured by the two MCPs as [58]

$$\theta = \frac{1}{2}\frac{I_1 - I_2}{I_1 + I_2}$$
$$R \propto I_1 + I_2$$

The advantage of such a design is a sensitivity of rotations up to one degree on a single shot basis, making it perfect to time-resolved magneto-optical techniques.

To reconstruct a magnetic dynamics, two delay traces at opposite saturating magnetizations must be collected in a pump-probe configuration. The standard pump-probe configuration consists on chopping the pump laser at half the frequency of the probe, so that the pumped signal is on every other pulse. Then, at any delay, the pump-probe signal θ_{pp} will be simply the difference of the mean pumped θ_p and the mean unpumped θ_u, so that

$$\frac{\Delta M(t)}{M_0} = \frac{\theta_{pp}^+(t) - \theta_{pp}^-(t)}{\theta_u^+ - \theta_u^-}$$

Where the apices $\pm$ express the sign of the saturating magnetizations,

whereas the denominator factor $\theta_u^+ - \theta_u^-$ serves as the amplitude of the unpumped hysteresis.

2.3 XMCD effect

The development of X-ray magnetic circular dichroism (XMCD) was a direct result of Erskine and Stern [26] theoretical expectations of strong magnetic dichroic effects at absorption edges. In their original work, they considered the $M_{2,3}$ optical transition, or from 3p filled states to 3d empty states. The transition matrix elements result predominantly from the spin-orbit splitting of the 3p core state in conjunction with the final d-state spin polarization. The calculations predicted a change up to 10 % due to the strong spin-orbit interaction [26]. Hence, magnetic sensitivity results from the sensitivity of the transitions from core shells to empty states to the symmetry of the initial state due to the (electric-dipole) selection rules. The circular dichroism of Fe, Co and Ni at the L-edges was then thoroughly investigated in the following decade, leading to the establishment of XMCD as a reliable probe of magnetization.
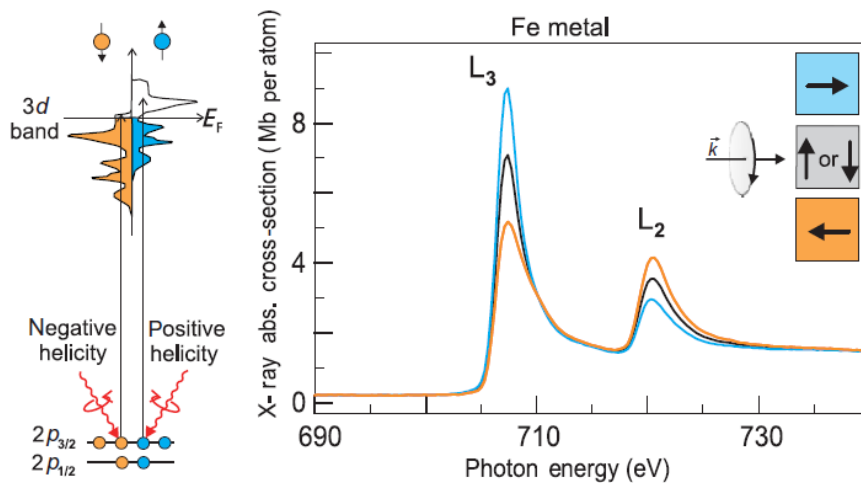

Figure 2.5: The XMCD effect illustrated for the L-edge absorption in Fe metal. The shown density of spin-up and spin-down states closely resembles that calculated for Fe metal. The case of circularly polarized X-rays with positive angular momentum (helicity) is shown, and the color coded spectra correspond to the shown sample magnetization directions. Reprinted from [59].

XMCD results from the different absorption of left and right circularly polarized light when a component of the sample magnetization is on the x-ray propagation direction. As previously shown, in the event of a nonzero component of the magnetism of the sample along the wave vector, the two eigenstates inside the sample correspond to circularly polarized light. As a result, $\mu^+ \neq \mu^-$, where the apex $\pm$ denotes the two eigenmodes for a given direction of the magnetic field (in fact, reversing the magnetic field corresponds to inverting the modes). It is likewise possible to derive the transition matrix elements in a simple two-step model [27]. In the first step the photoelectrons excited upon the x-ray absorption become spin-polarized according to the helicity of the photons, as core states are spin-orbit split. Then, the unoccupied final states act as spin detectors of the photoelectrons. In fact, as the system is magnetic, the density of states is different for spin-majority and spin minority. Accordingly, the absorption of X-rays can be constructed with a spin-independent term μ_0 and a spin dependent one μ_c. If the polarization of the excited electrons is proportional to the polarization P_e of the X-rays, then the total absorption will be written as

$$\mu(E) = \mu_0 + \mu_c \sim |M_{if}|^2(\rho(E) + P_e\Delta\rho(E))$$

where M_{if} is the matrix element that connects the initial and final states and $\Delta\rho = \rho^{\uparrow\uparrow} - \rho^{\uparrow\downarrow}$, i.e. the difference between the parallel and antiparallel configuration of the initial and final states. The measured intensities can be calculated by the Lambert-Beer absorption law, which for a sample of thickness d results

$$I(E,d)^{\pm} = I_0(E)\,e^{(\mu_0(E)\pm\mu_c(E))d}$$

As the XMCD effect, depends on the relative orientation between the helicity of the photons $\boldsymbol{\sigma}$ and the magnetic field as $XMCD \propto \boldsymbol{\sigma} \cdot \boldsymbol{M}$, it is possible to define a magnetic contrast as the relative change with respect to the nonmagnetic case, or

$$XMCD = \frac{\mu_c}{\mu_0} = \frac{I^+ - I^-}{I^+ + I^-} = tanh(P_e\mu_c d)$$

For a full (100%) polarization of the photons, XMCD values can yield up to tens of percent. As any spectroscopic measurement, in measuring the whole intensity it provides a macroscopic measurement. Even in ferromagnetic samples, if they are not monocrystalline, the different domains will contribute according to their orientation.
It is possible to calculate the exact matrix elements for a simple case, as the

$L_{2,3}$ transition, using Fermi's golden rule for the spin-polarized density of states case. For a dipole transition the matrix element is proportional to

$$M_{if} \propto \langle f | \boldsymbol{\epsilon} \cdot \boldsymbol{r} | i \rangle$$

where $\boldsymbol{\epsilon}$ is the polarization vector. Due to the scalar product, the dipole transition must obey the following selection rules connecting the initial and final states so to have a nonzero matrix element

$$\Delta j = 0, \pm 1, \quad \Delta l = \pm 1, \quad \Delta s = 0, \quad \Delta m = \begin{cases} +1 & \text{right circular} \\ 0 & \text{linear} \\ -1 & \text{left circular} \end{cases}$$

The absorption process connects states with different angular momentum quantum numbers i and m_l. The initial and final states, characterized by the form $|n \; j \; m_j\rangle$ must be rewritten in terms of the angular momentum $|n \; l \; m_l\rangle$, as the absorption is sensitive to the angular momentum l and not to the total angular momentum j. For the $L_{2,3}$ transition, the initial states in the total angular momentum $j = 3/2$ ($p_{3/2}$) and $j = 1/2$ ($p_{1/2}$) must be written using the Clebsh-Gordon coefficients into the angular momentum states.

$$|3/2, \pm 3/2\rangle = |\pm 1, \uparrow\downarrow\rangle$$
$$|3/2, \pm 1/2\rangle = \sqrt{2/3}\,|0, \uparrow\downarrow\rangle + \sqrt{1/3}\,|\pm 1, \downarrow\uparrow\rangle$$
$$|1/2, \pm 1/2\rangle = \mp\sqrt{1/3}\,|0, \uparrow\downarrow\rangle \pm \sqrt{2/3}\,|\pm 1, \downarrow\uparrow\rangle$$

To evaluate the matrix elements, a coordinate system in which the z axis is parallel to the magnetization field can be selected, so that

$$\boldsymbol{\epsilon_{\pm 1, 0}} \cdot \boldsymbol{r} = R_{\pm 1, 0}$$

with

$$R_{\pm 1} = \mp\sqrt{1/2}(x + iy), \quad R_0 = z$$

where ϵ_{+1}, ϵ_{-1} and ϵ_0 correspond to right and left circular and linear polarization respectively. Employing only circularly polarized light, the matrix elements for the $2p \rightarrow 3d$ transition have to be calculated, where the final state has $l' = l + 1$ and $m'_l = m_l \pm 1$. Finally, the matrix elements can be calculated using the Wigner-Eckart theorem as

$$\langle n', l+1, m_l \pm 1 | R_{\pm 1} | n, l, m_l \rangle = -\sqrt{\frac{(l \pm m_l + 2)(l \pm m_l + 1)}{2(2l + 3)(2l + 1)}} \, \langle n', l+1 || \boldsymbol{R} || n, l \rangle$$

where the radial term R is independent of the quantum number and therefore independent of helicity. Inverting both the helicity and the magnetic quantum number m_l does not change the result of the transition probabilities. However, inverting only m_l is equivalent to inverting the helicity (and therefore the spin). By adding all the terms of a specific spin contribution it is possible to calculate the total transition probability. As an example, the transition from L_3 with a spin-up electron under right circular polarized light is obtained by having

$$\langle 2, 2, | R_{+1} | 1, 1 \rangle = 2/5 R^2, \quad \langle 2, 1, | R_{+1} | 1, 0 \rangle = 1/5 R^2, \quad \langle 2, 0, | R_{+1} | 1, -1 \rangle = 1/15 R^2$$

so that the transition L_3 with right circular polarized light results as

$$p_{+1,\uparrow}(L_3) = \frac{2/5 + 1/5 \cdot 2/3 + 1/15 \cdot 1/3}{2/5 + 2/5 \cdot 1/3 + 1/5 \cdot 2/3 + 1/5 \cdot 2/3 + 1/15 \cdot 1/3 + 1/15} = 62.5\%$$

And similarly

$$p_{-1,\uparrow}(L_3) = 37.5\%, \quad p_{+1,\uparrow}(L_2) = 25\%, \quad p_{-1,\uparrow}(L_2) = 75\%,$$

As a result, right circular polarized light excites mainly spin-up electrons at the L_3 edge and mainly spin-down polarized electrons at the L_2 edge. If instead the whole edge is considered, $p_{\pm 1,\uparrow}(L_3 + L_2) = 2/3 p_{\pm,\uparrow}(L_3) + 1/3 p_{\pm,\uparrow}(L_2) = p_{\pm 1,\downarrow}(L_3 + L_2) = 50\%$, so it shows no polarization. Therefore, the spin polarization in the XMCD arises from the spin-orbit splitting of the core level.

The second step involves the filling of the final states; as the d-states are split by the exchange energy, the unoccupied density for spin-up and spin-down states is different. In the extreme case of half metals, one of the two spin-split bands is completely filled; in this case, the allowed transitions will involve only the filling of the partially emptied band, and therefore only one variety of spins. Consequently, the dichroism is maximized. Normally, both spin-up and spin-down empty states are available for the transition, so that the transition is proportional to the unbalance of the spin population in the partially occupied bands.

2.3.1 Sum rules

Part of the success of XMCD techniques arises from the possibility to infer quantitative information from the XMCD spectral features. In fact, under some conditions it is possible to derive the three components of magnetic moment, namely the orbital $\boldsymbol{L}$, the spin $\boldsymbol{S}$ and the dipole $\boldsymbol{T}$ components. The two rules were derived separately by Thole, Carra et al. [60, 61] for single ions in a crystal field with partially filled bands.

Let us consider a transition from a core level c to a valence level l filled with n electrons in its ground state. The first sum rule can then be written (in units of the Bohr magneton μ_B) as [62]

$$\frac{\int_{j^++j^-} I^+ - I^-}{\int_{j^++j^-} I^+ + I^0 + I^-} = \frac{2 + l(l+1) - c(c+1)}{2l(l+1)(2(2l+1)-n)} \langle 0|L_z|0\rangle$$

where the terms $I^{\pm,0}$ represent the intensities at opposite helicities or in linear polarization and $j^\pm$ corresponds to the $c+1/2$ and $c-1/2$ transitions - in terms of the total momentum - which are well energetically separated. Moreover, it is possible to write the total number of holes in the final state as $h = 4l+2-n$. The expression greatly simplifies in the case of the transition from c to $l = c+1$, where the coefficient reduces to $1/lh$. This first sum rule thus connects the integral of the XMCD signal - normalized to the nonmagnetic edge integral - to the ground state orbital magnetic moment $\langle 0|L_z|0\rangle$.

Similarly, the second sum rule is for $c \neq 0$

$$\frac{\int_{j^+} I^+ - I^- - \frac{c+1}{c} \int_{j^-} I^+ - I^-}{\int_{j^++j^-} I^+ + I^0 + I^-} = \frac{c(c+1) - l(l+1) - 2}{3ch} \langle 0|S_z|0\rangle + A(c,l,h)\langle 0|T_z|0\rangle$$

Where the coefficient $A(c,l,h)$ is equal to $\frac{l(l+1)[l(l+1)+2c(c+1)+4]-3(c-1)^2(c+2)^2}{6cl(l+1)h}$. The second sum rule then connects the difference of the integral of the XMCD signal between the j^- and the j^- edges to the ground state spin $\langle 0|S_z|0\rangle$ and the dipole $\langle 0|T_z|0\rangle$ magnetic moments. The requirement for the spin sum rule is that the core level splitting is sufficiently big to result in well-defined j^+ and j^- transitions.

The range of applicability of the XMCD sum rules has been questioned over the years [63, 64]. Nonetheless, they are widely used to estimate the contributions of the three magnetic moments to the total one. It must be emphasized that the sum rules rely on several assumptions. The first one is that generally both the $l = c+1$ and $l = c-1$ channels are equally possible.

As the sum rules are different for the two transitions when $c \neq 0$ and the two channels cannot be energetically separated, it must be assumed that only one of the two transitions is dominant, while the other is negligible. This is the case for example at the $L_{2,3}$ edge, where the channel $l = c - 1$ is several order smaller. In Ti^{3+} for instance the ratio $|\langle 4s||r||2p \rangle|^2 / |\langle 3d||r||2p \rangle|^2$ is less than 10^{-2} [65]. The second assumption is that the final state of the transition $c^{4c+2}l^n \rightarrow c^{4c+1}l^{n+1}$ is a pure state. This is equivalent to stating that the transition involves only the core level donating an electron and the final level accepting the electron. In this picture, there is no relaxation from the other shells as a result of the excitation of the core level and the subsequent formation of a hole. Actually, in the general case the final state is not a pure state, but instead a multiplet of states. Thirdly, having assumed that the radial component of the integral $|\langle l||r||c \rangle|^2$ leads to its simplification in the expression. This is the result of having considered only dipole transitions and having considered the radial integral to be independent on the energy. Usually the high-order transitions (electric quadripole, magnetic dipole) are much less intense than the electric dipole transitions. It is difficult to make estimates on the range of validity of the second part of the assumption. The fourth assumption concerns the separation of the core levels. The spin-orbit splitting, which varies in the range 2-100 eV, can still lead to a mixing of the states; in general this energy should be compared to the other relevant energies involved in the total hamiltonian describing the final state.

Finally, it should be noticed that as the validity of the whole theory is somehow difficult to check, the only possible test is theoretical. The magnetic X-ray absorption can be calculated and therefore the average of the three momentum operators, but for instance, as soon as you include additional terms such as delocalized electrons, the discrepancy starts to grow. Even though the validity is limited by certain approximations, the applicability of the sum rules has been theoretically [66] and experimentally verified for the 3d metals Fe and Co [67].

2.3.2   TEY and FY

As the effect is basically related to the absorption coefficient, the most direct measurement is the transmission mode, in which the photon flux is measured just before and after a thin sample. But due to the strong absorption, it is often difficult to realize except for thin free-standing films, which are hard to prepare. As a consequence, the most widely spread techniques are the total electron yield (TEY) and the fluorescence yield (FY).

In TEY the measured effect is the sum of all the photoelectrons that are cre-

ated in the absorption process and escape from the sample. Unfortunately, owing to the small free path of electrons in solids, the further away the excited atom is from the surface, the less likely the electron is to escape from the solid. Moreover, as the core holes generated are rapidly filled primarily by Auger emission, the TEY technique is mainly dependent on secondary electron generation. As a result, the technique is capable of probing only the first layers of the material [68], which is in the order of 3 nm for 3d transition metals [69]. An expression for the TEY can be derived by considering that the signal must account for both the electron and photon mean free paths. The penetration depth of the incoming photons is exponentially dumped with a factor $\lambda_x cos(\theta)$ accounting for the incident angle, whereas the electron escape is governed by the electron mean inelastic free path λ_e (as TEY main contribution is from secondary electrons). Correspondingly, the contribution of all layers is exponentially dumped according to the two terms and it can be demonstrated that the total contribution follows the law [69]

$$ TEY \propto \frac{\mu}{1 + \lambda_e/\lambda_x cos(\theta)} $$

which in the case of the limit of infinite X-ray penetration depth shows a linear dipendence of TEY with respect to the absorption coefficient. TEY current is usually measured directly through the sample drain current, which requires the electrical insulation of the sample. In applied magnetic field an extraction grid must be used to force the escape of the electrons.
In FY instead, the measured effect is connected to the secondary generations of the hole recombination. In fact, whereas the main channel of hole recombination is through the Auger process, a small percentage of holes recombine through the fluorescence channel. In this case, the emission is proportional to the absorption coefficient. The proportionality is not exactly direct because of nonlinear effects linked to the "self absorption" process [70], caused by the absorption of the generated fluorescence radiation that is escaping from the sample. This process can be greatly reduced in case of diluted samples or thin films. Due to the large photon penetration depth, the probing is not limited to the few surface layers. Therefore FY is more a bulk measurement with respect to TEY. As the the Auger channel contribution decreases with the atomic number, FY is the preferred technique for heavy elements, whereas TEY is usually employed for lighter elements. Depending on the photon range, the employed detectors in FY are MCPs or silicon/germanium diodes.

2.3.3   CiPo beamline

The Circular Polarization (CiPo) [71] beamline has been developed specifically to study the dichroism both in the low-energy (5-200 eV) and in the high-energy (200-1200 eV) range. The configuration has been purposely designed to allow measurements on magnetic and natural dichroism, magnetic extended X-ray absorption fine structure, spin-resolved photoemission, two-photon absorption experiments, and vacuum ultraviolet ellipsometry. Accordingly, the insertion device is capable to generate linear and highly circular polarized radiation in the whole energy range. The insertion device at CiPo is an electromagnetic elliptical wiggler (EEW) where the vertical and horizontal magnetic fields are generated by electromagnets. By varying the currents it is possible to generate both linear and circular polarized light, whereas by reversing the horizontal current the helicity can be inverted.
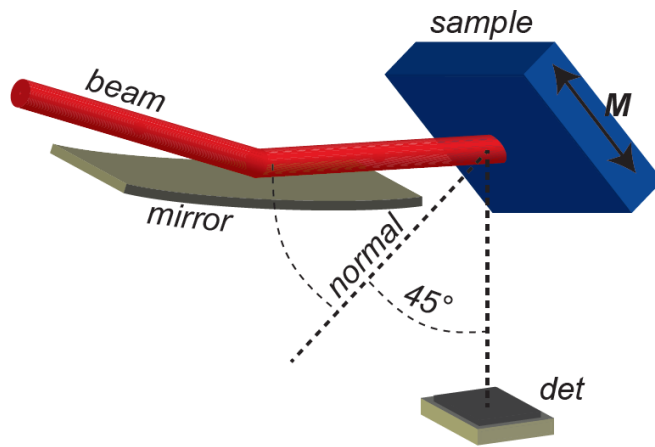

Figure 2.6: Experimental configuration of the sample with respect to the synchrotron radiation beam and the magnetic field **B** at the CiPo beamline. The I_0 signal is taken from the toroidal refocusing mirror gold surface. The external magnetic field is along the incoming radiation direction. A silicon diode detector was positioned at $45°$ from the sample normal in order to collect the reflected radiation.

The broad photon range (5-1200 eV) can be tuned by setting the correspondent vertical and horizontal currents to produce an emission peak of around 8-10 eV FWHM, which is then monochromatized with grazing incidence spherical grating monochromators in a Padmore configuration [72]. For the low-energy measurements that were collected during this work, the

grating resolving power was 8100 and the polarization degree was 90 %. Moreover, the entrance slits can be adjusted to further peak the beamline emission. The beamline optic elements are gold-coated mirrors at 2.5° grazing angle. The last mirror is intended to focus the radiation to the sample and for this scope is toroidal, with a magnification equal to one.

The intensity I_0 of the beamline is obtained by the photocurrent generated on the last mirror, which is then digitalized by a multimeter. The XMCD end-station allows for absorption experiments and is equipped of an in-axis electromagnet generating up to 0.4 T. The sample is mounted on an insulating support, which allows to measure the total electron yield from the sample as the drain current by a multimeter. Moreover, by working away from normal incidence, it is possible to recollect the reflection from the sample by a silicon diode, which is then measured by an amperometer.

Characterization of Ni/Si$_3$N$_4$/Si heterostructures

The interfaces between metals and semiconductors play a fundamental role in current semiconductor technology. According to their character, they are broadly divided in three categories: ohmic, tunneling and Schottky contacts.

3.1 Ohmic and tunneling contacts

If two electrodes are separated by a sufficiently thin insulating layer, a current can flow between the two electrodes due to the tunnel effect. Tunneling through potential barriers was hypothesized and studied since the first derivations of quantum mechanics. In the same years of the derivation of the Schrodinger equation, the semiclassical method WKB [73] was developed. Later in the thirties, the work of Sommerfeld, Bethe and Holm put forward the WKB model to the case of an arbitrary applied voltage at the interface [74, 75]. These first works considered a rectangular barrier and added the effect of image potentials at the interface, but the resulting equations could be solved only numerically. The following years saw the attempt to closely model the shape of the barrier and thus improve the precision of the predictions.

No general formula can therefore describe the flow of the current at the interface, as the problem involves the analytical calculation of the tunneling through a general potential barrier via WKB [76], further complicated by the presence of electrons and holes that see different potential barrier heights. The problem can be set up by starting with a general unidimensional potential V(x) and then calculate the transition probability $\Theta(E_x)$ with WKB

$$\Theta_C(E_x) = exp\Big[-2 \int_{x_1}^{x_2} |k_x|\, dx \Big]$$

where k_x is the component of the complex electron wave vector within the insulator I along the x direction (perpendicular to the interface). As the real moment is a vector in the 3D space, the transverse component k_t will form with the x-direction one the total momentum k_I, so that

$$k_x = \sqrt{k_I^2 - k_t^2}$$

Considering the reduced valence and conduction band masses in the insulator as equal [77], the energy dispersion of the bands in the insulator can be simplified so that the total momentum results as

$$k_I = \frac{\sqrt{2m_{CI}^*}}{\hbar} \sqrt{E - E_{CI}}$$

where m_{CI}^* and E_{CI} indicate respectively the reduced mass and the energy in the insulator I conduction band. Combining the two previous expressions, the x-direction momentum can be derived as

$$k_x = \frac{\sqrt{2m_{CI}^*}}{\hbar} \sqrt{E_x - E_{CI}}$$

where E_x is the energy associated to an electron whose momentum is on the x direction. The tunneling probability thus assumes its usual representation as

$$\Theta_C(E_x) = exp\left[-\frac{4\pi}{\hbar} \int_{x_1}^{x_2} \sqrt{E_x - E_{CI}}\, dE_x \right]$$

As can be seen, the evaluation of the transition probability requires the knowledge of the band structure in the insulator region. To calculate the total current density, the two contributions must be summed, as the exchange of electrons between the metal M and the semiconductor S occurs in both directions. If we consider only the conduction band and neglect the holes, the net electron current is obtained by summing the transition probability at fixed transverse energy E_T over all the allowed energies in the x direction and by taking in account the free states in the metal M and the semiconductor S

$$j_c = \frac{4\pi e m_C^*}{h^3} \int_{E_{CO}}^{E_{CI}} dE_x \Theta_C(E_x)$$

$$\int_0^\infty dE_T \left(\frac{1}{1 + exp\left(\frac{E_T + E_x - E_{FS}}{kT}\right)} - \frac{1}{1 + exp\left(\frac{E_T + E_x - E_{FM}}{kT}\right)} \right)$$

Ohmic contacts form instead when the electrical properties vary narrowly and smoothly at the interface. This condition can be obtained for example by employing a heavily-doped semiconductor, which reduces the potential barrier at the interface, or by allowing the mixing of the two species into an alloy at the interface. As a result, the current is linear to the applied voltage, hence the name "ohmic". For the heavily doped Si, the tunneling through the narrow barrier is the dominant process; the tunneling current j can be written as [78] (more details in the following section)

$$j = j_0 \, exp\Big(- \frac{\phi_B}{E_{00}} \Big)$$

where ϕ_B is the Schottky barrier height and E_{00} is a characteristic energy which is defined as

$$E_{00} = \frac{q\hbar}{2} \sqrt{\frac{N_D}{m^* \epsilon}}$$

where N_D, m^* and ϵ are respectively the electrically active dopant concentration, the effective mass and the dielectric constant of the semiconductor. The parameter that describes an ohmic contact is the contact resistance, which generally depends on the metal and the semiconductor electric properties [79].

$$R_C = (\partial J / \partial V)^{-1}|_{V=0} \propto exp\Bigg(\frac{\phi_B}{E_{00} \, coth(E_{00}/kT)} \Bigg)$$

3.2 Schottky barrier

Rectifying properties at metal-semiconductor contacts were first reported in 1874 by Braun [80]. Following the observation of a strong *unilateral conduction* that deviated from Ohm's law, Braun postulated that a thin interface layer could be present between the two contacts, but he misidentified this layer as air. In 1929, Schottky and Deutschmann confirmed the presence of a barrier layer of an estimated thickness of about 0.3 μm [81]. Schottky was the first to explain the rectifying properties by introducing a space charge layer on the semiconductor side, depleted of mobile carriers [82], and mirrored by an equal charge at the metal surface. These interfaces are known as Schottky barriers to acknowledge the contribution of Walter Schottky, who firstly attributed correctly their properties to space charge layers. The

transport at these interfaces is governed by the barrier height of the depletion layer, defined as the distance between the Fermi level and the valence band top (or the conduction band bottom) at the interface for a p-doped (n-doped) semiconductor. However, the estimation of this energy proved challenging, as the first simplistic attempt to bring the vacuum levels of the metal and the semiconductor to the same value turned out to reproduce only partially the measured Schottky barrier heights. Further corrections invoked the presence of additional states at the interface that could partially accommodate the electrons in the space charge region [83]. The extreme case, i.e. the rectification is totally independent of the type of the metal, led to the idea that a strong pinning of the Fermi level in the semiconductor was responsible for the partial insensitivity. In the following 40 years, subsequent attempts were dedicated to pinpoint the physical nature of these defect-induced states. To name just a few, the formation of metal-semiconductor alloys at the interface can lead to the presence of dangling bonds at the semiconductor-alloy interface [84] that act as free states in the semiconductor. Or else, spatial inhomogeneities at the metal/semiconductor interface in the form of atomic steps, grain boundaries or metallic diffusion spikes [85] can generate fluctuations of the potential barrier, thus lowering the observed barrier. In summary, significant theoretical and experimental work has been devoted to metal-semiconductor interfaces. Unfortunately, the problem of barrier heights in Schottky contacts has turned out to be quite complicated, even though it is possible to reconcile the positions by allowing a continuum of states in the energy-forbidden region of the semiconductor [86].

The formation of a metal-semiconductor interface can be explained in a Gedanken experiment, as exemplified in Fig. 3.1. The distance between two surfaces of a metal and a semiconductor will be gradually reduced until the contact is finally established. If the two materials are externally connected by a wire, their Fermi levels E_F are aligned and the thermal equilibrium is established. In particular, the Fermi energy in the metal and its work function ϕ_m will remain unperturbed. Instead, the semiconductor Fermi level will be changed by an amount equal to the difference of the metal work function and the semiconductor work function. As the semiconductor does not have free states in the gap, its "effective" work function is defined as

$$\phi_{s0} = \chi_s + \phi_s$$

where χ_s is the semiconductor electron affinity and ϕ_s is the difference between the Fermi energy E_F and the conduction band minimum energy E_c in the semiconductor bulk. At the interface charge neutrality must be
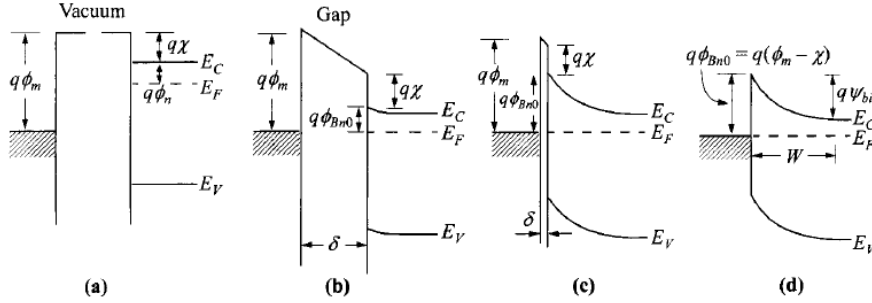
Figure 3.1:   Energy bands associated to the formation of the metal-semiconductor contact. The metal and the semiconductor will align the Fermi energy E_F as the system passes from separated systems (a) to a single connected system (b). As the gap δ approaches 0, the diffusion potential ϕ_{bi} (indicated elsewhere in the text as V_d) increases until the formation of the Schottky barrier. Reprinted from [87], p. 135.

established, namely

$$Q_m + Q_s = 0$$

The electric field generated by these charges penetrate both the metal and the semiconductor, but because of the Thomas-Fermi screening, on the metal side the penetration is in the order of less that 1 Å and can therefore be neglected. On the semiconductor side, instead, we have to consider the Debye length, which is generally orders of magnitude bigger than the Debye length of a metal. Therefore, a region of the semiconductor will experience a penetration of the electric field, resulting in the formation of a space charge layer. The charge Q_s is evenly distributed in the space charge layer and, depending on the specific case, can be positive, implying a depletion of mobile charges, or negative, if instead there is an excess of electrons. By combining the Poisson equation at the interface with the knowledge of the spatial density of electron and holes from the bands and from the impurities, it is possible to write the surface density of electrons as [88]

$$Q_s = eN_dL_d = \sqrt{2\epsilon_b\epsilon_0 N_d(eV_d - k_bT)}$$

where L_d is the depletion layer thickness, and ϵ_b and N_d are the relative dielectric constant and the impurity density of the semiconductor, and V_d is the diffusion potential defined as

$$eV_d = \phi_{B,0} - \phi_s$$

where $\phi_{B,0}$ is the height of the potential step at the interface, or Schottky barrier height. This potential is a manifestation of a distortion of the bands caused by the penetration of the electric field in the semiconductor. The total band bending at the interface will be V_d and, consequently, the "effective" work function will change of the same amount V_d. Resuming again the previous Gedanken experiment, treating the systems as a two-plate capacitor at a distance δ, the surface charge density at the interface is given by

$$Q_s = \frac{\epsilon_0}{e} \frac{\Delta\phi_0 - eV_d}{\delta}$$

where $\Delta\phi_0$ is the difference between the two work functions ϕ_m and ϕ_{s0}. Combining with the previous expression for the surface charge density

$$\frac{(\Delta\phi_0 - eV_d)^2}{eV_d} = 2e\frac{\epsilon_b}{\epsilon_0}N_d\delta^2$$

can be obtained, which in the limit of vanishing gap allows to rewrite the equation as

$$\phi_{B,0} = \phi_m - \chi_s$$

This is the Schottky-Mott rule, stating that for an ideal metal-semiconductor contact the Schottky barrier height is equal to the difference between the metal work function and the semiconductor electron affinity.

3.2.1   Interface states

Experimentally, the Schottky-Mott rule does not correctly describe the Schottky barrier height. The discrepancy is especially evident in Fig. 3.2, where the experimental points have been compared to the expected linear trend. This discrepancy has been attributed to interface states within the semiconductor band gap that absorb part of the charge build-up. Accordingly, charge neutrality has to be written as

$$Q_m + Q_i + Q_s = 0$$

where the interface charge Q_i resides in a layer of width δ_i. In fact, when the periodic structure of a lattice is terminated, surface-specific states form. In particular, in the semiconductors these states tend to be localized in
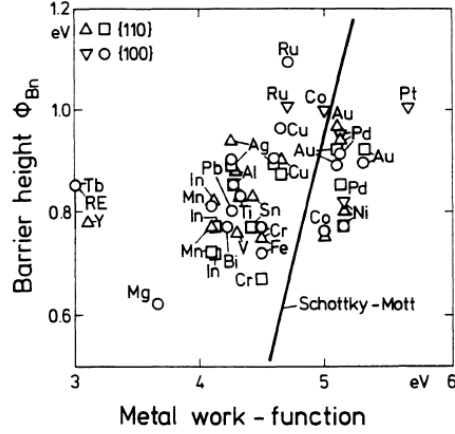
Figure 3.2: Experimental barrier heights of GaAs Schottky diodes against metal work function ϕ_{Bn}. The straight line represents the Schottky-Mott rule. Reprinted from [88], p. 311.

the band gap. Furthermore, the creation of metal-semiconductor chemical bonds at the interface can also lead to the formation of similar mid-gap states. Lastly, the presence of the metal causes the formation of metal-induced gap states (MIGS) because of the tails of the metal electron wave functions penetrating in the semiconductor E_v - E_F energy range, as shown in Fig. 3.3. According to their position within the band gap, all these kinds of states can behave as acceptors or donors. The effect of these levels is to pin the semiconductor Fermi energy within the band gap. The charge neutrality level (CNL) is central to the Fermi-level pinning. The CNL is defined as the energy at which the filling of these states does not add net charge at the interface. If the CNL - referred to the Fermi energy - is below the Fermi energy, it will result in an excess of positive charges at the interface. Schematically, the density of states for these defects D_{GS} can be considered as constant near the CNL, leading to the surface charge density of the gap states being described as

$$Q_{gs}^{mi} = eD_{GS}(\phi_B + \phi_{CNL} - E_g)$$

As both Q_m and Q_{gs}^{mi} reside at either side of the interface, an electric double layer is formed at the interface. This implies a charge transfer across the contact, which according to Pauling can correlate to the electronegativities X of the involved elements

$$Q_{gs}^{mi} \propto X_m - X_s$$

This additional charge causes an additional energy barrier Δ, as seen in Fig. 3.3, and is linked to the metal charge as

$$\Delta = \phi_m - \chi_s - \phi_B = -e\frac{Q_m}{\epsilon_i \epsilon_0}$$

where ϵ_i is the interfacial dielectric relative constant. The charge neutrality can be rewritten as

$$\phi_m - \chi_s - \phi_B = -\frac{e^2 D_{GS}\delta}{\epsilon_0 \epsilon_i}(\phi_{CNL} - E_F) + \sqrt{\frac{2N_d\delta^2\epsilon_b}{\epsilon_0\epsilon_i}}\sqrt{eV_d - k_bT} =$$
$$- \alpha(\phi_{CNL} - E_F) + \sqrt{V_1(eV_d - k_bT)}$$

As this interface charge density occurs on a subatomic distance, it can be fairly estimated as $\delta \simeq 2$ Å and take $\epsilon_i = 1$. For densities N_d as high as $10^{17}cm^{-3}$ the term V_1 corresponds to an energy of 0.002 eV, hence the last term can be neglected. Finally, it should be noted that in case of no interface charge, the CNL coincides with the Fermi energy and the barrier height is obtained as $\phi_{B,0} = E_g + \phi_{CNL}$. Thus, the correct form of the barrier height in case of the presence of MIGS is

$$\phi_B = S_\phi(\phi_m - \chi) + (1 - S_\phi)\phi_{B,0}$$

where $S_\phi = 1/(1+\alpha)$. The Schottky-Mott rule is obtained in the limit of $S_\phi = 1$, or $D_{GS} = 0$, whereas in the opposite case - which is called Bardeen limit - the $D_{GS} \rightarrow \infty$ and the Fermi level is pinned at the CNL.
A further effect to consider at a real Schottky barrier is the image-force lowering. In fact, the minimum energy for extracting an electron from a surface is the work function, but as the electron is at a distance x from the surface, it induces a positive charge at -x that exerts a force on the electron. If at the same time the electron is subject to an electric field, as is the case at a metal-semiconductor interface, the total potential energy can be written as

$$E(x) = -\frac{e^2}{16\pi\epsilon_0 x} - e|\mathscr{E}|x$$

The maximum of this potential energy represents the image force lowering $\delta\phi$ experienced at the interface

$$\Delta\phi = \sqrt{\frac{e|\mathscr{E}|}{4\pi\epsilon_b\epsilon_0}}$$

where $|\mathscr{E}|$ is taken as the maximum electric field at the interface, as the electric field is not constant with distance. At high fields this correction can reduce considerably the effective barrier height the electrons have to surmount to be added to the thermionic emission.
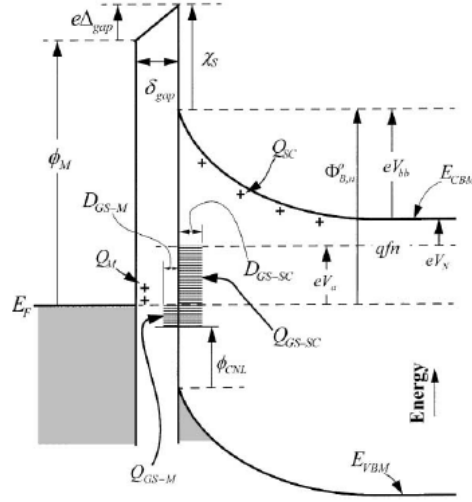

Figure 3.3: Detailed energy-band diagram of a metal-n-semiconductor contact with an interface layer δ_{gap} (vacuum) of the order of atomic distance. In particular, the charge-neutrality level ϕ_{CNL}, the metal-induced gap states D_{GS-M} and D_{GS-SC} (indicated elsewhere in the text as D_{GS}) and the space charge density Q_{SC} (Q_s) are depicted. Reprinted from [89], p. 82.

3.2.2 Thermionic emission

The mechanism associated to the current flow at a Schottky barrier is the thermionic emission. Under the assumption that the barrier height ϕ_B is bigger than the thermal energy k_bT, that the system is at thermal equilibrium and that the flow does not alter significantly the equilibrium properties of the system, two fluxes of charges - from the metal to the semiconductor and

vice versa - are superimposed. The shape of the barrier profile is therefore fixed and the current depends only on the barrier height. From the semiconductor, an electron must have sufficient energy to overcome the potential barrier, so that the flux results

$$J_{s \to m} = \int_{E_F + \phi_B}^{\infty} e v_x \, dn$$

In the limit of a parabolic conduction electron band, the density can be written as

$$dn \approx \frac{4\pi (2m^*)^{3/2}}{h^3} \sqrt{E - E_c} exp\Big(- \frac{E - E_c + \phi_B}{k_b T} \Big) dE$$

if the energy of the electrons is only kinetic energy, $E - E_c = 1/2 m^* v^2$, so that

$$J_{s \to m} = 2e\Big(\frac{m^*}{h}\Big)^3 exp\Big(- \frac{\phi_B}{k_b T} \Big) \int_{v_0}^{\infty} v_x \Big(- \frac{m^* v^2}{2 k_b T} \Big) 4\pi v^2 \, dv =$$
$$\frac{4\pi e m^* k_b^2}{h^3} T^2 exp\Big(- \frac{\phi_B}{k_b T} \Big) exp\Big(- \frac{m^* v_{0x}^2}{2 k_b T} \Big)$$

The minimum kinetic energy $1/2 m^* v_{0x}^2$ required to surmount the energy barrier is given by $e(V_s - V)$ for an applied voltage V. Thus, the current can be written as

$$J_{s \to m} = -\frac{4\pi e m^* k_b^2}{h^3} T^2 exp\Big(-\frac{\phi_B}{k_b T}\Big) exp\Big(\frac{qV}{k_b T}\Big) = A^* T^2 exp\Big(-\frac{\phi_B}{k_b T}\Big) exp\Big(\frac{eV}{k_b T}\Big)$$

which is called the Richardson law for the thermionic effect. Since under bias the barrier height remains unaffected, the current from the metal into the semiconductor is not sensitive to the applied voltage. As a result, its contribution must be equal and opposite to the current in the other direction when the system is in thermal equilibrium, i.e. at $V = 0$

$$J_{m \to s} = -A^* T^2 exp\Big(- \frac{\phi_B}{k_b T} \Big)$$

so that the total current results

$$J_{TE} = -A^* T^2 exp\Big(- \frac{\phi_B}{k_b T} \Big) \Big[exp\Big(- \frac{V}{k_b T} - 1 \Big) \Big]$$

However, the total current can deviate from the theoretical value due to the effect of the coexistence of the tunneling current and the recombination of charges that can occur within the depletion layer. These effects are usually factored by a dimensionless experimental term η called the "ideality factor", which approaches the unity in case of no spurious effect. As a result, the current through a Schottky barrier follows the law $J = J_0[exp(qV/\eta k_B T) - 1]$, where J_0 is the saturation current density obtained by extrapolating the current at V=0.

3.3   Sample growth

Metal-semiconductor contacts are usually grown in vacuum conditions by evaporating the metal on a polished semiconductor surface [90]. Depending on the kind of contact being made, the semiconductor surface can be bare, present a native oxide or be passivated with the growth of a non-reactive interlayer. Accordingly, metal-semiconductor alloys by solid-solid metallurgical reactions can form at the interface even at comparatively low temperatures. In the case of silicon, a vast group of transition metals form stochiometric alloys called silicides with good electrical properties. As a result, the metal silicide-silicon contact behaves like a metal-silicon contact exhibiting stable electrical and mechanical properties. In particular, the resulting Schottky barriers show quite a strong Fermi level pinning. In semiconductor technology sometimes this property is preferred, since it provides more reliable and reproducible Schottky barriers and the interface chemical reactions are well defined and can be kept under good control [87].
Nickel silicides play a special role in this area; in fact, they are an extensively studied subject - because of the easiness in growing them and their consequent ubiquitous presence in semiconductor devices - and are known to be created in a wide range of growth techniques. Si contacts with Ni can form uniform and well-defined alloyed interfaces and due to the low energy required to form them are known to occur even at room temperature [11, 12]. Of the possible Ni alloys, only three - namely Ni_2Si, $NiSi$ and $NiSi_2$ sorted per increasing formation temperature - are originated by the contact reaction [91]. Generally, the compounds grow consecutively one by one, as the reaction temperature increases; for Ni_2Si the formation temperature is in the range 200-350 °C. Thus, when a nickel film reacts with a silicon wafer, the first phase formed is Ni_2Si; only when all the Ni is consumed, then $NiSi$ forms, and after all the Ni_2Si is consumed, $NiSi_2$ will form between $NiSi$ and Si. In any case, the formation of silicides should start with the breaking of

the Si covalent bonds. However, the amorphous transition temperature of Si is much higher than Ni silicide formation, therefore the bond breaking must be assisted by the interstitial diffusion of the metal [92]. Indeed, experimentally, Ni can diffuse across a Si wafer rather quickly [93] and lead to charge transfer from the covalent Si-Si bond to metallic NiSi bonds, thus easing the following breaking of the bond.

This study investigated metal/semiconductor interfaces and therefore involved the growth of thin Ni films on Si substrates. In the present case, a sample as homogeneous as possible that could exhibit a sharp chemical transition was needed. In fact, it can be speculated that a high-quality and sharp transition enables the maximum spin transport at the interface since it has the least number of discontinuities at the interface. Furthermore, a clear spatial separation was needed with the aim at decoupling the dynamics of the metal and the semiconductor. Accordingly, it was necessary to develop a sample growth technique that could reduce the interdiffusion of atoms at the interface as much as possible. Hence, two approaches were used: on the one hand the growth of a thin mechanically rigid interlayer acts as a barrier, whereas on the other hand the subsequent metallic film growth at liquid nitrogen temperature in a two-step technique [15] subtracts the energy needed for the diffusion. The chosen interlayer material is silicon nitride due to its unique properties. Si$_3$N$_4$ can be grown as a thin crystalline bilayer on Si (111) by thermal nitridation at high substrate temperatures. The crystalline growth on the Si (111) surface is allowed by the almost perfect lattice match of the two materials and, furthermore, it is a self-terminating reaction until the growth of a bilayer [13]. In particular, the employed growth technique included the outgassing and the subsequent flashing of the Si substrate at high temperature (1500K) to allow the desorption of any impurity and the Si (111) 7x7 surface reconstruction. Then, by exposing the surface at 1050 K to 100 langmuirs of ammonia while the sample was held at 1050 K, the formation of a bilayer of β-Si$_3$N$_4$ was allowed. Nickel was then deposited by an effusion cell while the sample was kept at liquid nitrogen temperature. This protocol enabled the formation of a flat polycrystalline Ni layer [15]. The deposition rate was calibrated with the reduction of a resonance peak on a polished Cu surface by XPS. Finally, after leaving the sample slowly recovering to room temperature, a capping layer was lastly deposited to prevent metal oxidation. At each growth step an XPS spectrum was collected to follow the deposition and verify the quality of the samples. Furthermore, after the growth, the samples were characterized by HRTEM.

Ultrathin thermal Si$_3$N$_4$ layers in p- and n-type Si Schottky barriers have been already studied as a function of the thickness of the nitride layer [94].

In particular, these devices show near unity ideality factors - not display-
ing any form of "pinning" - and have a barrier height that varies linearly
with the nitride thickness. According to Ref.s [14, 16], the interlayer nitride
thickness is in the range 0.6-0.8 nm, from which a p-type Si Schottky barrier
height $\Phi_B = 0.02$ eV can be extrapolated. In this work, three samples were
grown employing the same growth technique and differing only in the Si
substrate doping. In table 3.1 the main parameters are given; all the three
substrates were B-doped. Specifically, the depletion layer thickness can be
calculated using the expression from the previous section, where eV_d is the
difference between the Schottky barrier Φ_B and the Fermi energy E_F, the
latter being linked to the semiconductor doping by [95]

$$\Delta E_F = k_B T \, arcsinh \left(\frac{N_D}{2n_i} \right)$$

where Δ denotes that a doping induces a shift of the Fermi energy to a
level near the semiconductor valence (conduction) band and where N_D and
n_i are respectively the doping density and the intrinsic doping, the latter
being equal to 9.7 10^9 cm^{-3} [96] for Si at 300 K.

sample	ρ (Ωcm)	N_D (cm^{-3})	ΔE_F (eV)	L_D (nm)
LD	1-20	1.5e15	0.359	520
MD	0.05	3.5e17	0.450	41
HD	0.005	2.1e19	0.556	6

Table 3.1: LD, MD and HD resistivity, dopant density, Fermi energy shift
(with respect to $E_g/2$) and depletion layer thickness. For the low-doped
sample LD, the dopant density in the resistivity range according to Ref.
[97] has been calculated and the mean values for the Fermi energy shift and
depletion layer thickness in the same range have been indicated.

Ref. [16] discusses in great detail the Ni/Si$_3$N$_4$/Si interfaces with both
HRTEM and XPS. Contrary to expectations, the sub-nanometer interlayer
of crystalline Si$_3$N$_4$ avoids only partially the diffusion of the metal in the
substrate. In particular, where the thermal stress accumulated during the
growth creates small cracks in the interlayer, a diffusion of Ni atoms occurs,
resulting in the formation of discontinuous silicide areas. These areas are
confined right below the interlayer and are of a composition which is com-
patible with NiSi$_2$. Still, this additional region is less than 3 nm thick and

its spatial distribution is discontinuous, with significant parts of the sample which do not show such a diffusion. As in the ideal case, these free areas allow spin injection, therefore the presence of silicides can at most reduce the observed effect. This silicide layer does not prevent the observation of a magnetic effect in the substrate not least because these silicides are nonmagnetic.

3.3.1   XPS

XPS spectroscopy allows to obtain quantitative information on the chemical composition of the surface. Monochromated x-rays impinging on the sample produce photoelectrons that are subsequently energy-resolved. XPS spectra basically probe only the first few monolayers of the sample. The probing depth is governed by the electron inelastic mean free path (IMFP) and therefore by the grazing angle and the kinetic energy of the emitted electrons. For kinetic energies in the ranges of 50-300 eV, the electron mean free path assumes a minimum value of about 0.5-1.5 nm [98].
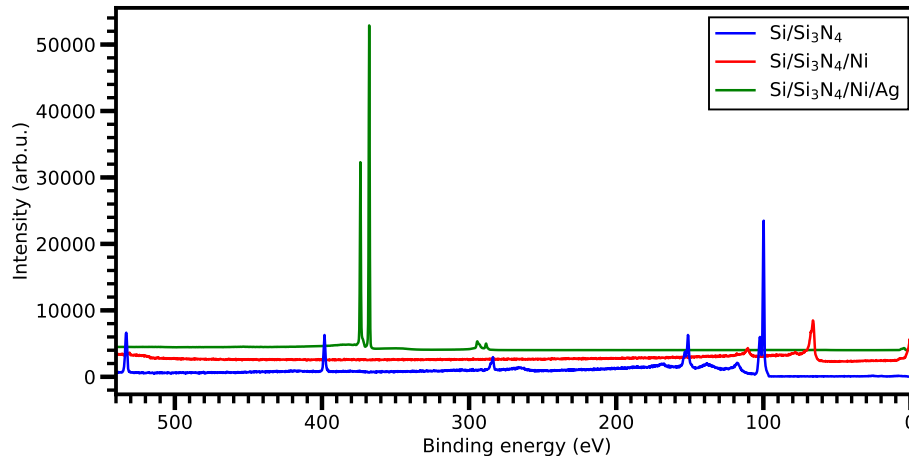
Figure 3.4:   Photoemission survey scans on LD taken at 650 eV photon energy. The spectra have been taken after the nitridation on the Si/Si$_3$N$_4$ sample (blue), after the Ni film deposition (red) and after the deposition of the Ag capping layer (green).

Sample MD was the first object of study, followed by a second experiment carried on both LD and HD samples. To simplify the analysis, XPS data on LD and HD only will be shown, as no additional information is gathered from XPS studies on MD, which have also been reported in Ref. [16]. LD
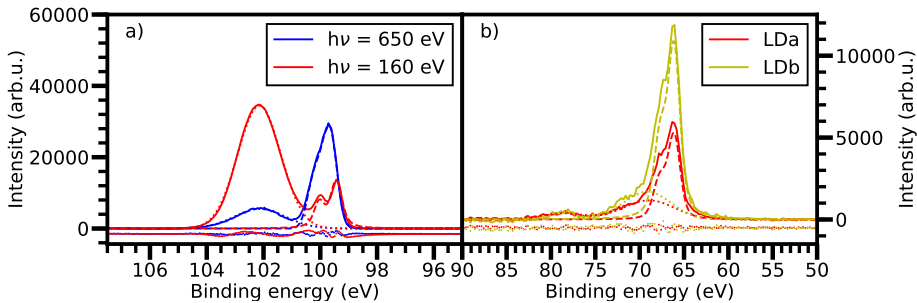
Figure 3.5: Panel (a): the Si 2p core level spectrum on LD taken at 650 eV (blue) and at 160 eV (red) are shown; the fitting of the double-peak related to the Si bulk is shown in both cases in dashed line, whereas the Si-N nitride peak is shown in dotted line. Panel (b): the Ni 3p core level spectra on LDa (red) and LDb (yellow) are shown; the fitting of the double-peak as well as the two satellites are shown in dashed and dotted lines respectively. For experimental restraints, the two spectra are collected at two different angles of the sample, whence the different height. Below the two panels, the residual is shown as well.

and HD samples were grown in a two-step. First the silicon substrates were passivated using the above mentioned technique and then were broken in two pieces. Then the same two pieces underwent the same metal deposition; for both LD and HD one of the samples was sacrificed for the HRTEM measurements, whereas the second was used for the static and dynamic studies.

In Fig. 3.4 the XPS survey spectra on LD are shown. For the Si substrate, the spectra were corrected so that the peaks at the N core level matched the expected binding energy. In fact, the intensity at the valence band was too low to obtain a robust value for the Fermi energy. Vice versa, the spectra taken after the metal deposition showed a clear Fermi energy step, which made the correction of the binding energy position possible. The bottom spectrum shows the Si/Si_3N_4 surface; the peaks related to the Si 2p and Si 2s are clearly visible, as well as the N core level. The distinctive peak related to the Si-N bond is clearly visible on the left side of the Si 2p and Si 2s peaks [99, 100]. On the passivated surface, contamination of O and C are also present. After the metal deposition, carbon contaminant remained buried within the Si substrate, as no trace is visible, whereas traces of oxygen can still be seen. The middle spectrum was taken after the Ni deposition; the peaks from the Si substrate are completely vanished due to

the surface sensitivity of the probe. The top spectrum was taken after the last deposition of Ag; the peaks pertaining to the Ni are greatly reduced.
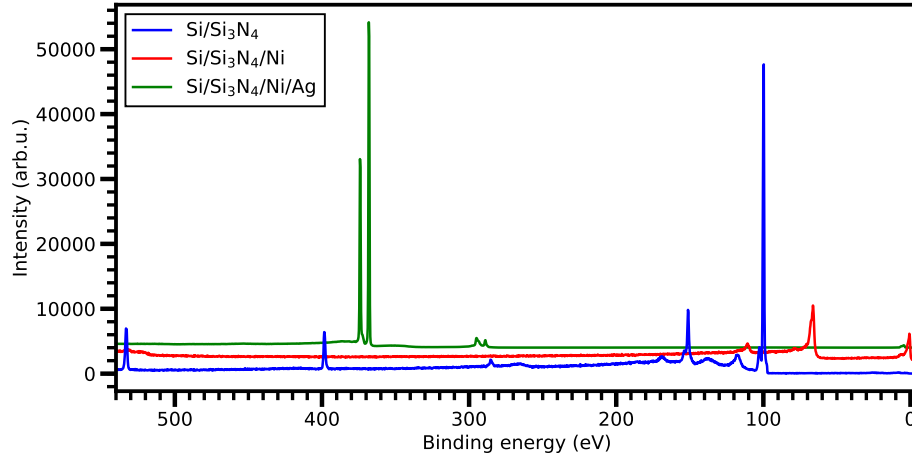

Figure 3.6:   Photoemission survey scans on HD taken at 650 eV photon energy.
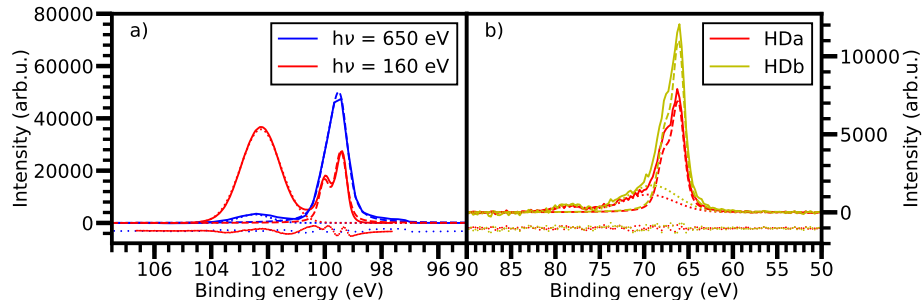

Figure 3.7:   The Si 2p core level spectrum on HD (a) and the Ni 3p core level spectra on HDa (red) and HDb (yellow) are shown (b).

Figure 3.5 a) and b) show instead the LD sample high resolution spectra of the Si 2p and the Ni 3p peaks, respectively. In panel a) the Si 2p peak displays the spin-orbit split double-peak pertaining to the Si substrate at 99 eV, as well as the Si-N peak at 102.1 eV. The two spectra are taken at high and low photon beam energy; the change of the ratio between the Si and the Si-N peak is due to the XPS being more surface sensitive at the lower energy (KE = 60 eV) than at the higher one (KE = 550 eV). In panel b) the Ni 3p peak shows similarly a double-peak structure at 66 eV, as well as

the two satellites at higher energies [101, 102].
Figures 3.6 and 3.7 show the same peaks for the HD sample.

3.3.2 HRTEM-HAADF

Transmission electron microscopy (TEM) is capable of tremendous spatial resolution up to the single atom as a direct result of the high energy electrons that are employed. The electrons are produced by a heated filament and then are accelerated and chromatized by means of magnetic fields and electromagnetic lenses. A high vacuum is needed to prevent the scattering of the electrons before reaching the sample. Along with the crystallographic structure of the sample, the atomic-resolution images can provide the chemistry as well.
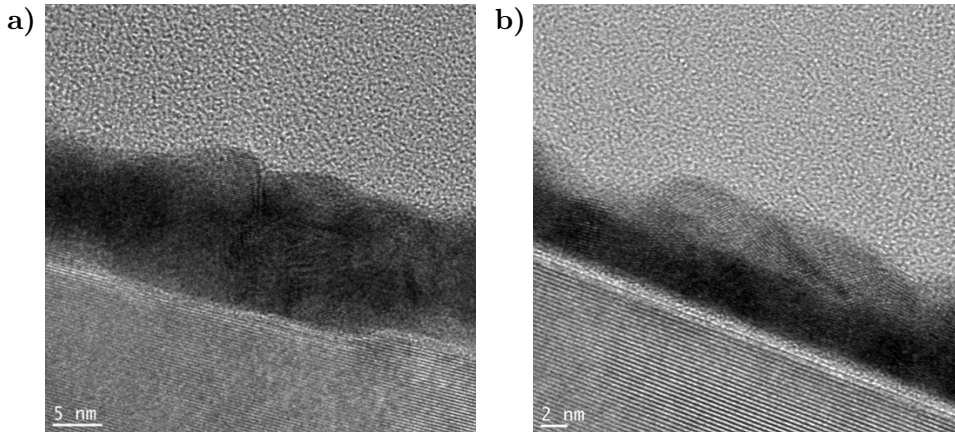
Figure 3.8: HRTEM characterization on LD (panel a) and HD (panel b). On the lower side the crystalline Si substrate can be identified. The substrate is surmounted by a thin brighter layer, which is the crystalline Si_3N_4 interlayer. The darker layers above correspond to the Ni magnetic layer and the Ag capping layer. According to the atomic distances, the Si_3N_4 thickness is 0.7-1.0 nm for the two samples, whereas the Ni film thickness is 10 ± 2 nm for LD and ~ 7 for HD. The Ni film appears polycrystalline and uniform.

As they penetrate the sample, the electrons that are scattered from the sample - both elastically and inelastically - can be recorded either in transmission or in reflection. Accordingly, the contrast is generated by the mass absorption, diffraction or phase. While diffraction and phase are geometric factors that are useful for determining the spatial structure of the sample, absorption is sensitive to the absorbance and therefore to the chemical struc-

ture of the sample.

The interfaces have been measured both in high-resolution TEM (HRTEM) - Fig. 3.8 - for the spatial part, as well as in the high-angle annular dark-field (HAADF) in Fig. 3.9. With HAADF, only the electrons scattered at higher angles are collected; as elements with higher Z scatter more electrons at higher angles, this technique is also called Z-contrast imaging. Z-contrast is sensitive to the local absorbance and accordingly exhibits an enhanced contrast, especially at lower atomic numbers, if compared to TEM.

As for the XPS characterization, only the analyses of the HD and LD samples are presented here. The HRTEM images presented in Fig. 3.8 show for both samples a clear contrast region between the semiconductor (lower part) and the metal (darker layer), with a continuous interlayer (bright strip) separating them. The thickness of the interlayer is found to agree with the theoretical expectations for a Si$_3$N$_4$ crystalline bilayer.
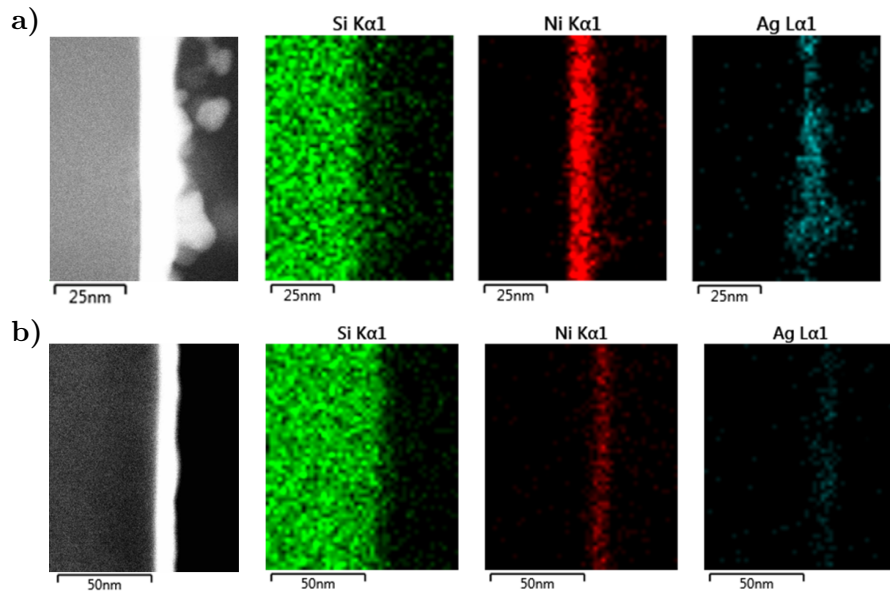

Figure 3.9: HAADF characterization of LD (panel a) and HD (panel b). The K edge of Si (green) and Ni (red) and the L edge of Ag (azure) were employed to derive the chemical selectivity. Due to the sensitivity to the higher Z, the brighter region corresponds to the heavier elements, as Ni and Ag, whereas the lighter elements as Si and N have reduced contrast.

The HAADF characterization in Fig. 3.9 reveals a substantially well-defined region in correspondence with metallic film, while conversely the
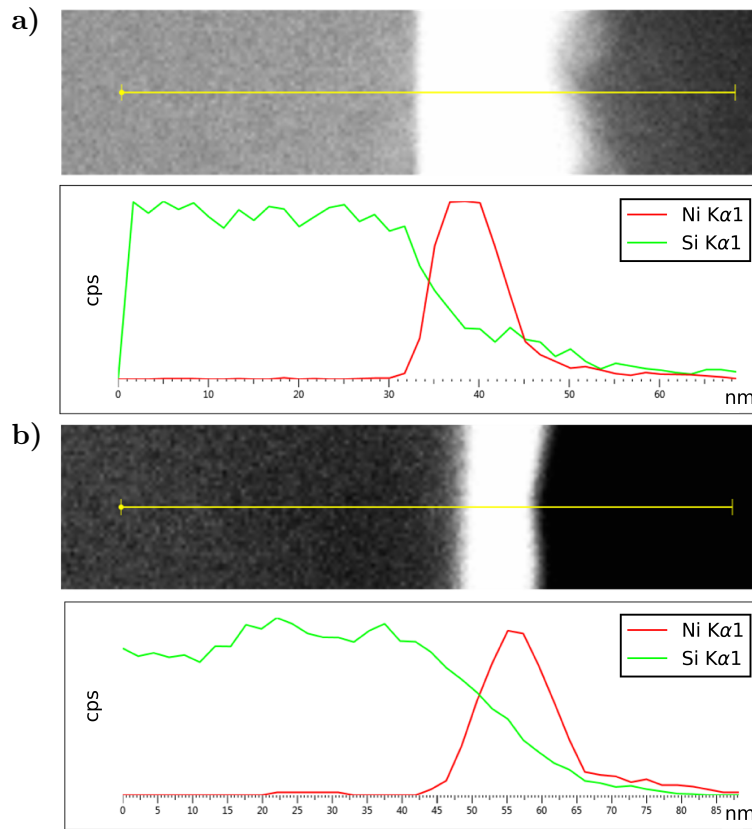
Figure 3.10: HAADF profile of LD (panel a) and HD (panel b) collected perpendicular to the layer deposition (yellow line). Whereas the Ni trace (red) is peaked at at the metal layer, the Si trace (green) stretches well within the Ni film.

Si species seems to penetrate well within the Ni film. This effect must be addressed cautiously; in fact, even though the positions of the atom species are well defined - and so their profiles transversely to the interface presented in Fig. 3.10 - the origin of their displacement may be due to the TEM preparation of the sample. Indeed, a sample thin enough to be transparent to electrons must be physically milled down to a few tens of nanometers in order to expose the heterostructure on the side, perpendicular to the milling direction. This is done first by mechanically polishing (or chemical etching) the surface, secondly by ion milling. The resulting thin wedged structure is then analyzed in reflection or in transmission. As a result of the high

mechanical and thermal stresses, some artifacts can emerge: ion implantation, sputtering of chemical species resulting in contamination as well as amorphization of layers [103] are common features. As Si is a comparatively light atom, during ion milling some atoms can be expected to be displaced and redeposited on the wedged sample, resulting in a contamination of the contiguous layers. As a result, while the profile of Ni is well-centered in the bright region defining the metallic layer, since the Si atoms are displaced, the resulting profile is smeared at the interface, as can be seen in Fig. 3.10.

Magnetic dynamics

4.1 Superdiffusive currents

In the range 100-1000 fs upon the optical excitation in a metal, a bath of electrons is excited by the laser and subsequently interacts with the metal through electron-electron scattering or electron-phonon scattering. As the Coulomb screening acts at the lower end of these timescales, the excitons created in the metal can act significantly. As a result, in this ultrafast heating process both electrons and holes diffuse. In parallel, as they diffuse, they lose energy because of scattering, which leads to a heat transport process too.

Let us suppose to excite a metal surface with an ultrafast laser; due to the very short penetration depth, only the first few nanometers will experience the excitation. In this layer electrons that absorb a photon will increase their energy by $\hbar\omega$, which corresponds to a kinetic energy increase of about 10^5 K. As a consequence, a small subset of the electron population is brought in an out-of-equilibrium state and by diffusion it will share the energy with the rest of the system. Simulations can prove that this diffusion of high energy electrons is *superdiffusive*, which in general is a term referring for a diffusion process for which

$$\langle r^2(t) \rangle = Dt^\alpha$$

in the case of $\alpha > 1$. The counterpart process of *diffusion* occurs for $\alpha = 1$, which is the classical behavior of the Brownian motion.

A sample under ultrafast heating can be treated as if it has all the states below E_F filled and all the states above it empty, as the thermal energies are negligible. The absorption of a photon promotes an electron to the conduction band leaving a hole below E_F. As the screening is extremely fast in the metal, the hole is rapidly screened by other electrons, leading to non-bound electron-holes pairs productions. Since the photon momentum

is negligible, electron momentum is randomized in direction; the high speed electron will then travel until the first scattering event occurs, where it will lose a portion of its energy randomizing its momentum again. The same fate will be experienced by holes. For electrons promoted from valence d-bands to conduction p-bands in transition metals, the velocities are in the order of 1 nm/fs and the scattering times in the order of 10 fs [104] (see Fig. 4.1).
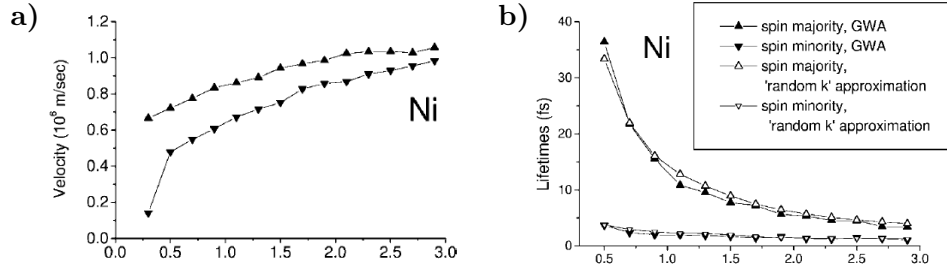

Figure 4.1: Transport properties of spin-majority and spin-minority electrons in Ni calculated by *ab initio* GW+T models. Panel a: the momentum-averaged velocities in Ni for spin-majority (up triangles) and spin-minority (down triangles) electrons. Panel b: The momentum-averaged electronic lifetimes in Ni for spin-majority (up triangles) and spin-minority (down triangles) electrons as calculated in GWA and "random k" approximation. All the data are expressed as a function of the total kinetic energy of the electron. Adapted from [104].

Depending on the scatterer, the scattering event will alter the final state. In e-e scattering, the high-energy electron will interact with an electron below E_F, resulting in the production of a new excited electron. Finally, at longer timescales, this electron channel will thermalize the electron ensemble, resulting in the formation of a Fermi-Dirac distribution of high-energy electrons. It is worth noting that this process will end up enhancing the transport, since it is a positive-feedback mechanism happening on the same timescale of the optical excitation. Instead, electron-phonon/impurities scattering will simply remove a portion of the energy from the electron ensemble. The latter, happening at longer timescales, can be neglected in the ultrafast part of the heating process.
As the timescales of the transport are comparable to the scattering time, the process is predominantly ballistic. In modeling the transport, we can consider each transport between an event of scattering ant the next as a generation; in fact, by neglecting any other scattering event, e-e scattering becomes a source of a new particle contributing to the transport. The

probability for a particle to be scattered can be written as [105]

$$P(s) = e^{\int_0^s ds'/\tau(s')v(s')}$$

having a particle moving ballistically along the s' coordinate at a velocity $v(s')$ with a characteristic scattering time $\tau(s')$. In the general picture, these parameters are space-dependent, but can be treated as constants in the homogeneous case. According to the probability, we can calculate the number of particles surviving after a time t at position s as

$$\varphi(s,t|s_0,t_0) = P(s)\theta(t-t_0)\theta\left(t-t_0-\int_{s_0}^{s}\frac{ds'}{v(s')}\right)$$

where the two Heaviside thetas account for a particle generated at t_0 and propagated from the generation s_0 up to the position s, respectively. The flux $\Phi(s,t)$ is simply the time-derivative of $\varphi(s,t)$. This picture considers a single particle, whereas for a distribution of electrons, the integral over the time and space has to be considered. As the initial distribution of electrons, the external source of excitation has will considered, i.e. the laser excitation in this model. This source S^{ext} will again be a function of time and space, so that in the 1-D case, the total flux will be calculated as

$$\Phi^{[1]}(z,t) = \int_{-\infty}^{+\infty} dz_0 \int_{-\infty}^{t} dt_0 \; S^{ext}(z_0,t_0)\Phi(z,t|z_0,t_0)$$

where the superscript [1] accounts for considering only the first-generation electrons. The calculated flux can then be inserted in the corresponding continuity equation as

$$\frac{\partial n^{[1]}}{\partial t} = -\frac{\partial \Phi^{[1]}}{\partial z} - \frac{n^{[1]}}{\tau} + S^{ext}$$

so that the total density of first-generation electrons $n^{[1]}$ will diffuse conforming to the flux $\Phi^{[1]}$ with a source term S^{ext} and a reaction term $n^{[1]}/\tau$, which accounts for the removal of the particles suffering scattering. In order to insert the other generations of electrons, it is necessary to consider what happens to an electron after scattering; the energy of the electron will be split to the scattering and scattered electrons according to the probability $P(\sigma,\sigma',E,E',z)$, which takes into account spins and energies of the two particles. As the removal of first-generation electrons is equal to $n^{[1]}/\tau$, the source of second-generation electrons can be defined as

$$S^{[2]} = \sum \int P(\sigma, \sigma', E, E', z) \frac{n^{[1]}}{\tau} \, dE'$$

The same continuity equation also holds for the new generation,if the superscripts are accordingly substituted. Defining the operator flux $\hat{\Phi}$ which operates on the source term $S = \sum S^{[i]}$, and the total density $n = \sum n^{[i]}$, the continuity equation that accounts for all the generations can be written as

$$\frac{\partial n}{\partial t} + \frac{n}{\tau} = \left(-\frac{\partial}{\partial z} \hat{\Phi} + \hat{I} \right) \left(S + S^{ext} \right)$$

where $\hat{I}$ is the identity operator. Is this transport superdiffusive? As the ballistic transport does not account for thermalization, to answer the question thermalization and transport must be decoupled, which can be achieved by considering the scattering being purely elastic. The integral

$$\sigma^2(t) = \int n(t, z)(z - z_0)^2 \, dz \propto t^{\alpha(t)}$$

will provide an answer. According to Ref. [6], the evolution of the α parameter evolves from 2 to 1, or from ballistic to diffusive, passing from the range $t << \tau$ to the range $t >> \tau$. The transition is smooth, as the increasing number of generated electrons conditions the overall behavior of the electron distribution.

The superdiffusive transport model made the prediction of the behavior of interfaces under the action of ultrafast laser pulses possible in different cases. In the ultrafast demagnetization of thin Ni films deposited on nonmagnetic Al substrates [105] a pump laser promotes both spin-up and spin-down electrons. Then, the generated electrons cause the displacement of an even larger number of electrons that in part diffuse in the substrate as well. Because of the big ratio $\tau_\uparrow / \tau_\downarrow$ between spin majority and spin minority in Ni, as shown in Fig. 4.1, within 100 femtoseconds the excited electrons are almost entirely spin-polarized. Within 300 femtoseconds the motion of the charges is greatly reduced, as well as the population of excited electrons. Without any spin-flip channels the magnetization dynamics is completed in 200 femtoseconds.

If Si replaces the substrate, it is possible to inject a spin current in the semiconductor [7]. In fact, the ultrafast demagnetization can trigger the injection of a highly polarized (80%) spin current. This is once again the result of the same big ratio $\tau_\uparrow / \tau_\downarrow$ in the magnetic metal, which causes a spin filtering of the electrons that reach the interface. Moreover, because of the

band gap in the semiconductor, a high number of low-energy electrons is reflected at the interface, whereas only the high-energy electrons cross the interface. Then, as the charges diffuse continuously into the semiconductor, to counterbalance the charge accumulation at the interface an electric field is induced to oppose any further electron injection. As a result, for $\sim \text{mJ/cm}^2$ laser fluences, the resulting spin injection in Si is in the order $10^{-2} \div 10^{-1}$ μ_B/atom. This can overcome the problem of the conductance mismatch at the interface, as the involved charges are high-energy electrons.

4.2 Description of the experimental conditions

Spin-based electronics, or Spintronics, has been considered as a natural development of semiconductor technology, as it would allegedly enhance the switching speed and lower the switching energy as well [106, 107]. For example, spin-polarized currents - which are the magnetic counterpart to electrical currents - are presumed to flow with almost no dissipation [1, 2]. Moreover, the spin coherence is longer with respect to the charge confinement lifetime [3]. As a result, there has been a growing interest in discovering reliable ways to generate spin-polarized currents inside semiconductors. Spin injection through superdiffusive currents at metallic interfaces has proved to be an effective approach to transfer magnetism from ferromagnetic films to nonmagnetic substrates [108, 109, 110, 111].

Spin injection in the current technology prevalent semiconductor has conversely been proven but not measured. Apart from the technological relevance, spin currents in Silicon are believed to be especially long-lived because of its small spin-orbit, its reduced nuclear spin as well as its crystal inversion symmetry [112, 113, 5]. Accordingly, as reported in the above mentioned studies, thin nickel films deposited on passivated silicon substrates have been chosen as an ideal system to study spin injection in the semiconductor. The purpose of this work is therefore to create an experimental benchmark to provide pivotal parameters that are still lacking [114, 115], such as the magnitude of spin accumulation, the spin lifetimes, and the spin current velocity. The investigation on the ultrafast magnetic dynamics at the interface has been carried out at the MagneDyn beamline using the time-resolved resonant magneto-optical Kerr effect [38, 116] at both the Ni $M_{2,3}$ and the Si $L_{2,3}$ absorption edges. It was possible to decouple the magnetodynamical response at the two edges thanks to the high quality of the interface, as well as the big energy separation between the edges of 35 eV which guarantees no overlapping of the magnetooptical responses. This has also been confirmed

by ab initio calculation of the Ni Kerr rotation away from the Ni $M_{2,3}$ edge in the energy region of the Si $L_{2,3}$ edge. Details of the calculation can be found in chapter 6.

The experimental configuration was the longitudinal RMOKE, which was measured in a pump-probe scheme. The applied magnetic field B of 550 mT was parallel to the k-vector thus orienting the Ni magnetization along the line of intersection between the sample surface and the plane of incidence. The pump pulses of 70 fs duration and at 1.55 eV were decimated at a frequency of 25 Hz with respect to the FEL probe pulses at 50 Hz to achieve the standard pump-on/off data acquisition mode. The mean time jitter between the two pulses is 6 fs [117], as the FEL pulses are externally seeded by a portion of the same laser that is then used as a pump. The 50 fs FEL probe pulses were tuned at the energy of the Ni or the Si absorption edges. The linearly polarized FEL pulses incised with p-polarization at 45° incidence angle on the sample. The angle of incidence of the incoming IR pulses was instead set to 43.5°.

The RMOKE analysis was carried out as a function of the pump-probe delay Δt with the TONIX Wollaston-like polarimeter [18]. For each delay point 200 pulses were recorded with the polarimeter, alternating pump and unpumped pulses. Then, the difference between the mean of the pumped and the unpumped pulses θ_{pp} was calculated, contributing to the total pump-probe signal. Finally, by recording the dynamics while inverting the magnetic field, the transient magnetic dynamics was calculated as

$$\frac{\Delta M(t)}{M} = \frac{\theta_{pp}^+(t) - \theta_{pp}^-(t)}{\theta_{sat}^+ - \theta_{sat}^-}$$

where the superscripts indicate the sign of the external applied field and θ_{sat} represents the RMOKE unpumped saturation values at opposite magnetic fields. The characteristic lifetimes of the ultrafast magnetodynamics were retrieved by the demagnetization curve fitted by a decay-recovery double-exponential function

$$f(t) = \frac{\Delta M}{M}\Theta(t)(1 - e^{-t/\tau_m})e^{-t/\tau_r}$$

where Θ is the Heaviside step function, and τ_m and τ_r are the demagnetization and the recovery times, respectively.

The first two sections will show the results described in Ref. [20], that have been obtained on the sample MD with the medium doping of the substrate. The results for the other two samples will be presented in the third section.

4.3 Nickel demagnetization

The demagnetization curve at the Ni $M_{2,3}$ edge was obtained by collecting the Kerr rotation in opposite saturating magnetic fields of 550 mT. In Fig. 4.2 the demagnetization curve was studied as a function of the incoming pump fluence. The fluence has been obtained from the dimension of the spot size as $1/e^2$, as in Ref. [118] and was varied in the range 12-30 mJ/cm^2. The absorption of the optical laser on the singular layers has been calculated considering the reflectivity and the absorbance of the different layers of the sample stack at the pump laser energy of 1.55 eV [119], modeled as 2 nm of Ag deposited on 7 nm of Ni, grown on a Si$_3$N$_4$-passivated (thickness of 0.7 nm) Si substrate, in accordance to the sample characterization. The calculation has been carried out with the transfer-matrix method derived by Byrnes [37] and developed in Python. As the last layer is opaque, it is necessary to implement a cutoff, so to prevent the trivial result, i.e. that the majority of the optical laser is absorbed in the substrate. While this is indeed the case, it is noteworthy remembering that the absorbed radiation is distributed in a bigger volume, as the penetration depth in Si at 1.55 eV is $\sim 10~\mu$m. Limiting the absorption calculation up to the first 100 nm of Si, the fraction of the total optical laser fluence absorbed in the Ni layer is 95%. The remaining fluence is absorbed by the substrate (4%) and the capping layer (1%). Accordingly, it can be fairly assumed that the laser excitation is directly inducing a dynamics only in the Ni layer.
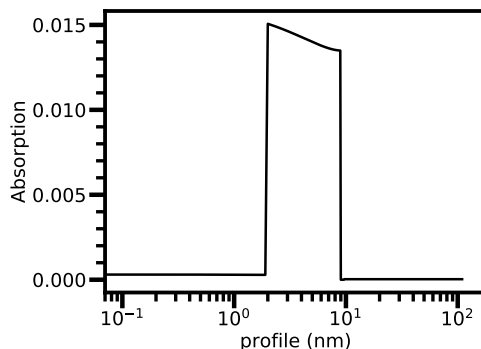

Figure 4.2: Absorption profile of the IR pulse on the Ag (2 nm)/Ni (7 nm)/Si$_3$N$_4$ (0.7 nm)/Si sample stack. The profile has been calculated using the TMM Python code described in [37]. Within the first 100 nm, the vast majority of the pump pulse is absorbed by the Ni film.

At increasing fluences the demagnetization amplitude increases accord-

ingly - linearly within the fluence range - while the dynamics shape varies only slightly. In particular, the demagnetization time is maintaining its value of 100 fs, whereas the recovery time varies in the range 15-25 ps. This variability is the result of the noise on the signal at later times. Even though the characteristic demagnetization and recovery times are slightly different, the fit obtained at the highest fluence appears highly compatible even for lower fluences. Notably, these parameters do not show a trend with the fluence, but instead seem mainly influenced by the noise. Accordingly, the dynamics presented in Fig. 4.3 have been fitted with the same parameters of the last curve, with the exception of the scaling factor. Figure 4.4 shows the demagnetization amplitude as a function of the incident laser fluence. Despite the quite high rate of demagnetization, the amplitude results linear in the interval considered. The saturation of the demagnetization appears to occur at higher fluences.
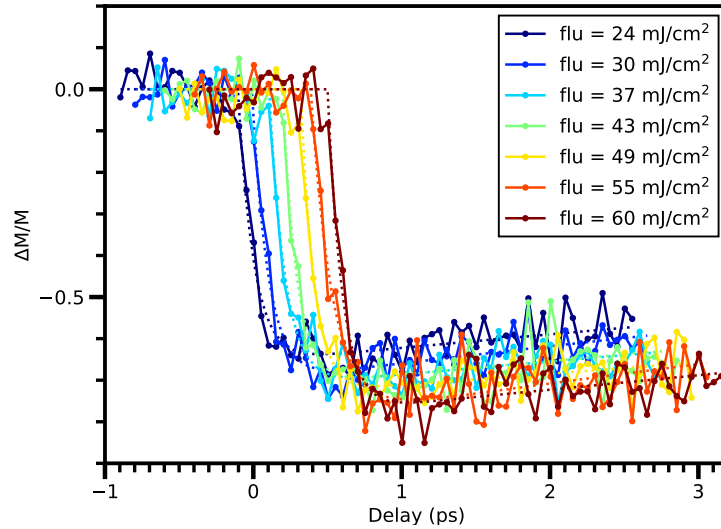

Figure 4.3:   Resonant MOKE demagnetization curves at the Ni $M_{2,3}$ edge obtained from the MD sample as a function of the pump fluence. The traces have been horizontally shifted for clarity. The shape of the demagnetization has been fitted by the double-exponential decay recovery function, revealing that the demagnetization and recovery characteristic times are highly compatible.

Figure 4.5 shows the dynamics at the highest fluence. The double-exponential decay recovery fitting function returns the value $\tau_d = 100 \pm 12$ fs as decay time, whereas the recovery time results to be $\tau_r = 20.3 \pm 5.6$

ps. Right after the arrival of the pump pulse, the magnetization is rapidly quenched. This is the result of the pump heating the electronic system and in turn reducing the exchange split of the spin-split bands at the same timescales. The demagnetization and recovery times are consistent with similar Ni films under the excitation of ultrafast femtosecond lasers [120, 108].
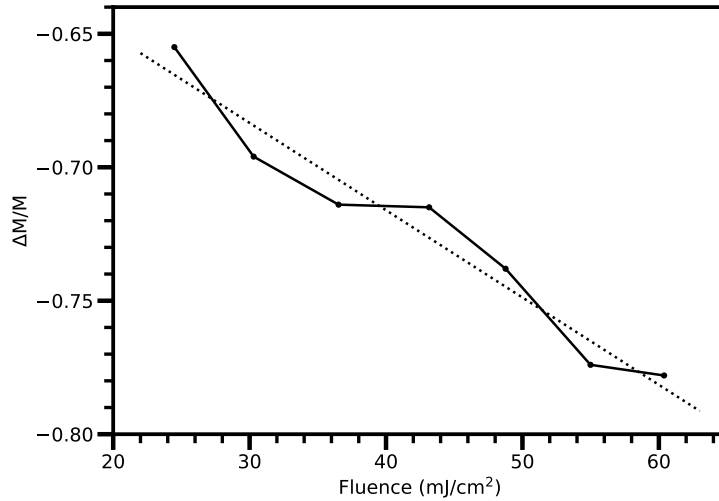

Figure 4.4: Amplitude of the resonant MOKE demagnetization curve at the Ni $M_{2,3}$ edge on the MD sample as a function of the pump fluence. In the whole range, the effect is linear, suggesting that we are away from the saturation of the demagnetization.

The Kerr rotation at the Ni $M_{2,3}$ edge has also been collected as a function of the applied magnetic field, as shown in Fig. 4.6. The Kerr rotation displays a hysteresis shape with a coercivity field of 50 mT, confirming the ferromagnetic nature of the deposited Ni film. 500 fs after the pump arrival, the Kerr hysteresis quenches while maintaining the same shape. The amplitude of the Kerr rotation, i.e. the saturation value θ_{sat}, does not allow to obtain quantitative estimations of the magnetization in the Ni film, as it is a reflection of several factors, such as the magneto-optical constant, the experimental geometry, the layer stack structure and eventually the magnetization of each layer.
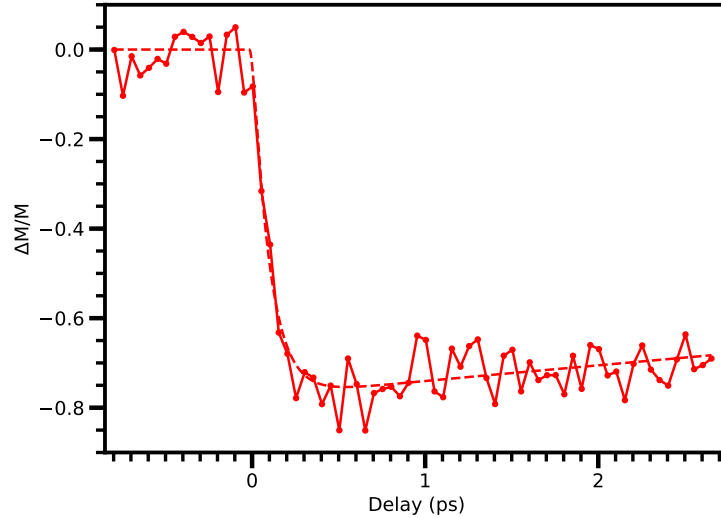
Figure 4.5: Resonant MOKE demagnetization curve at the Ni $M_{2,3}$ edge on the MD sample at the maximum fluence of 30 mJ/cm^2. The demagnetization and recovery times are respectively 100 ± 12 fs and 20.3 ± 5.6 ps. The trace has been rescaled to align the fluence at the same level as the fluence used at the Si edge exploiting the linearity of the demagnetization amplitude.

4.4   Silicon demagnetization

In the same configuration, the demagnetization curve at the Si $L_{2,3}$ edge has been collected in opposite saturating magnetic fields of 550 mT. Figure 4.7 shows the demagnetization curve for a laser pump fluence of 15 mJ/cm^2. To align this curve to the curve obtained at the Ni $M_{2,3}$ edge, a rescaling factor has been implemented for the Ni signal, exploiting the seeming invariance of the demagnetization curves in the considered fluence range. The magnetic dynamics in Si shows that a demagnetization process is in act, thus implying that a magnetic state before the pump arrival is well established. This is not trivial, as Si is expected to be weakly diamagnetic. Some possible mechanisms that would allow this kind of effect will be described in the Discussion section. Similarly to the Ni case, the quenching after the pump arrival is in the order of 50%. The observed dynamics in Si is slower than the dynamics at the Ni edge, having a demagnetization time $\tau_d = 255 \pm 86$ fs. It was not possible to obtain a reliable value on recovery time τ_r, except by providing a lower limit of 100 ps. As explained in the Discussion section, the relative difference between the two dynamics has been linked to the onset and the
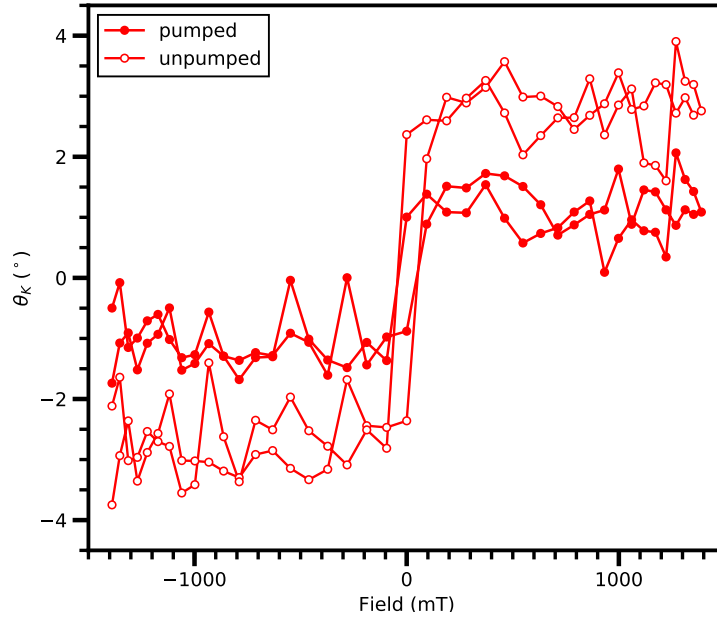
Figure 4.6: Unpumped (empty circles) and pumped (filled circles) resonant MOKE demagnetization hysteresis at the Ni $M_{2,3}$ edge on the MD sample at the maximum fluence of 30 mJ/cm^2. The pumped hysteresis has been collected 500 fs after the pump arrival. The coercivity field of 50 mT is clearly visible.

propagation of a spin current into the semiconductor.

In Fig. 4.8 the Kerr rotation at the Si $L_{2,3}$ edge has been similarly collected as a function of the magnetic field. The hysteresis shape is well defined, although it was not possible to determine the potential presence of a coercivity field due to the lower signal-to-noise ratio. 300 fs after the pump arrival, the hysteresis is quenched, but the shape remains unaltered. As previously mentioned, no comparison can be made between the saturation value θ_{sat} of Ni and Si, as the two values are affected by several aspects. Nevertheless, the behavior of Ni and Si is consistent with a reduction of the magnetization in both layers.

4.5 Doping concentration dependence

The experiment has been repeated in the same configuration on the LD and HD samples. The fluence of the optical laser was maintained at 17.5 mJ/cm^2
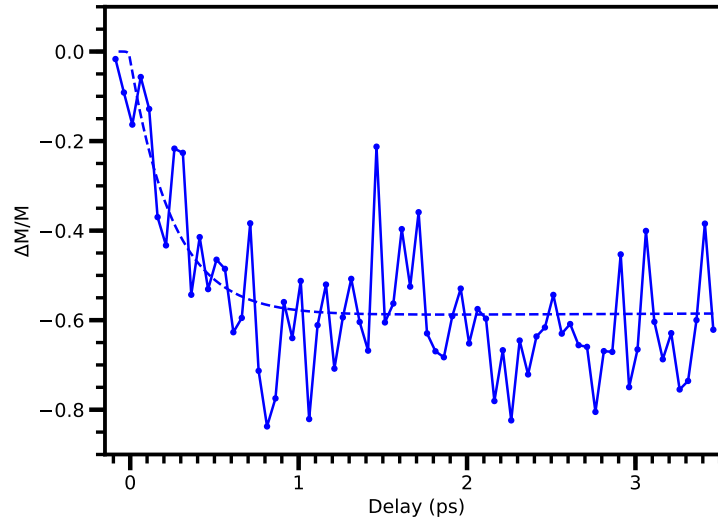
Figure 4.7: Resonant MOKE demagnetization curve at the Si $L_{2,3}$ edge on the MD sample at the fluence of 15 mJ/cm^2. The demagnetization and recovery times are respectively 255 ± 86 fs and >100 ps. The amplitude of the demagnetization reaches the same value as the Ni demagnetization trace.

for both absorption edges. At the Ni $M_{2,3}$ edge the scenario is analogous to what has been observed on the MD sample. Both samples HD and LD display a hysteresis of comparable amplitude which is quenched after the laser excitation, as shown in Fig. 4.9 (b). In particular, the sign of all the hysteresis is the same. Analogously, the demagnetization dynamics at the same edge does not reveal any particular insight, as the two dynamics overlap almost perfectly (see Fig. 4.10 (b)).

The situation is different at the Si $L_{2,3}$; first, and most notably, the sign of the hysteresis is reversed between the LD and the HD sample (Fig. 4.9 (a)). As the magnetooptical constant must be the same for the two samples, this implies that indeed the magnetization sign is reversed between the two cases. Unfortunately, it is not possible to directly compare the hysteresis sign at two different edges; the parallel or antiparallel alignment between Ni and Si can be verified instead with XMCD, as shown in chapter 5.

The magnetic dynamics in Fig. 4.10 a shows a different behavior too. In fact, HD, which is the most metallic sample, features a dynamics which comes closest to the Ni demagnetization, whereas the dynamics on LD is both retarded and slowed. In table 4.1 the results for the fitting at the Si
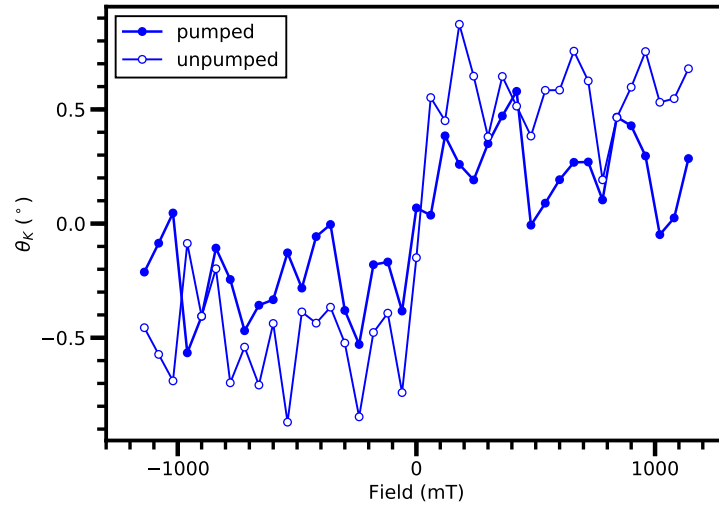
Figure 4.8: Unpumped (empty circles) and pumped (filled circles) resonant MOKE demagnetization hysteresis at the Si $L_{2,3}$ edge on the MD sample at the fluence of 15 mJ/cm^2. The pumped hysteresis has been collected 300 fs after the pump arrival. Due to the worse statistic, we are unable to observe a coercivity field.
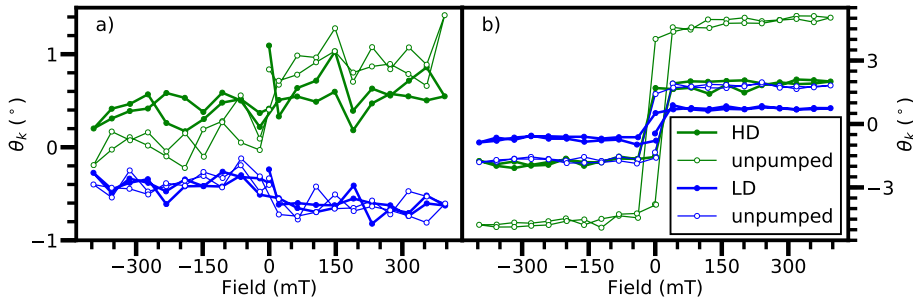

Figure 4.9: Unpumped (empty circles) and pumped (filled circles) resonant MOKE demagnetization hysteresis at the Si $L_{2,3}$ edge (panel a) and at the Ni $M_{2,3}$ edge (panel b) on the LD (blue) and HD (green) samples at the fluence of 17.5 mJ/cm^2. The two samples display the same behavior at the Ni edge, both demagnetizing after the pump arrival. The hysteresis is instead reversed at the Si edge; LD displays an amplitude of +0.4°, whereas for HD the value is -1.0°

edge - as well as at the Ni edge - are presented. It is possible to observe a trend of the demagnetization and recovery times with respect to the doping;
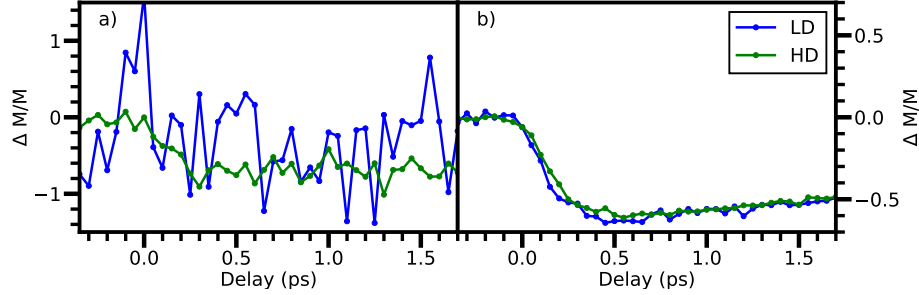
Figure 4.10: Resonant MOKE demagnetization curve at the Si $L_{2,3}$ edge (panel a) and at the Ni $M_{2,3}$ edge (panel b) on the LD (blue) and HD (green) samples at the fluence of 17.5 mJ/cm^2. The two dynamics are almost the same at the Ni edge, whereas the opposite is true at the Si edge. In particular, LD shows a maximum which is less pronounced and retarded with respect to HD, while recovering the magnetization on a shorter timescale.

the most metallic sample is in fact mimicking the Ni dynamics, whereas the least metallic shows a retarded dynamics.

sample	$Ni\ \tau_m\ (fs)$	$Ni\ \tau_r\ (ps)$	$Si\ \tau_m\ (fs)$	$Si\ \tau_r\ (ps)$
LD	179 ± 1	4.16 ± 0.02	649 ± 539	3.60 ± 1.96
MD	100 ± 12	20.3 ± 5.6	255 ± 86	> 100
HD	178 ± 1	4.80 ± 0.02	84 ± 6	51.90 ± 28.12

Table 4.1: LD, MD and HD demagnetization and recovery times measured at the Ni $M_{2,3}$ and Si $L_{2,3}$ edges by a double exponential decay-recovery fit function.

4.6   Discussion

Figure 4.11 shows the comparison between the magnetic dynamics recorded at the Ni $M_{2,3}$ and the magnetic dynamics at the Si $L_{2,3}$ edges on the MD sample. The task of interpreting the magnetic dynamics involves addressing the initial condition, which is not trivial. In fact, the initial state consists of a magnetized Ni film as well as a magnetized Si substrate, as revealed by the measured RMOKE hysteresis. Accordingly, two possible models to address the existence of a magnetized state in the otherwise weakly diamagnetic Si

have been are provided, both of which rely on the proximity effect of the Si substrate to the magnetized Ni layer.
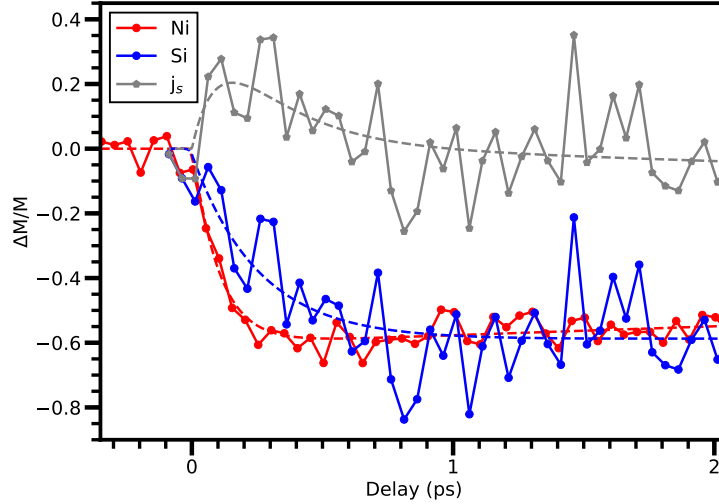

Figure 4.11: Comparison of the relative demagnetization collected at the Ni M$_{2,3}$ (red) and Si L$_{2,3}$ (blue) edges on MD. The Ni demagnetization curve was rescaled to account for the different pump fluences applied. The best fits are also shown in broken lines. The difference between the two magnetization dynamics, defined as $(\Delta M/M)_{js}$, is also shown (gray pentagons). The gray curve is a guide to the eye for$(\Delta M/M)_{j_s}$.

The first model relies on the presence of low-energy thermal electrons in Ni. As they diffuse at equilibrium in the metallic layer, spin minority and spin majority electrons experience a different exchange interaction with the mainly spin-majority-polarized electron background. Accordingly, spin minority electrons are more scattered than spin majority electrons, resulting in shorter lifetimes and velocities if compared to their spin majority counterparts. As a result, thermal electrons that impinge the Ni/Si interface are also spin-polarized, and they can diffuse as a tunneling current inside the Si substrate [121]. Only a fraction of the electrons impinging the interface are injected into the semiconductor (dashed black arrow). Because there is no net charge current without an external bias, this charge flux from Ni to Si must be balanced at equilibrium by a current flowing in the opposite direction. However, the spin polarization of the two currents can be different, resulting in a net spin accumulation in the proximal layer of Si (shaded white profile) [121].

A second possible origin of the magnetization in Si is due to the proximity magnetic field that spin-polarizes the electrons in the conduction band in the depletion layer. Due to the presence of the magnetized metal, the electrons in Si will perceive an effective magnetic field causing an exchange splitting $\Delta E_{ex} = \mu_B \cdot B_{eff}$ - where μ_B is the Bohr magneton and B_{eff} is the effective magnetic field - determining a net spin majority polarization localized in the depletion layer region. Accordingly, any change of the magnetization in Ni will affect almost instantaneously the effective field - $\Gamma/c = 55/nm/c \sim 0.2 fs$, where Γ is the attenuation length at the Si $L_{2,3}$ edge. The same applies to the spin unbalance of electrons in Si, resulting in a fast electron coupling between the Ni and Si spin-polarized electron populations.

HRTEM analysis also revealed small traces of silicide formation, in particular of $NiSi_2$, between the silicon substrate and the nitride layer. Yet, as $NiSi_2$ is predicted to be nonmagnetic in literature [122, 123], the contribution of their presence to the static magnetization of Si can be discarded. Although the two models described above qualitatively explain the magnetization of the Si substrate before the pump arrival, further investigations are needed to elucidate this point.
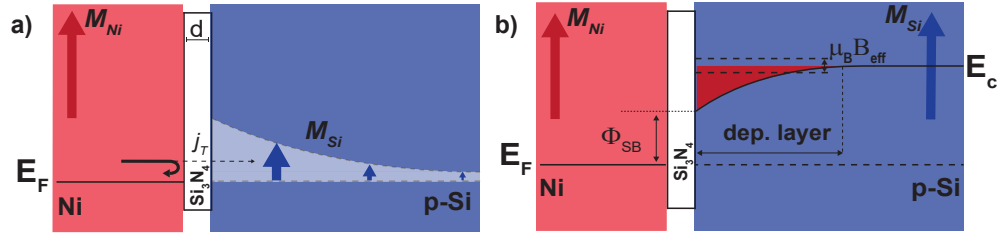

Figure 4.12: Schematic of the two proximity effect mechanisms that can account for a magnetization in the proximal layer of the Si substrate. The initial situation comprises a magnetic Ni film (red, M_{Ni}) and the magnetized Si substrate (blue M_{Si}). (a) Thermal electrons that impinge the Schottky barrier are spin-polarized; by tunneling the thin Si_3N_4 layer (d = 0.7 nm), they generate a spin-polarized current (j_T, black solid and dashed arrows). (b) Energy band diagram of the Ni/Si interface, with a focus on the depletion layer populated by spin-polarized electrons (red area).

Figure 4.12 exemplifies the two mechanisms that govern the magnetic dynamics at the heterostructure. The optical absorption of the ultrafast pump pulse by the Ni film is accompanied by a sudden increase of the

electron temperature and a consequent reduction of the spin polarization
of the exchange-split Ni bands. This process operates on the typical 100-
femtoseconds timescale, which is characteristic of ultrafast demagnetization.
Yet, because of the coupled Ni/Si system, any reduction of the spin polar-
ization in the Ni bands is reflected in a reduction of the polarization of the
electrons in Si. Accordingly, M_{Si} diminishes, as revealed by the magnetody-
namics at the Si edge. The striking feature is that within the first picosecond
from the laser excitation the responses are different when the two dynamics
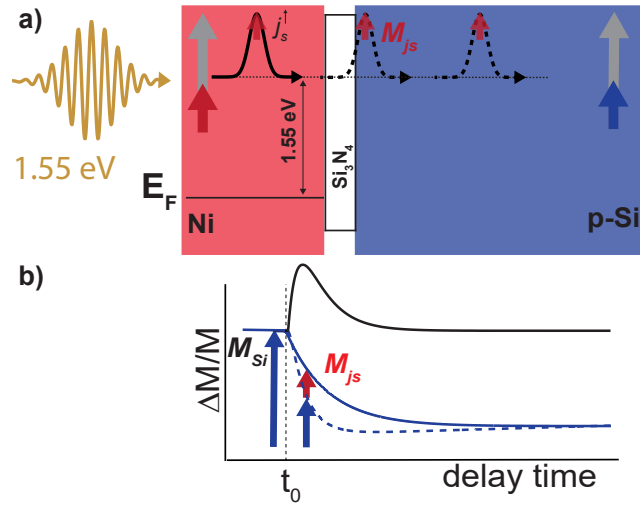are compared.

Figure 4.13: Schematic magnetic dynamics at the Ni/Si interface triggered
by the absorption of an ultrafast IR pulse (golden wave). (a) Right after the
pump arrival, the magnetization of the Ni layer is quenched. This triggers
a demagnetization of the Si and simultaneously the injection of a superdif-
fusive SC (j_s , black pulse) into Si, carrying a magnetic moment M_{j_s} (small
red arrows). (b) The two phenomena compete and slow down the demagne-
tization rate in Si (blue arrows and dashed curve).

Specifically, M_{Si} reacts 2.5 times slower than M_{Ni}; the difference
$(\Delta M/M)_{Si} - (\Delta M/M)_{Ni}$, which has been indicated as $(\Delta M/M)_{j_s}$ rep-
resents the transient spin current j_s. In the absence of any spin current
injection we expect the dynamics at the two edges to be the same as a con-
sequence of the presence of the proximity effect. As displayed in Fig. 4.13,
the propagation of j_s competes with the demagnetization of the Si substrate,
resulting in a longer demagnetization time τ_m. Consequently, based on this

scenario, the difference between the Ni $M_{2,3}$ and Si $L_{2,3}$ magnetodynamics $(\Delta M/M)_{j_s}$ can be considered as experimental evidence of the onset and propagation of a superdiffusive spin current across the Ni/Si interface.

Then, at longer times, as the spin current further propagates within the Si substrate, the observed contribution of j_s to the measured total magnetization M_{Si} decreases, as a consequence of the longer path the X-rays travel within the substrate. Finally, having established the presence of a spin current injected in the Si substrate, it is possible to obtain further quantitative information. In fact, $(\Delta M/M)_{j_s}$ displays a maximum 150 fs after the pump arrival, followed by an exponential decay. This matches the theoretical expectations in Ref.s [7, 124], that the maximum of the magnetic flux at the interface is retarded with respect to the pump pulse. The exponential decay time $\tau = 248 \pm 128 fs$ obtained from Fig. 4.11 by an exponential fitting is therefore the result of the diminished magnetic contrast of the spin current pulse feature traveling further within the semiconductor. Thus, considering the spin current pulse decay as $\tau = \Gamma/v$, the calculated velocity v of the spin pulse propagating in the Si substrate results to be $\Gamma/\tau \sim 0.2nm/fs$, which again matches the theoretical predictions based on an ideal Ni/Si system [7].
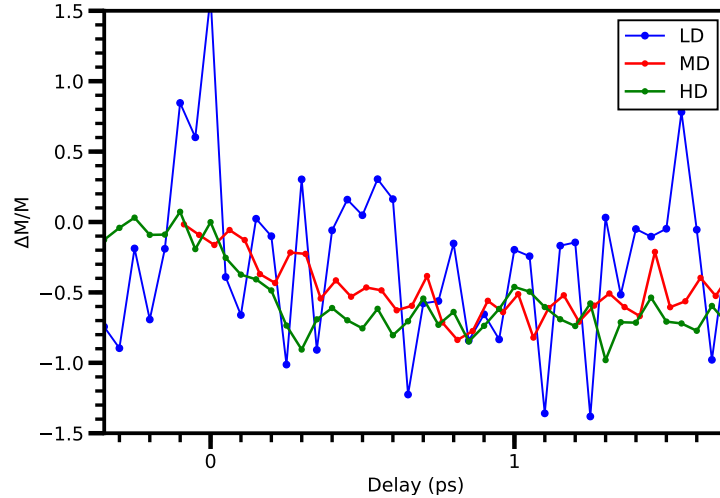

Figure 4.14: Comparison between the relative change of the Si-resolved magnetization M as a function of the time delay for the three samples LD (blue), MD (red) and HD (green). A trend with a doping concentration can be inferred, where the most metallic sample has a dynamics more similar to the dynamics of Ni.

In figure 4.14 the three dynamics at the Si $L_{2,3}$ edge at increasing doping concentrations have been displayed. The trend is particularly evident; higher doping corresponds to faster demagnetization times. It is convenient to consider as an example HD, the most metallic sample. For this case, the initial configuration consists of a Ni film of 7 nm deposited on a Si substrate with a characteristic Schottky depletion layer of about 6 nm, or less. There are two particularly interesting features; the amplitude of the demagnetization is the same at the two edges, namely 60%, and the ultrafast part of the demagnetization dynamics almost overlap. Another interesting feature is that a higher spin polarization can be expected in a lower volume at the interface as a result of the higher doping concentration. As a result, using the benchmark spin current pulse velocity of 0.2 nm/fs, the spin pulse travels entirely the depletion layer in about 20-25 fs, or less. Accordingly, the manifestation of a spin injection should be less evident. On the low-doped sample, instead, the opposite holds true. The demagnetization decay time is bigger at the Si $L_{2,3}$ edge and the recovery is faster, which makes its behavior more similar to the MD sample magnetodynamics.

XMCD characterization

5.1 Magnetic coupling at interfaces

The interest in metal-semiconductor interfaces has increased in the recent years due to the possibility to engineer their properties arising from both the metal and the semiconductor attributes. Magnetism at interfaces can be induced as well, as the electrons that are confined to the interface region can feel the influence of the magnetic films grown on it as well as the presence of an external field. The formation of a region of spin-polarized electrons has accordingly been studied in a variety of different conditions and configurations.

The most common configuration that allows a nonzero spin polarization in a nonmagnetic medium - notably a semiconductor - is by applying a bias at the interface. The main elements needed for achieving spin polarization are an efficient spin injection and a long spin lifetime in the substrate, as can be achieved in Si. The spin transport at interfaces has been addressed under the so called "conductivity mismatch" problem [8]: as the conductivity changes abruptly at the interface, the associated spin transport is greatly reduced. The problem was then theoretically [10, 9] as well as experimentally [125, 121] solved by adding a tunnel barrier between the two materials. In these cases the external electric bias is at the origin of the spin accumulation at the interface. Solving the transport equations at the interface allows to model the current density $J_\pm$ as a function of the chemical potential profile $\mu_\pm(z)$. In particular, the presence of the spin accumulation is directly related to the difference of the chemical potential as [10]

$$J_\pm = \frac{1}{e\rho_\pm}\frac{\partial \mu_\pm}{\partial z}$$

where $\rho_\pm$ is the resistivity of the two spin channels at the interface. This relation is the reason why the difference $\delta\mu = \mu_+ - \mu_-$ is called *spin accumulation*. As the steady state is determined by a form of dynamic equilibrium,

the expected spin accumulation at zero external bias is zero. Nevertheless a zero-polarized current still does not imply that the spin polarization in the semiconductor is strictly zero. In Ref. [125] the electrical injection of current between a ferromagnet into Si is shown to result in an unbalance of spin up/down electrons/holes in the Si bands. The spin accumulation orientation is determined by the magnetization direction of the magnetic film as a result of the spin-polarized tunneling. Furthermore, the accumulation varies as a function of the distance from the interface, with a characteristic spin diffusion length L_{SD}. Again, as a result of the linear scaling of the spin accumulation with the current, the expected effect at zero bias is null.

In the recent few years, net nonzero spin polarization has been reported without an external electric bias. This phenomenon especially arises in highly correlated systems, as is the case of quantum wells structure. The two-dimensional gas which arises from the confined structure allows the insurgence of exchange interaction between the free charges and the fixed magnetic moments in the ferromagnetic metal. The phenomenon is governed by the wave function overlap between exchange-split metal d-bands and the otherwise unpolarized semiconductor p- bands. This p-d exchange interaction has been studied for GaAs [126, 127], where a spin polarization without any optical or electrical spin injection has been achieved. This exchange interaction is at the origin of the strong coupling between the metal and the semiconductor, resulting in a spin-polarized electronic system. An interesting feature of these systems is the possibility to develop a proximity effect on a long-range up to 30 nm [128]. This has to be compared to the expected distance of p-d coupled systems, which is in the order of 1 nm.

A second experimental confirmation of zero-bias magnetism in nonferromagnetic samples concerns the ferromagnetic-proximity polarization (FPP). According to the findings of Ref.s [129, 130], the nuclear spins in the semiconductor align to the magnetization of the magnetic layer. Then, the resulting nuclear spin polarization generates an effective field which in turn acts on the semiconductor electron spin via the hyperfine interaction. Thus, the dynamics in the semiconductor is induced by the exchange of angular momentum between electrons and nuclei and is governed by the magnetic state of the ferromagnetic layer.

Finally, the field of diluted magnetic semiconductors is worth mentioning . Spontaneous magnetization above room temperature can arise in these systems even though the origin and control of their magnetic character is challenging both from the theoretical and experimental point of view [131]. As an example, Mn-doped semiconductors develop magnetism through the long-range interactions that are established between the Anderson-localized

states in the random-dispersed impurity medium and the free electrons in the medium.

Unfortunately, even though the previously described models allow a spin polarization in semiconductors, their underlying theories are not readily applicable to the present case, as the system is not a confined structure, does not display a nuclear magnetic moment (the most common Si isotope has zero nuclear spin), and does not contain magnetic impurities.

5.2   Description of the experimental conditions

The static magnetization in the metal/semiconductor interfaces has been studied at the CiPo beamline using X-ray magnetic circular dichroism. The XMCD signal was measured across all the Ni $M_{2,3}$ and the Si $L_{2,3}$ edges.

The sample surface was placed at $45°$ with respect to the incoming synchrotron radiation. Along the same direction, a saturation field B of 200 mT was applied orienting the magnetization of the film in the same way as the dynamical measurements in chapter 4. A AXUV100G silicon diode was placed specularly to the normal to the sample in order to collect the reflected beam . Furthermore, as the manipulator was electrically insulated, the drain current was measured as well. This scheme made it possible to acquire both the total electron yield (TEY) and the reflectivity signals simultaneously. The data were subsequently normalized to the intensity I_0 of the incident radiation, as determined by the photocurrent measured from the gold coating of the focusing toroidal mirror positioned immediately before the sample. Throughout the entire range of measurements (50-110 eV), the degree of polarization for the delivered circularly polarized synchrotron radiation is maintained at 90%, the resolving power being 8100.

Both the reflectivity and the TEY generated from the photoabsorption of the circularly polarized radiation were measured via currents by means of digital multimeters. The signal intensity at each energy point of any spectrum was the result of averaging 5 measurements at an integration time of 300 ms. Then, a baseline calculated on the pre-edge plateau was removed from each resulting trace by means of a linear fitting, and subsequently the spectra were normalized to a region above the edge. Finally, the XMCD signals were calculated as the difference between the spectra taken at opposite fields (helicities) while maintaining the helicity (field) fixed.

The measurements were carried out on both the LD and HD samples, but not on the MD one. The XMCD technique is unique inasmuch as it distinguish unambiguously the local magnetism via individual core-level ex-

citations, thus providing valuable insights into the underlying mechanisms responsible for the observed magnetic behavior. The results allowed to un-equivocally identify the local magnetism on both Ni and the proximal layer of the semiconductor substrate, potentially arising from the depletion layer region.
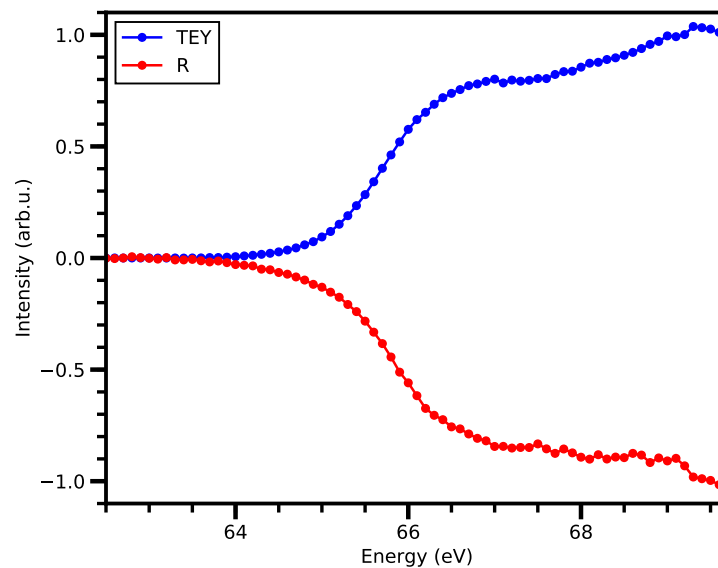
5.3   Nickel edge XMCD

Figure 5.1: Reflectivity (red) and TEY (blue) signals at the Ni $M_{2,3}$ edge. The sign of the reflectivity signal has been inverted for clarity. The two lineshapes are similar and the edge prominence is comparable in both cases.

Figure 5.1 displays the reflectivity (red) and TEY (blue) signals taken at the Ni $M_{2,3}$. At the Ni edge both reflectivity and TEY lineshapes display a clear increase culminating at approximately 66 eV, at the Ni absorption edge position. The Ni absorption edge arises from the M_2 and M_3 peaks at positions 65.3 and 66.9 eV [132, 133], which merge into a single peak. The corresponding XMCD signal acquired in TEY and reflectivity are displayed respectively in Fig.s 5.2 and 5.3. At this edge the transition responsible for generating the XMCD takes place from p-states to d-states, while the transition into s-states can be disregarded. The XMCD signal shows a sin-gle almost-symmetric peak at 66.5 eV for both the LD (squares) and HD

(triangles) samples, as the two metallic films have the same thickness and magnetic state. The complementary behavior confirms the magnetic nature of the metallic film for both samples. Reflectivity data are compared to the theoretical expectation (black curve) taken from Ref. [133].
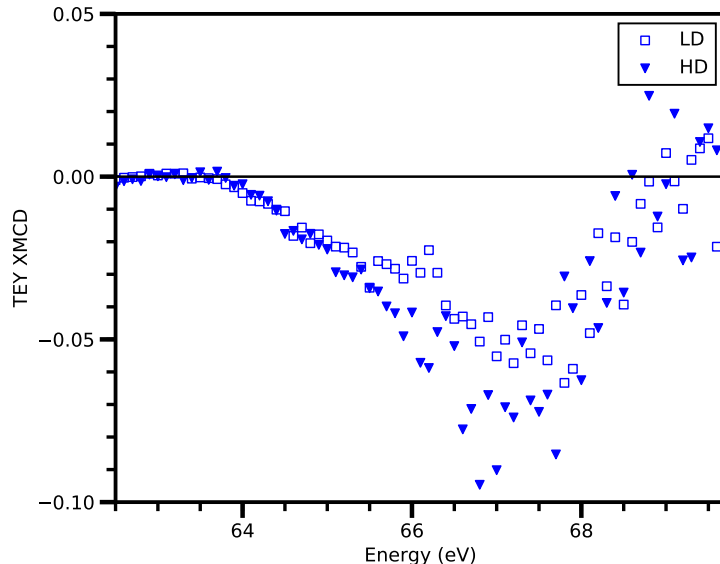

Figure 5.2: TEY XMCD signals at the Ni $M_{2,3}$ from the heterostructures. The signals on LD (squares) and HD (triangles) are complementary, confirming the magnetic nature of the metallic film for both samples.

The XMCD signals almost overlap for the two samples both in TEY and in reflectivity. It is worth mentioning that, as expected from the theoretical studies, the edge should show a first negative peak and a second positive one, as predicted in [26]. The failure to observe the second positive oscillation is related to the width of the beamline emission at fixed wiggler currents. To maximize the signal, the emission peak was set at the center of the region of investigation, sacrificing the edges. Accordingly, where the signal should be different from 0 at around 68.5 eV, the beamline emission is so little that the signal-to-noise explodes. Moreover, since the traces had to be normalized at higher energies to extract the XMCD signal, an energy range for which the emission of the beamline was sufficiently high while being as far as possible from the edge was used. As a compromise, it was necessary to choose a range comprising in part the XMCD signal; any deviation between the LD and HD traces must account for it.
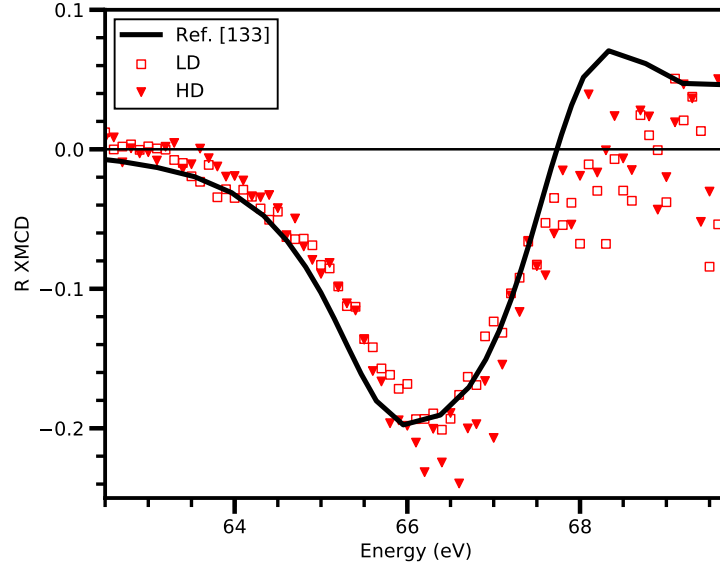
Figure 5.3: Reflectivity XMCD signals at the Ni $M_{2,3}$ from the heterostructures. Similarly to the TEY case, the signals on LD (squares) and HD (triangles) are complementary. Data are compared to the theoretical expectation (black curve) taken from Ref. [133].

5.4   Silicon edge XMCD

The Si $L_{2,3}$ absorption edge corresponds to an excitation from the 2p inner shell to a final state associated with the minimum of the conduction band [134] at a threshold of 99.8 eV. The 2p inner shell is split by a spin-orbit interaction of 0.61 eV, with a statistical intensity ratio of 2:1 between the L_2 and L_3 components. In accordance with Refs. [135, 136, 137], it is possible to make a clear determination of the origin of the peaks in the lineshape reflectivity spectra at the Si $L_{2,3}$ edge. The initial edge signal, which encompasses a pre-edge at 99 eV, a primary peak at 100 eV, and a post-edge feature at 102 eV, can be ascribed to Si^0 oxidation state. In the higher energy domain, specifically within the 104-110 eV range, a secondary peak emerges due to the presence of Si^{4+} nitridation state, which derives from the Si_3N_4 layer [138, 139]. It is noteworthy that the established Ni silicides absorption edge position resides within 0.1-0.3 eV above the Si absorption edge [140, 141].

At the Si edge TEY and reflectivity signals are different; while the reflectivity line shape shows a clear resonance signal at the Si $L_{2,3}$ threshold
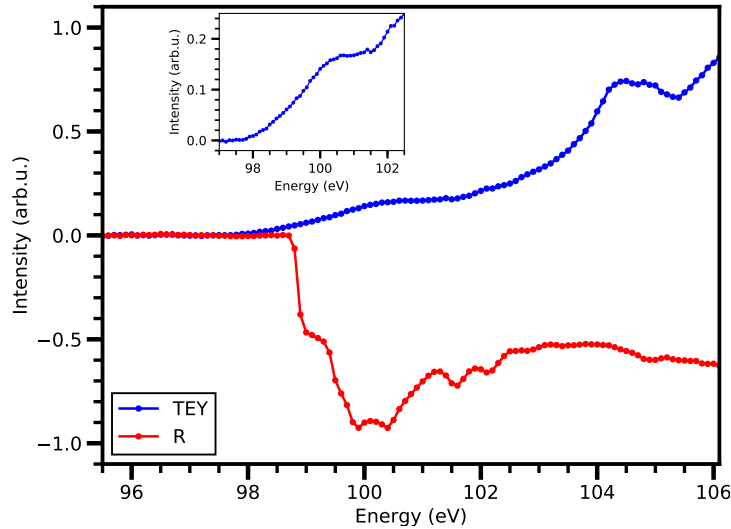
Figure 5.4: Reflectivity (red) and TEY (blue) signals at the Si $L_{2,3}$ edge. The sign of the reflectivity signal has been inverted for clarity. The edge jump is particularly evident in reflectivity, with a sudden increase at 99 eV. This is not the case with TEY, where at the same energy the edge prominence is less evident. A zoom of the TEY edge is shown in the inset.

(Fig. 5.4, red), this is not the case with TEY (blue). Consequently, the corresponding XMCD signal is much more evident in the reflectivity signal. This can be rationalised by considering that the probing depth of reflectivity is much more bulk-sensitive than that of TEY [68]. Hence, even though the magnetic signal is present in both TEY and reflectivity, the subsequent discussion and the following calculations at the Si edge are solely focused on the measurements of reflectivity. Owing to the surface-sensitivity of the TEY signal, the double-peak ascribing to the Si_3N_4 layer in the range 104-106 eV is clearly visible.

Figures 5.5 and 5.7 show the corresponding XMCD signal collected on sample LD both at opposite fields and fixed helicity (blue) and at opposite helicities and fixed field (red) at the Si edge respectively in TEY and reflectivity for the LD sample. While the reflectivity signal reveals a single peak culminating at around 100 eV that then decays to zero above 104 eV, the TEY signal seems to increase up to the maximum value remaining constant afterwards. The same behavior of the XMCD signal is assumed from the HD sample (Fig.s 5.6 and 5.8) , except for the sign reversal of the whole trace. As the sample is known to align the metallic film magnetization along the

surface and in the same direction of the external magnetic field, the substrate magnetization of LD is assumed to be "ferromagnetic-like", whereas HD behaves antiferromagnetically, meaning that the Si magnetization is opposed to the magnetization of Ni. A moving average has been superimposed to the experimental data to make the XMCD shape more apparent.

As for the MD sample, even if no XMCD data was available, it is possible to retrieve its magnetic orientation from the sign of the Kerr hysteresis. Subsequent considerations on the previous acquired data revealed that the magnetization of MD was "antiferromagnetic-like", as for the HD sample. The hysteresis in Fig. 4.8 is in fact showing the same sign as the HD hysteresis.
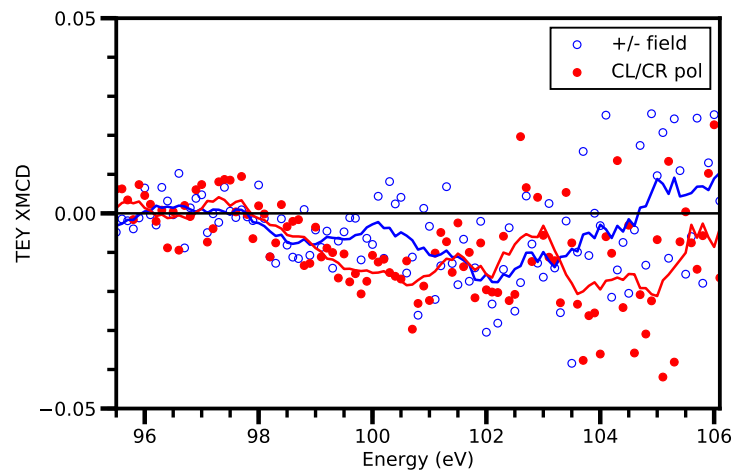

Figure 5.5: TEY XMCD signals at the Si $L_{2,3}$ from the LD heterostructure. Data collected with the same helicity at opposite fields (blue) and vice versa (red) show that the XMCD signal rises to a maximum at around 100 eV and then remains constant afterwards. A moving average has been superimposed to the data (solid red and blue lines).

5.5   Discussion

Silicon is inherently a weakly diamagnetic material, and as a consequence, an XMCD signal at any absorption Si edge is not typically expected. However, the observations reported in Fig.s 5.7 and 5.8 - as well as the static measurements in chapter 4 - reveal a distinct magnetic signal in the present Ni/Si interfaces. As reported in the previous chapter, the two potential ef-
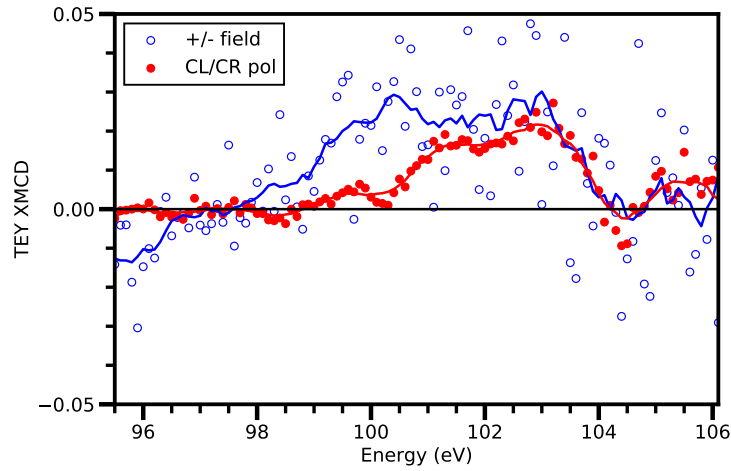
Figure 5.6: TEY XMCD signals at the Si $L_{2,3}$ from the HD heterostructure. The shape is comparable to the LD sample, except a reversal of the sign. The different signal-to-noise ratio is a result of different statistics between the two datasets.

Figure 5.7: Reflectivity XMCD signals at the Si $L_{2,3}$ from the LD heterostructure. The data collected with the same helicity at opposite fields (blue) and vice versa (red) both reveal a single peak at the Si edge position that then decays to zero after 104 eV.

fects that could account for the origin of the magnetism in silicon are both based on the proximity effect. In fact, both models rely on the effect of the
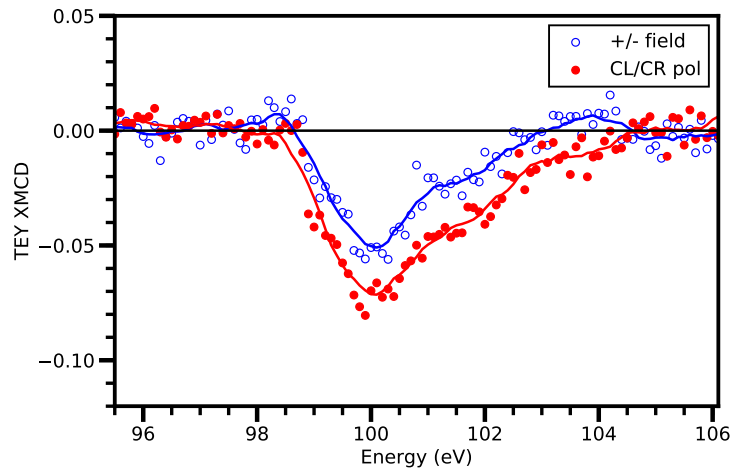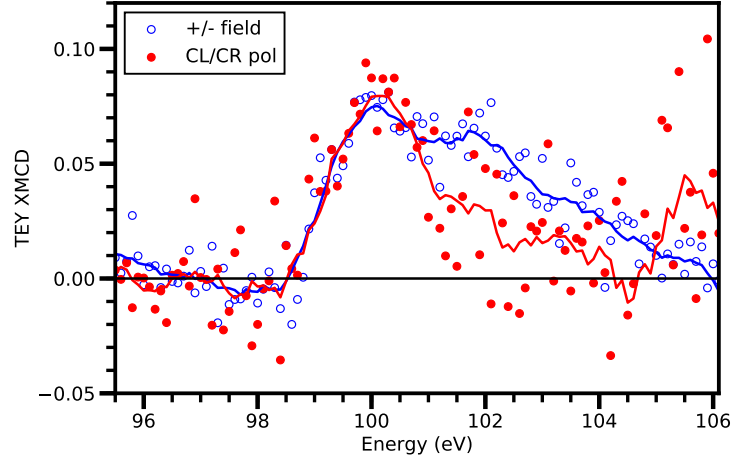
Figure 5.8:   Reflectivity XMCD signals at the Si $L_{2,3}$ from the HD het-erostructure. Similarly to the TEY data, the shape is comparable, but the overall sign is opposite.

magnetized Ni layer on the silicon substrate.

The first possible effect was identified in the spin-polarized diffusion of low-energy thermal electrons from the metal to the semiconductor. In fact, at equilibrium the electron flux to the semiconductor is spin-polarized at the interface as a result of the different exchange interactions with the predominantly spin-majority polarized electron background. The second method explores the proximal magnetic field generated by the metallic film, which induces a spin polarization for the conduction electrons in the Schottky barrier depletion layer. The perceived effective magnetic field will cause an exchange splitting ΔE_{ex} determining a net spin majority polarization. As the role of silicides can be ruled out, since the known phases of nickel silicides are nonmagnetic, the two above mentioned mechanisms should be the only possible origins of magnetism into the semiconductor.

The magnitude of the magnetization in Si can be estimated, providing greater insight into the observed effect. As stated above, the theoretical XMCD transition from a $L_{2,3}$ edge involves the core level 2p of the chemical species. In the present case, further simplifications can be applied to silicon; the transition can be considered as probing the empty s-band only, on the grounds that the contribution from the d-band to the conduction band arises solely at higher energies. Accordingly, in the range 0-3 eV above the absorption edge any contribution that does not arise from an s-band can be neglected [142]. The theoretical XMCD signal generally comprises three

terms: the orbital angular momentum $\langle L_z \rangle$, the spin angular momentum $\langle S_z \rangle$ and the magnetic dipole momentum $\langle T_z \rangle$. However, as the $L_{2,3}$ transition arises from a p- to an s-band, further simplifications may be applied. The final state allows neither a nonzero angular momentum, nor the magnetic dipole momentum [143], if any contribution arising from surfaces and interfaces is excluded. As a result, the spin sum rule from the initial filled band c to the final band l with occupation n can be written as [62, 61]

$$\frac{\int_{j^+} dE(I^+ - I^-) \; - \; \frac{c+1}{c} \int_{j^-} dE(I^+ - I^-)}{\int_{j^+ + j^-}(I^+ + I^0 + I^-)} = \frac{l(l+1) \; - \; c(c+1) \; - \; 2}{3ch}\langle S_z \rangle$$

where the labels c and l refer to the initial filled p-core level (c = 1) and the final s- h-hole filled level (l = 0) respectively, and the energy ranges j^+ and j^- pertain to the transition to a state with final moment $c + 1/2$, or L_3, and $c - 1/2$ or L_2, respectively. Accordingly, by writing the holes h as $4l + 2 - n$ (n being the number of electrons in the band), the expression can be further reduced to

$$\frac{\Delta A_3 \; - \; 2 \cdot \Delta A_2}{3A} = -\frac{2}{3}\langle S_z \rangle$$

where ΔA_3 and ΔA_2 are the XMCD asymmetries integrated on the L_3 and L_2 edges respectively and A the reflectivity edge integrated across the whole $L_{2,3}$ edge.

To apply the spin selection rule, it is necessary to unambiguously separate the two absorption edges. However, according to literature, this is not possible when the edges overlap, as occurs at the $M_{2,3}$ edge for magnetic transition metals, as well as at the Si $L_{2,3}$ edge. Despite this challenge, the XMCD signal in reflection at the Si $L_{2,3}$ edge displays a clear step where the contribution from the L_2 edge begins to increase. Based on the assumptions outlined in the previous paragraph, the L_3 and L_2 contributions to the total XMCD signal were estimated. In particular, the XMCD signal was fitted with two step-functions separated by the Si spin-orbit splitting of 0.61 eV and each aligned at higher energies with the same exponential decay, which accounts for the reduced magnetic sensitivity as we move away from the Si edge. Subsequently, the amplitudes of the two components were normalized to the mean reflectivity signal in the range up to 3 eV above the edge.

The normalized values for the L_3 and L_2 XMCD components can be found in Table 5.1. From these values it is possible to extract the spin angular momentum $\langle S_z \rangle$ for LD and HD, which are respectively $-0.0295 \pm 0.0002 \; \mu_B$

	Si L_3	*Si L_2*
LD	−0.0230	−0.0410
HD	+0.0367	+0.0357

Table 5.1:   XMCD L_2 and L_3 components of the fits for LD and HD normalized per the mean reflectivity edge A in the range 0-3 eV above the Si $L_{2,3}$ edge.

and +0.0174±0.0005 μ_B. These values are comparable to the spin magnetic moment measured at Si L-edge on Si-based Heusler alloys [144, 145].

For the Ni film, instead, the spin and angular momentum can be reasonably inferred by theoretical and experimental literature data obtained at the Ni L-edges. From a wide range of experiments on thin Ni films, the values of the measured magnetic moments were observed to deviate considerably from the bulk Ni values only for films of 2 ML or less [146]. As in the present case the thickness of the Ni film is far greater than 2 ML, it is possible to fairly estimate the magnetic moments as the bulk values moments [147], that is $\langle S_{z(Ni)} \rangle = 0.47$ μ_B and $\langle L_{z(Ni)} \rangle = 0.05$ μ_B. The case for a nanocrystalline Ni sample has been considered, as it seems a fair assumption based on the HRTEM images taken on the samples.

These findings illustrate the feasibility of observing extremely weak induced magnetic moments in heterostructures. Moreover, the estimate of the magnetic moments provides support for the above mentioned mechanisms that induce a non null magnetic moment in silicon.

Magnetooptical simulation

6.1 Overview

When an electromagnetic wave propagates through a medium that is affected by the presence of a magnetic field, magneto-optic effects occur. The most notable consequence of the optic propagation in a magnetic medium is the insurgence of two eigenmodes for each wave vector, which add together in the electric field in the medium. As is the case with the optical properties of a material, the magneto-optical effects can be fully characterized by knowing the in- and off-diagonal elements of the dielectric tensor of the material.

It is possible to model the dielectric tensor of a medium by considering its charge distribution as well as its crystal geometry, but on a more fundamental level any physically correct dielectric tensor must satisfy three conditions: (i) time-reversal symmetry, (ii) causality - through the Kramers-Kronig relations - and (iii) the sum rules. Over the years several techniques within what is known as *density functional theory* (DFT) have been deployed to overcome the complex calculations by converting the electron many-body problem in an energy functionals problem. These techniques rely on modeling the wave functions of both the valence and conduction electrons, with a combination of spatial atomic wave functions and planar wave functions. Then, the different wave functions are employed to perform a set of self-consistent calculations to generate the total electron density. The electron density is subsequently exploited to determine the total potential that is thus used in the next iteration to adjust the electron density until convergence is reached. The most common computational strategy is called local density approximation: it consists of reducing the many-body interactions to a single electron interacting with the mean electron density generated by the other electrons. DFT allows to obtain the material behavior from first principles relying entirely on quantum mechanical considerations without the knowledge of any fundamental material property.

To simulate the magnetic properties of the Ni/Si interfaces both at the Ni
and at the Si absorption edges, the dielectric tensor of magnetic Ni has been
calculated. To perform the DFT calculations, the *WIEN2k* code [148] has
been employed. This code treats both valence and conduction electrons us-
ing planar waves as a basis set and exploits the full potential and charge
density to solve the Kohn-Sham problem, making it one of the most pre-
cise implementations of DFT. With the advent of precise resonant magnetic
techniques, magnetic measurements at the absorption edges have been used
to test the validity of the mathematical models employed to describe mag-
netic solids. As a result, a thriving scientific literature exists on this matter
[54, 133]. This allowed also to match the in- and out-of-diagonal dielectric
tensor components to the experimental data.

6.2   Nickel dielectric tensor
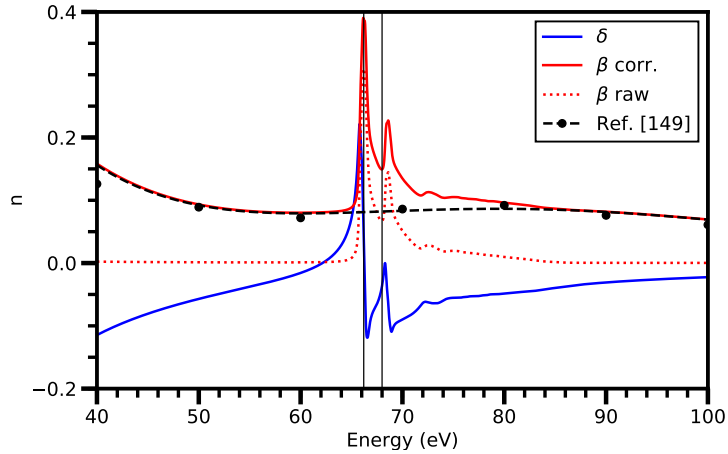
Figure 6.1: Real (blue) and imaginary (red, dotted line) components (as 1
- δ - iβ) of the refractive index at the Ni $M_{2,3}$ edge obtained as the square
root of ϵ_{xx}. The imaginary component is greatly underestimated, as can be
seen from the data obtained from Ref. [149] (black dots). The polynomial
fit (black, dashed line) based on the data from Ref. [149] allows to correct
the behavior of the imaginary part away from the resonance. The corrected
component has also been plotted (red, solid line). The data suffered from
a rigid energy shift that was corrected by matching the absorption edge to
the experimental values (black vertical lines).

The *WIEN2k* code has been used to calculate the components of the

dielectric tensor. In the case of nickel, being a ferromagnet with cubic structure, there are only two independent components of the dielectric tensor, i.e. the in-diagonal term ϵ_{xx} and the out-of-diagonal term ϵ_{xy}. The usual procedure is to calculate the real components of the dielectric tensor and then obtain the imaginary component by applying the *Kramers-Kronig* (KK) transformations. The KK integrals exhibit a slow rate of convergence, necessitating an energy cut-off at high energy to ensure the reliability of resultant values [150]. As an unintended outcome, upon juxtaposition of the calculated data with preexisting literature [149, 133], some incongruities have emerged. To amend the anomalous imaginary components, their convergence towards zero at higher energies has been methodically calibrated.
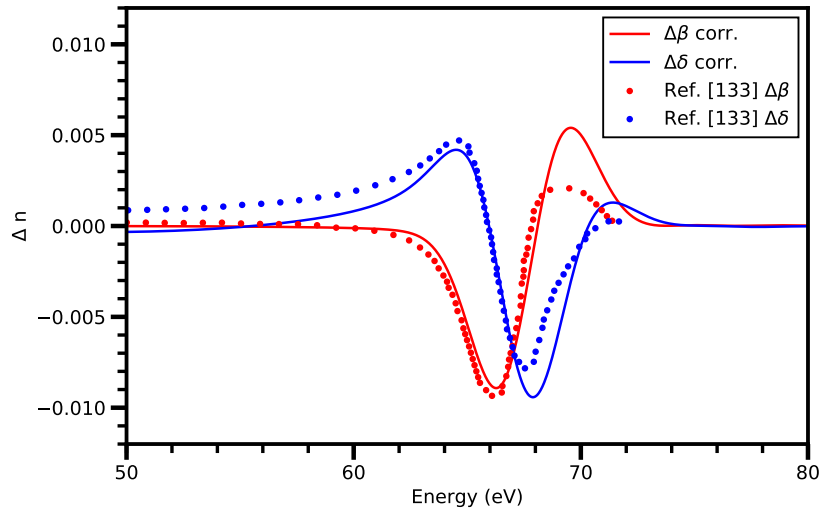
Figure 6.2: Real (blue) and imaginary (red, solid line) components of the magneto-optical functions at the Ni $M_{2,3}$ edge obtained by the in- and out-of-diagonal components of the dielectric tensor. Data from Ref. [133] have been overlapped to the real (blue) and imaginary (red dots) components. To match the data, a Gaussian smoothing of 1.4 eV was applied to the calculated components and a rescaling factor of 0.6 was implemented.

In particular, from Henke [149] the value of the imaginary component of the refractive index $n_{xx} = \sqrt{\epsilon_{xx}}$ was extracted and compared to the value calculated from the *WIEN2k* code. Notably, the calculation greatly underestimated the contribution. Accordingly, the data from Henke has been interpolated and this contribution was added to the imaginary part of the calculated refractive index. The results of the correction are presented

in Fig. 6.1, from which the correct in-diagonal term of the dielectric tensor has been obtained.

The out-of-diagonal component has been referred to Ref. [133]. In fact, in the article the measured magneto-optical function is written as

$$\Delta\delta(\omega) - i\Delta\beta(\omega) = 0.5\, i\, \epsilon_{xy}(\omega)/\sqrt{\epsilon_{xx}(\omega)}$$

Similarly, the real and imaginary parts of the out-of-diagonal dielectric tensor was considered and the imaginary component was corrected so that it converged at higher energies. The results of the corrected real and imaginary magneto-optical functions are presented in Fig. 6.2 and are compared with the data from Ref. [133]. The overall agreement of both the real and imaginary components to the data presented is quite good.

6.3   XMCD and MOKE calculations

To test the validity of the measured static properties of the interface, the XMCD and MOKE response of the system has been modeled at the Ni $M_{2,3}$ and Si $L_{2,3}$ absorption edges. We have employed the so-called *magnetic matrix formalism* which is the magnetic counterpart of the transfer-matrix method [151] employed in the x-ray reflectometry studies. In particular, as magnetism interacts also with the polarization of the beam traveling in the medium, it is necessary to know how the polarization changes as a function of the profile.

X-ray reflectometry is usually employed to find the intensity in the case of thin films, when the incoming beam wavelength is comparable with the thickness d of the films. In this specific case the beam interferes multiple times with itself within the film contributing either constructively or destructively, depending on the exact geometry. The condition of constructive reflectivity is given when the path of the beam within the film matches an integer number m of wavelengths λ, or

$$\Delta s = 2d\,\sqrt{n_1^2 - cos(\theta)^2} = m\lambda \sim 2d\,sin(\theta)$$

where the last equivalence is justified in the X-ray regime, given that the index of refraction n_1 approaches the unity. Similarly, considering the transfer of momentum in the same case, the difference between the two incoming and outgoing momentum vectors $\boldsymbol{k'} - \boldsymbol{k_0} = \boldsymbol{q_z}$ is directed along the z axis, z being the normal of the surface, so that according the first law of reflection

$$2d \, \frac{q_z/2}{k_0} = m\lambda$$

which is the Laue condition of diffraction for a momentum transfer which is equal to $2\pi/d$ in modulus. Nonetheless, the intensity of the interference is also contingent on the amplitude of the beam; generally, this augments as the angles decrease, or when there is a more pronounced change in the refractive index at the interface. It also depends on the polarization of the beam due to the continuity equations for the total electric and magnetic fields at the interfaces for the three beams (E_i, E_r and E_t and their magnetic counterparts). In fact, the in-plane electric field $\boldsymbol{E}_{//}$ and the out-of-plane magnetic field $\boldsymbol{B}_\perp$ must be continuous. If the ratio between the reflected/refracted electric fields and the incoming field ($E_r/E_i = r$, $E_t/E_i = t$) is written for the two different polarizations, the classic Fresnel equations can be obtained.

6.3.1 Transfer matrix method

Owing to both energy conservation and the reversibility of the optical path, if two media are considered, denoted as 1 and 2, the relations $r_{12} = -r_{21}$ - which is represented as r - and $t_{12} = r + 1$ hold. Given that the refractive index in the X-ray region approaches unity, it is typically expressed as $n = 1 - \delta + i\beta$. When considering reflectivity in practical applications, it is imperative to appropriately handle the presence of multiple refracted/reflected beams within thin film structures. Furthermore, as the absorption is strong at absorption edges, the reflectivity can change quite abruptly in the X-ray regime as the wavelength approaches the attenuation length and the characteristic lengths of the sample, causing for example the interference patterns to disappear. To account for the interference pattern of the multiple beams originating at interfaces, all the contributions have to be taken into account and summed up together. Accordingly, at each interface two incoming (towards positive z) and two outgoing (negative z) waves have to be considered; their electric field will add up to form the total field per layer. Including the reflected and transmitted beam, the coupled iterative formulas

$$\begin{cases} E_i^R e^{ik_i z} = rE_i^T e^{-ik_i z} + (1-r)E_{i+1}^R e^{ik_{i+1}z} \\ E_{i+1}^T e^{-ik_{i+1}z} = -rE_{i+1}^R e^{ik_{i+1}z} + (1+r)E_i^T e^{-ik_i z} \end{cases}$$

can be obtained, where the superscripts indicate a propagating wave (T) and a back-propagating (R) wave which have a negative and positive phase

term respectively, whereas the subscripts denote the layer. The geometry is schematically represented in Fig. 6.3. The two equations can be thought as representing the conditions for matching of the electric field amplitudes for the reflection from the medium i to the medium i+1 and for the opposite case from i+1 to i (in the latter T can be substituted T with R). If E_i^R is substituted with $R_i\,E_i^T$, where R_i represents the ratio of the two fields, the following recursive expression can be found

$$R_i = \frac{r_i + R_{i+1}e^{2k_{i+1}\Delta z}}{1 + r_i\,R_{i+1}e^{2k_{i+1}\Delta z}}$$

where Δz is the thickness of the i-th layer. Notably, R_i and r_i represent respectively the reflectivity in one layer and the reflectivity at one interface. As it is an iterative formula, the bottom layer which corresponds to a semi-infinite medium has to be considered. As a consequence, there is no light is coming back and r and R are equal. The total reflectivity is then calculated as $|R_0|^2 = I_r/I_0$. This recursive method, which is also called *transfer matrix method* (TMM) [151], is implemented in several programming codes. The Python package *tmm* has been used to calculate the reflectivity of the Ni/Si heterostructure [37].
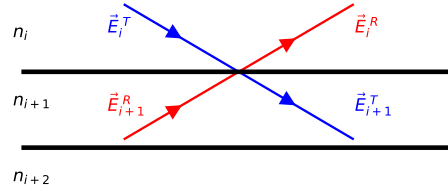
Figure 6.3:   The schematic view of the transfer-matrix method problem. In each layer a propagating beam (T) and a back-propagating beam (R) superimpose to form the total electric field for each layer.

6.3.2   Magnetic scattering

When dealing with magnetic structures, it is known that an incoming beam changes both its intensity and its polarization as it interacts with the magnetic medium. It is therefore it is not sufficient to know the reflectivity with the TMM model, that only describes the case of interference of multiple waves with no change of polarization upon interaction. Considering a magnetic atom, an incoming planar wave is scattered as a spherical wave with the form [152]

$$E_f = -r_e f(q, \omega_0, \boldsymbol{e_f}, \boldsymbol{e_i}) \frac{e^{ik_0 r}}{r} E_i$$

where the scattering factor f includes both the nonmagnetic term $\boldsymbol{e_f^*} \cdot \boldsymbol{e_i}$ $[f_0 + f'(\omega) + if''(\omega)]$, which conserves the polarization, and the magnetic term, which can be written as a vector product $i \boldsymbol{e_f^*} \times \boldsymbol{e_i} \cdot \boldsymbol{b} \, [m'(\omega) + im''(\omega)]$. The vector $\boldsymbol{b}$ can be expressed in spherical coordinates and represents the magnetization direction. The scattering factor can be summarized in a single product as $\boldsymbol{e_f^*} \cdot \boldsymbol{F} \cdot \boldsymbol{e_i}$ and is linked to the susceptivity tensor χ through the optical theorem as

$$\chi = \frac{4\pi}{k_0^2} r_e \sum_i \rho_i F_i = \epsilon - 1 \sim -2\delta + 2i\beta$$

where the sum is carried over the different chemical species and the last equivalence is valid only in the X-ray regime. In calculating the scattering the two possible polarizations of the light σ and π can be represented as

$$\boldsymbol{e_\sigma} = \begin{pmatrix} 1 \\ 0 \\ 0 \end{pmatrix} \qquad \boldsymbol{e_\pi} = \begin{pmatrix} 0 \\ sin(\theta) \\ cos(\theta) \end{pmatrix}$$

whereas the circular polarization is represented as a combination of the two $\boldsymbol{e_{l/r}} = 1/\sqrt{2}(\boldsymbol{e_\sigma} \pm i\boldsymbol{e_\pi})$. Finally, by considering the scattering factor for a left and right circularly polarized wave, it is possible to show that the real and imaginary part take the form

$$\beta = \beta_0 \mp \beta_M[sin(\theta)cos(\phi_M) - cos(\theta)sin(\phi_M)sin(\gamma_M)]$$

and

$$\delta = \delta_0 \pm \delta_M[sin(\theta)cos(\phi_M) - cos(\theta)sin(\phi_M)sin(\gamma_M)]$$

which is a function of the direction of the beam θ with respect to the magnetization vector in spherical coordinates (ϕ_M, γ_M). This can be considered as a general expression of XMCD retrieved entirely from the scattering function, as $\Delta\mu \propto \beta_M$.

6.3.3 Matrix formalism of magnetic optical transport

The reflection and refraction effects within a magnetic heterostructure can be effectively delineated through a 4x4 [153, 41] matrix formalism. Indeed, in a nonmagnetic medium, the reflected and refracted beams are singular for
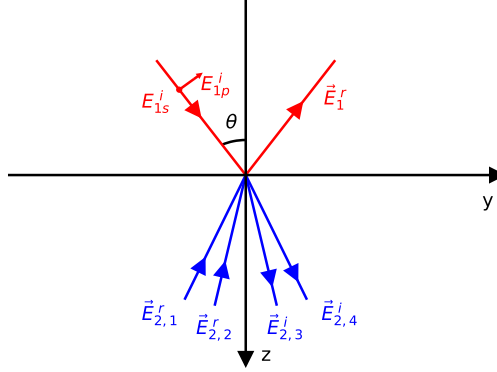
Figure 6.4: An incident beam (E^i) is reflected (E^r) and refracted on a magnetic surface. Due to the magnetization, the solutions of E^i and E^r in the material are split in two modes, which represent the two circularly polarized eigenmodes.

each polarization. However, within a magnetic environment, the presence of two eigenmodes essentially doubles the dimensionality of the problem, a concept that is schematically elucidated in Fig. 6.4. In chapter 2 the Fresnel equation in a magnetic medium has been derived as

$$\nabla^2 \boldsymbol{E} - \boldsymbol{\nabla}(\boldsymbol{\nabla} \cdot \boldsymbol{E}) = -k_0^2 \, \epsilon \, \boldsymbol{E}$$

Now the attention will be drawn to a specific geometry: the sample demonstrates homogeneity in the x-y plane, while its properties are solely dependent on the z-direction, which is orthogonal to the surface. The transferred momentum, denoted as q_z, equates to $2\pi/\lambda$. The dependence on the profile is then given only through $\epsilon(z)$. The problem can be solved inserting an electric field in the form of a plane wave $\boldsymbol{E} = \boldsymbol{E_0} \, e^{\boldsymbol{k} \cdot \boldsymbol{r}}$ as a solution. If the plane y-z is the scattering plane, then the moment is $\boldsymbol{k} = k_0(0, k_y, k_z)$, where $k_y = cos(\theta)$ is a material-independent property related to the incident angle θ.
Solving the system is equivalent to solving the problem

$$\begin{pmatrix} k_y^2 + k_z^2 - \epsilon_{xx} & -\epsilon_{xy} & -\epsilon_{xz} \\ -\epsilon_{yx} & k_z^2 - \epsilon_{yy} & k_y k_z - \epsilon_{yz} \\ -\epsilon_{zx} & k_y k_z - \epsilon_{zy} & k_y^2 - \epsilon_{zz} \end{pmatrix} \boldsymbol{E_0} = 0$$

If the y component is written as $k_y = cos(\theta)$, the determinant has a form of a polynomial of fourth grade in k_z. The four solutions represent therefore

the four wave vectors that are eigenmodes of the magnetic medium. The simplest case is a nonmagnetic medium, in which $\epsilon = n^2$ is diagonal. Solving the determinant

$$(cos^2(\theta) + k_z^2 - n^2)((k_z^2 - n^2)(cos^2(\theta) - n^2) - cos^2(\theta)k_z^2) = 0$$

the four solutions are found to be double degenerate, being $k_{z\,1,2} = -\sqrt{n^2 - cos^2(\theta)}$ and $k_{z\,3,4} = +\sqrt{n^2 - cos^2(\theta)}$ for positive and negative propagation, which corresponds to the Snell law. In particular they are solutions for the two polarizations, as $\boldsymbol{e_{13}} = (1, 0, 0)$ and $\boldsymbol{e_{24}} = (0, k_{24}, cos(\theta))$. Having the expression of the four electric fields, any solution of the electric field will be a linear combination of the four components as

$$\boldsymbol{E^{(j)}}(z) = \sum_{i=1}^{4} E_i^{(j)} \boldsymbol{e_i^{(j)}} e^{ik_{z_i}z}$$

whereas the magnetic field $i\omega \boldsymbol{B} = \boldsymbol{\nabla} \times \boldsymbol{E}$, so that

$$\boldsymbol{B^{(j)}}(z) = \sum_{i=1}^{4} \frac{\boldsymbol{k}}{\omega} \times E_i^{(j)} \boldsymbol{e_i^{(j)}} e^{ik_{z_i}z}$$

where $\boldsymbol{b_i} = \omega \boldsymbol{k} \times \boldsymbol{e_i}$. Therefore, the problem has been reduced to finding the four amplitudes $E_i^{(j)}$ for each layer j. Finally, it is possible to connect the solutions between adjacent layers by considering the boundary conditions, for example the in-plane components of the magnetic and electric fields, $E_{x/y}^{(j)b} = E_{x/y}^{(j)t}$ and $B_{x/y}^{(j)b} = B_{x/y}^{(j)t}$, where b and t denote the bottom and top layers. As a result, now the system has been described with 4N unknowns for N different layers, which are the propagating (positive $\mathbb{R}e(k_z)$) and back-propagating (negative $\mathbb{R}e(k_z)$) solutions. The 4x4 formalism allows to write the four solutions of the top layer as a function of the four solutions of the bottom layer

$$\begin{pmatrix} E_x^{(j)t} \\ E_y^{(j)t} \\ B_x^{(j)t} \\ B_y^{(j)t} \end{pmatrix} = \begin{pmatrix} E_x^{(j)b} \\ E_y^{(j)b} \\ B_x^{(j)b} \\ B_y^{(j)b} \end{pmatrix} P^{(j)} = A^{(j)} P^{(j)} \begin{pmatrix} E_1^{(j)} \\ E_2^{(j)} \\ E_3^{(j)} \\ E_4^{(j)} \end{pmatrix}$$

where the $P^{(j)}$ matrix is the propagating matrix that connects the four modes between the top and bottom surfaces within the film

$$P^{(j)} = \begin{pmatrix} e^{ik_{z1}d^{(j)}} & 0 & 0 & 0 \\ 0 & e^{ik_{z2}d^{(j)}} & 0 & 0 \\ 0 & 0 & e^{ik_{z3}d^{(j)}} & 0 \\ 0 & 0 & 0 & e^{ik_{z4}d^{(j)}} \end{pmatrix}$$

where $d^{(j)}$ is the thickness of the layer j, whereas the $A^{(j)}$ matrix is the matrix of the eigenvectors

$$A^{(j)} = \begin{pmatrix} e_{x1} & e_{x2} & e_{x3} & e_{x4} \\ e_{y1} & e_{y2} & e_{y3} & e_{y4} \\ b_{x1} & b_{x2} & b_{x3} & b_{x4} \\ b_{y1} & b_{y2} & b_{y3} & b_{y4} \end{pmatrix}$$

With the four-vector $E^{(j)}$, the interface conditions of the layer j can be applied to get the conditions from the layer $j-1$ as

$$A^{(j)}E^{(j)} = A^{(j-1)}P^{(j-1)}E^{(j-1)}$$

For a stack of different layers, the four-vector for the vacuum can be connected to the four-vector of the substrate as

$$E^{(v)} = \Big[\prod_j A^{-1(j)}A^{(j)}P^{(j)}\Big]E^{(s)} = BE^{(s)}$$

Therefore, the stack can be fully described by the eight coefficients of the "incident" quadrivector and the "outgoing" quadrivector. However, for the components in the bulk there is no reflected wave in the substrate. By definition the top layer is vacuum, so that $A^0 = A_0$ is the isotropic term. So, $e_1^{(v)}$ and $e_2^{(v)}$ represent the σ and π incident components and $e_3^{(s)} = e_4^{(s)} = 0$. The reflectivity will thus be

$$\begin{pmatrix} e_3^{(v)} \\ e_4^{(v)} \end{pmatrix} = \begin{pmatrix} r_{11} & r_{12} \\ r_{21} & r_{22} \end{pmatrix} \begin{pmatrix} e_1^{(v)} \\ e_2^{(v)} \end{pmatrix}$$

where the matrix r_{ij} is defined as

$$\frac{1}{B_{22}B_{11} - B_{12}B_{21}} \begin{pmatrix} B_{31} & B_{41} \\ B_{32} & B_{42} \end{pmatrix} \begin{pmatrix} B_{22} & -B_{12} \\ -B_{21} & B_{11} \end{pmatrix}$$

The total reflectivity is finally defined as the ratio between the outgoing terms and the incoming terms

$$R = \frac{Ir}{I_0} = \frac{|e_3^{(v)}|^2 + |e_4^{(v)}|^2}{|e_1^{(v)}|^2 + |e_2^{(v)}|^2}$$

6.3.4 Zak formalism

The medium boundary and the medium propagation matrix have been used in the form indicated by [154, 40], which is simply a transformation of the four-vector by taking into account the electric and magnetic components in the plane of incidence instead of the components tangential to the surface. The $A^{(j)}$ and $P^{(j)}$ matrices can therefore be written as

$$A^{(j)} = \begin{pmatrix} 1 & 0 & 1 & 0 \\ \frac{i\alpha_y Q}{\alpha_z}(\alpha_y g_i - 2s_\phi s_\gamma) & \alpha_z + i\alpha_y s_\phi c_\gamma & -\frac{i\alpha_y Q}{\alpha_z}(\alpha_y g_i - 2s_\phi s_\gamma) & -\alpha_z + i\alpha_y s_\phi c_\gamma \\ \frac{iNg_iQ}{2} & -N & \frac{iNg_rQ}{2} & -N \\ N\alpha_z & \frac{iNg_iQ}{\alpha_z} & -N\alpha_z & -\frac{iNg_iQ}{\alpha_z} \end{pmatrix}$$

and

$$P^{(j)} = \begin{pmatrix} U & Ug_i & 0 & 0 \\ -Ug_i & U & 0 & 0 \\ 0 & 0 & U^{-1} & U^{-1}g_r \\ 0 & 0 & U^{-1}g_r & U^{-1} \end{pmatrix}$$

where $\alpha_y = sin(\theta)/N$ and $\alpha_z = \sqrt{1 - \alpha_y^2}$ define the optical paths in the material as per the Snell law, $s_\phi = sin(\phi)$, $s_\gamma = sin(\gamma)$ and $c_\gamma = cos(\gamma)$ denote the magnetization direction in spherical coordinates, and $g_{i/r} = \pm cos(\phi)\alpha_z + sin(\phi)sin(\gamma)\alpha_z$.

These formulas have been used to calculate the contribution for the MOKE and XMCD signal at each layer at the Ni edge. The rotation of the polarization is given by the real part of the ratios

$$\theta_\sigma = \mathbb{R}e(r_{\pi\sigma}/r_{\sigma\sigma}) \qquad \theta_\pi = -\mathbb{R}e(r_{\sigma\pi}/r_{\pi\pi})$$

whereas the following modulus has to be considered to calculate the XMCD signal [155, 156]

$$R_\pm = \left| \begin{pmatrix} r_{\sigma\sigma} & \delta_{\sigma\pi} \\ -\delta_{\sigma\pi} & r_{\pi\pi} \end{pmatrix} \frac{1}{\sqrt{2}} \begin{pmatrix} 1 \\ \pm i \end{pmatrix} \right| = (R_{\sigma\sigma} + R_{\pi\pi} + 2\Delta_{\sigma\pi}) \pm \mathbb{I}m(-\delta_{\sigma\pi}^*(r_{\sigma\sigma} + r_{\pi\pi}))$$
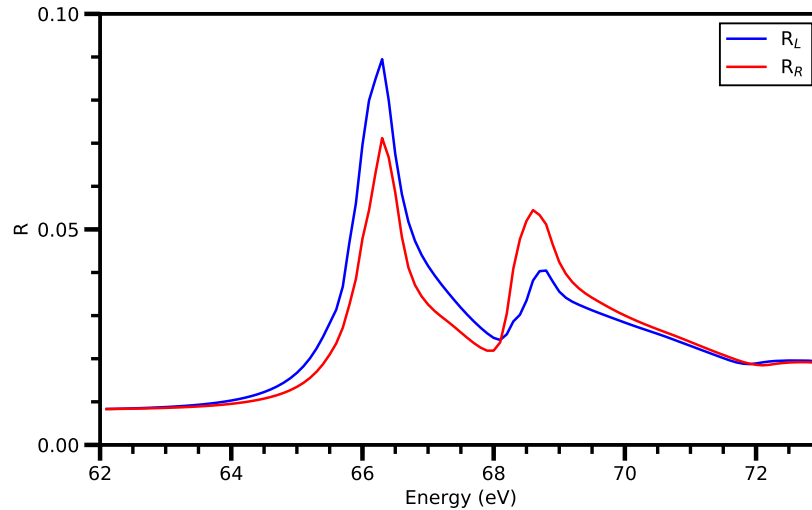
6.4   XMCD ad MOKE Nickel edge

Figure 6.5:   Reflectivity of a stack of 7 nm of Ni on a Si substrate in the longitudinal configuration for an angle of incidence of $45°$ at the Ni $M_{2,3}$ edge. The double-peak structure shows the familiar shape, with the L_3 and L_2 edges reflectivities having an opposite trend.

The reflectivity at $45°$ incidence angle for left and right polarization in the longitudinal configuration has been calculated using the modeled Ni dielectric tensor. Henceforth, to simplify calculations, the sample stack has been reduced to Ni(7nm)/Si. The positive and negative reflectivity traces are shown in Fig. 6.5. However, the conditions under which the XMCD was measured were not optimal, leading to strong deviations from the expected signal. In fact, as the wiggler current could not be changed while selecting the energy with the monochromator, during the energy scan, the beamline emission was strongly peaked at the center of the energy scan and lower at the edges, which made the measurements inaccurate. As the beamline peak emission was centered roughly at 66 eV, even though the XMCD signal was still expected to be nonzero at 69 eV, it turned out to be necessary to use this region to normalize the traces. Accordingly, the measured XMCD signal shows a single peak. In Fig. 6.6 (a) the data on the LD sample have been overlapped to the theoretical curves for the actual sample (7 nm of Ni on a Si substrate) and for a bulk Ni sample. It is particularly noticeable that both at lower and higher energies the discrepancy is huge. However, in Fig. 6.6 (a) the XMCD signal has been calculated by simply subtracting
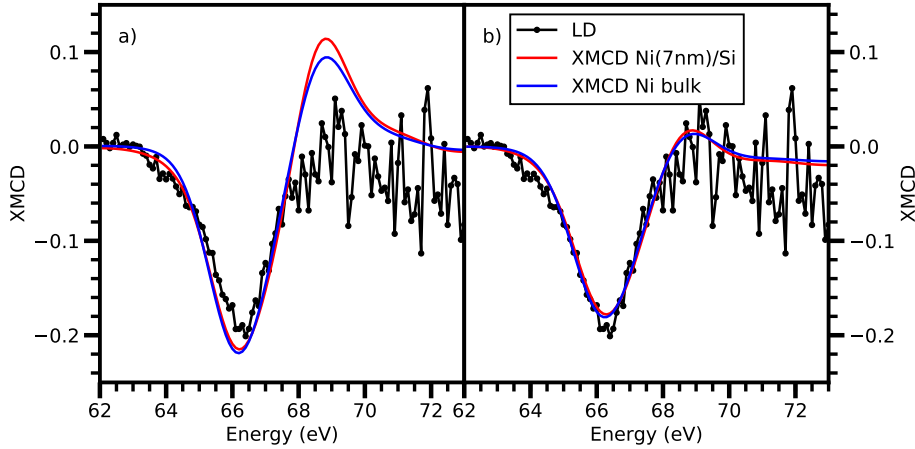
Figure 6.6: XMCD signal on LD (black) compared to the theoretical XMCD signal for the Ni (7nm)/Si stack (red) and for Ni bulk (blue). In panel a) the theoretical XMCD has been calculated simply as the difference between left and right-polarized reflectivity, whereas in panel b) at each theoretical reflectivity a linear baseline calculated below 63 eV was subtracted and then the resulting trace was normalized to 1 above 68 eV. The thin film and the bulk material show almost the same XMCD, as can be expected from Ref. [146]. At the theoretical traces a Gaussian broadening of 0.7 eV was applied as well as a rescaling factor of 0.5.

R_l and R_r, as the two reflectivities are already identical at the extremes of the considered energy range. Instead, the XMCD signal on the LD and HD samples has been measured by first subtracting the flat baseline below 63 eV from R_l and R_r and then normalizing the remainder to 1 above 68 eV, which leads to the disappearance of the second peak. In Fig. 6.6 (b) the theoretical XMCD so normalized has been overlapped to the data from the LD sample; the agreement is more consistent. A Gaussian broadening of 0.7 eV has been applied to the calculated XMCD to reproduce the experimental data.

The calculated MOKE rotation at the Ni edge is shown in Fig. 6.7. Unfortunately, data from the samples were available at only one energy, making a comparison impossible and preventing the verification of the simulation accuracy.
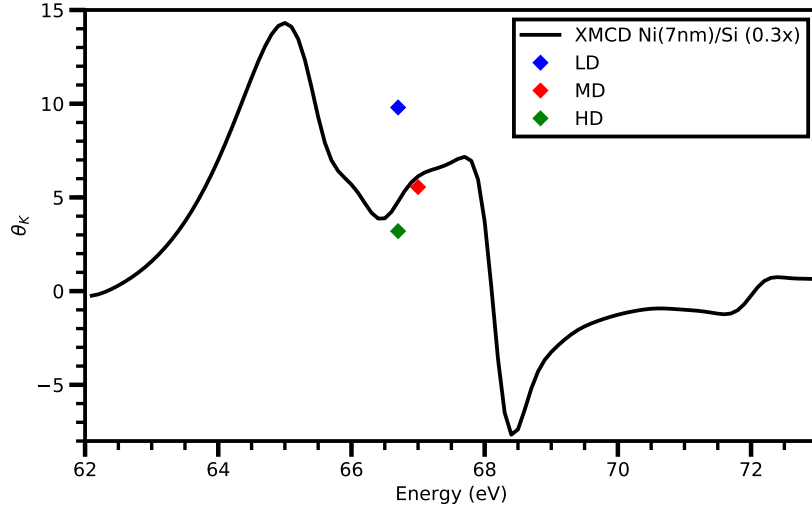
Figure 6.7:   MOKE theoretical amplitude of the hysteresis for the Ni (7nm)/Si stack (black) in longitudinal configuration for a π-polarized incoming beam at $45°$ incidence angle.   The trace has been rescaled by a factor 0.3; the origin of the mismatch may lie in having considered a simplified sample structure.   The measurements on the three samples have been added for comparison (diamond markers).

6.5   Silicon edge modeling

Due to its wide usage in the semiconductor and material technology, silicon has been thoroughly studied. However, despite several standard techniques being employed to investigate the magnetism of metallic magnetic systems, limited data is available on the silicon static magnetic properties. To our best knowledge, there are only two articles on the magnetism on Si in case of Heusler alloys [144, 145]. The measurements on LD and HD, therefore, represent the first attempt to show the magnetism across the whole $L_{2,3}$ edge in great detail.

It is possible to obtain a plausible shape of the dielectric terms by first-principles considerations. In fact, the magneto-optical effects can be derived from the material electrical response $\boldsymbol{P} = \epsilon_0 \hat{\chi} \boldsymbol{E}$, where in the linear range $\hat{\epsilon} = 1 + \hat{\chi}$. Considering a bonded particle of charge q and mass m subject to a form of coupling, its response will be a harmonic oscillation with a driving force plus a damping term [39]

$$m\frac{\partial^2 \boldsymbol{u}}{\partial t^2} + m\gamma\frac{\partial \boldsymbol{u}}{\partial t} + m\omega_0^2 \boldsymbol{u} = q\Big(\boldsymbol{E} + \frac{\partial \boldsymbol{u}}{\partial t} \times \boldsymbol{B}\Big)$$

Supposing a static magnetic field in the z-direction, $\boldsymbol{B} = (0, 0, B)$, an ansatz plane wave solution of the displacement and of the electric field as $exp(-i\omega t)$ can be assumed and, accordingly, the following system of equations can be written

$$\begin{cases} m(\omega^2 + i\gamma\omega - \omega_0^2)x - i\omega qBy = \chi_{xx}\,x + \chi_{xy}\,y \quad = -qE_x \\ m(\omega^2 + i\gamma\omega - \omega_0^2)y + i\omega qBx = \chi_{xx}\,y - \chi_{xy}\,x \quad = -qE_y \\ \qquad\quad m(\omega^2 + i\gamma\omega - \omega_0^2)z = \chi_{xx}\,z \qquad\qquad = -qE_z \end{cases}$$

whence the solutions $\boldsymbol{P} = nq\boldsymbol{u}$ can be obtained. In particular, for the out-of-diagonal components, this system leads to the expression

$$\epsilon_{xy} = -\frac{nq^2}{m\epsilon_0}\frac{i\omega\omega_c}{(\omega^2 + i\gamma\omega_0^2)^2 - \omega^2\omega_c^2}$$

where $\omega_c = qB/m$ is the cyclotron frequency. At zero magnetic field, therefore, the out-of-diagonal term will disappear. In a more rigorous quantum mechanical approach, the correct expression for ϵ_{xy} can be derived from Kubo's expression of conducibility obtained from the current density operators

$$\epsilon_{xy} = -\frac{inq^2}{2m\epsilon_0}\sum_{n<m}(\rho_n - \rho_m)\frac{\omega_{mn}(f_{mn}^+ - f_{mn}^-)}{\omega(\omega_{mn}^2 - (\omega + i\gamma)^2)}$$

where ρ_n is the probability function of the occupation of the state $|n\rangle$ and f_{mn} is the oscillator strength of the optical transition. At absolute zero temperature the expression can be further simplified by considering the initial state $\rho_n = 1$ and the final state $\rho_m = 0$.

The off-diagonal elements arise in case of non-vanishing $\Delta f_{nm} = f_{mn}^+ - f_{mn}^-$, i.e. the difference of the oscillator strength between left and right circular polarization transition modes. As these modes are electric dipole transitions, the total change $\Delta L_z = \pm 1$, implying the presence of a spin-orbit splitting Δ_{SO} for $L_z \neq 0$. Moreover, the effect of magnetization lifts the spin degeneracy, causing a non-vanishing Δf_{nm}. In the case of the $L_{2,3}$ in Si, the dominant transition is 2p $\rightarrow$ 3s [142], with a $\Delta_{SO} = 0.61$ eV in the initial state and with the L_3 transition intensity being twice as big than the L_2 transition.

To simulate a paramagnetic-like behavior of Si, the following form for the dielectric tensor has been considered [39, 157]

$$\epsilon_{xy}(\omega) = -i\frac{nq^2}{2m\epsilon_0}\left[\frac{\omega_0\Delta f_3}{\omega(\omega_0^2 - (\omega - i\gamma)^2)} - \frac{(\omega_0 + \Delta_{SO})\Delta f_2}{\omega((\omega_0 + \Delta_{SO})^2 - (\omega - i\gamma)^2)}\right]$$

where ω_0 corresponds to the L_3 transition. We assume that the the two $\Delta f_{2,3}$ oscillator strengths are opposite in sign, as a diamagnetic-like behavior of Si was imposed. As a result, the unknowns of the system are reduced to the oscillator strengths and the probability scattering γ.

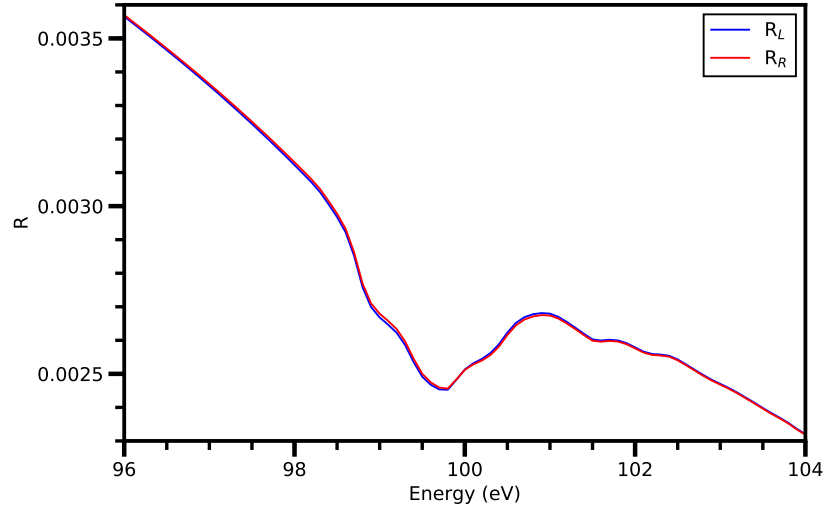## 6.6   XMCD ad MOKE Silicon edge

Figure 6.8:   Reflectivity of a stack of 7 nm of Ni on a Si substrate in the longitudinal configuration for an angle of incidence of $45°$ at the Si $L_{2,3}$ edge. The change in reflectivity is faint but concentrated around the Si edge.

The three parameters Δf_3, Δf_2 and γ have been estimated by comparing the resulting XMCD signal across the Si $L_{2,3}$ edge to the measured signal on the LD sample in the same geometry of the previous calculations at the Ni $M_{2,3}$ edge. Similarly to the experimental conditions at the Ni edge, the XMCD was calculated by subtracting a baseline from the two reflectivities and by normalizing the resulting traces above the edge. The results of the fitting converge to $\Delta f_3 = 0.1996$ and $\Delta f_2 = 0.1002$ for the oscillator strengths and $\gamma = 0.9995$ for the probability scattering. In this case, no Gaussian

broadening has been applied to the calculated XMCD, as the parameter γ from the dielectric tensor produces a similar effect on the resulting trace. It was not possible to estimate the error on these parameters. The positive and negative reflectivity for the Ni(7nm)/Si stack are shown in Fig. 6.8, whereas in Fig. 6.9 the data on the LD sample have been overlapped to the XMCD obtained by the fit parameters.
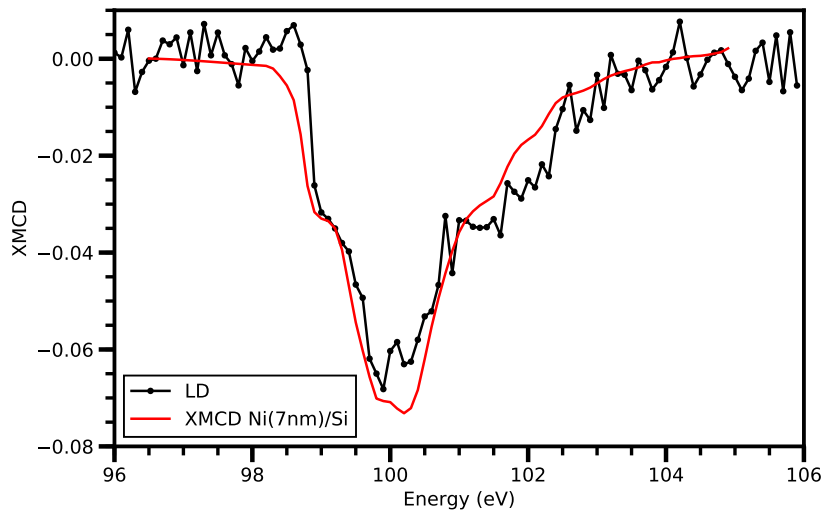

Figure 6.9: XMCD signal on LD (black) compared to the XMCD signal calculated for the Ni (7nm)/Si stack (red) across the Si $L_{2,3}$ edge. A linear baseline calculated below 97 eV was subtracted to the two reflectivities and then the resulting traces were normalized to 1 above 104.5 eV; the XMCD has then been calculated as the difference between the resulting traces. The agreement of the calculated trace is quite good and reproduces correctly the presence of a single peak.

Ultimately, the MOKE signal across the Si $L_{2,3}$ edge has been computed by employing the identical dielectric tensor obtained from the XMCD measurements. Figure 6.10 illustrates a comparison of the amplitude of the hysteresis, measured at various energies along the absorption edge on the three samples, with the theoretical MOKE rotation. Whilst the experimental data points substantially deviate from the theoretical rotation, the energy trend across the edge remains comparatively flat. The source of this discrepancy could be attributed once again to a simplified model of the sample structure. This agrees with the observation that data points do not seem to exhibit any increase in proximity to the resonance. Even though the rotation is ampli-

fied in magnitude below the absorption edge, it is important to acknowledge how shifting towards this energy range forfeits chemical selectivity, hence the intensity of the measured signal diminishes.
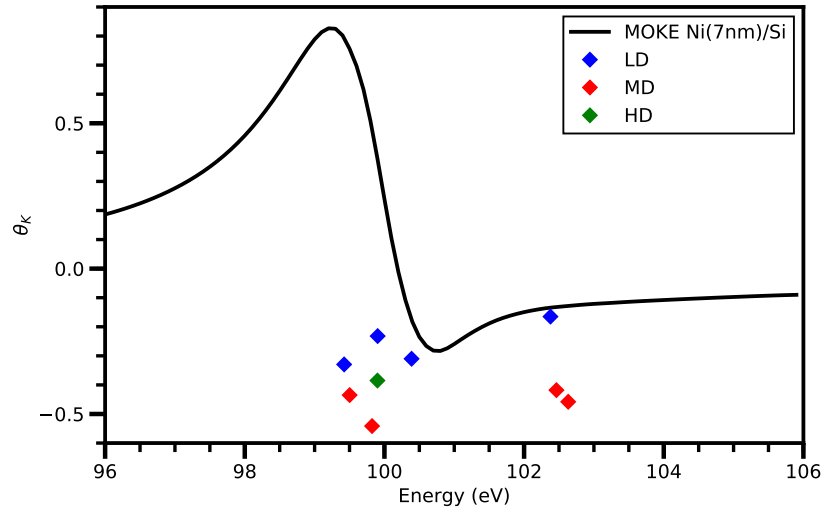

Figure 6.10:   MOKE half amplitude of the hysteresis on LD, MD and HD (diamond markers), compared to the MOKE signal calculated for the Ni (7nm)/Si stack (black) across the Si $L_{2,3}$ edge. The rotation shows a resonance exactly at the edge, whereas above the edge the rotation remains constant.

Conclusion

This thesis undertakes an in-depth investigation of the magnetic properties of Ni/Si interfaces representative of a ferromagnetic/semicondcutor heterostructure, in both static and ultrashort dynamic domains.

The time-resolved measurements at the heart to this thesis are prompted by the prospect of injecting superdiffusive spin currents, engendered by the ultrafast demagnetization of a ferromagnet, into the semiconductor substrate [7]. As per theoretical expectations, the injected current engenders a transient spin dynamics on the subpicosecond timescale. To overcome issues related to interface injection, the laser-induced ultrafast dynamics of a thin Ni layer are utilized and the propagation of the excited electrons in the underlying Si substrate is examined. A suitable magnetic-sensitive resonant technique is required for element-specificity and the successful decoupling of induced dynamics in both the metal thin film and the semiconductor substrate. Standard absorption-based approaches, such as XMCD, are not applicable for depth-sensitive studies as they are surface-restricted. Conversely, Magneto-Optic Kerr Effect (MOKE) techniques provide more suitable access to the magnetic state in the bulk of the material.

The application of the time-resolved resonant MOKE for the examination of magnetic dynamics at the interface requires the creation of innovative instrumentation and data analysis tools. Indeed, data pertaining to the magnetic state of the sample is encoded in the polarization of the reflected beam, making it complex to measure X-ray MOKE effect. To address this, a reflection-based Wollaston-like polarimeter has been specifically developed. This polarimeter has proved to operate successfully when tested on magnetic alloys across the M-absorption edges of the 3d transition materials.

Time-resolved traces reveal distinct magnetic dynamics for the Ni $M_{2,3}$ and Si $L_{2,3}$ absorption edges. The Si signal displays significantly slower dynamics compared to the metal. However, after a few hundred femtoseconds, the two traces converge towards the same demagnetization. This disparity in dynamics can be attributed to the competing mechanisms of substrate

demagnetization and the injection of spin-polarized electrons into the substrate. Specifically, Ni demagnetization initiates the displacement of spin-polarized electrons that propagate within the solid. Simultaneously, the reduction of Ni magnetization quenches the substrate magnetization, as the two are coupled due to the proximity effect. Thus, the differing magnetic dynamics are associated with spin current injection and propagation in the substrate, providing experimental evidence of all-optical spin injection.

Furthermore, from the propagation of the spin current, it has been possible to deduce the spin current velocity in silicon, which establishes a practical benchmark for theoretical expectations in this system.

The design of the experiment is not the only decisive aspect of this thesis; during sample preparation, a special effort has been directed towards enhancing overall sample growth quality alongside the design of the sample itself. The implementation of a substrate passivation procedure aims to prevent the formation of a thick mixed alloy phase layer, which could potentially prove deleterious to subsequent examinations. More specifically, the surface undergoes passivation via the cultivation of a crystalline Si_3N_4 bilayer, above which an epitaxial Ni film of 7 nm is grown, while maintaining the substrate temperature at the level of liquid nitrogen.

Throughout the sample growth process, X-ray photoelectron spectroscopy (XPS) is deployed to monitor sample quality during the various stages of growth. However, an exhaustive Transmission Electron Microscopy (TEM) characterization of the grown interfaces discloses the existence of discontinuous nickel silicide islands beneath the Si_3N_4 layer, potentially attributable to thermal stress-induced fracturing of the nitride layer. Notwithstanding these findings, the analysis verifies that a considerable portion of the sample remains devoid of nickel silicides. Despite their presence, due to their non-magnetic nature, they can only attenuate any measured effect to a minimal degree.

Three samples, composed of $Ag(2nm)/Ni(7nm)/Si_3N_4(0.7nm)/Si$, were cultivated for this thesis, differing solely in substrate doping concentrations. All samples underwent XPS characterization during growth to monitor the deposition and verify sample quality. Post-growth, TEM was utilized to verify the actual thickness of the layers and the quality of the interface. Complementary High-Angle Annular Dark Field (HAADF) characterization facilitated the calculation of the exact chemical profile of Ni and Si across the interface, unveiling a peaked distribution of Ni at the metal layer and a more dispersed distribution of Si. The presence of Si across the entire interface could potentially be ascribed to the mechanical processing of the interface during sample preparation for TEM measurements.

The unexpected presence of a static magnetic state in the semiconductor prompted further investigations into the causes of the proximity effect of the Si electrons in the magnetic field generated by the magnetic film. The focus has been on the presence of a depletion layer region into the semiconductor because of the Schottky barrier, where the screening on the electrons is less effective. As a result, a new batch of samples which varied only by the semiconductor doping has been grown, under the concept of controlling the magnetic properties of the semiconductor by controlling the depletion layer. Indeed, the magnetic dynamics recorded at the Si $L_{2,3}$ edge was different in the three systems, where the most metallic system showing a dynamics closely resembling the metal system. This finding is in agreement with this model, as a thinner depletion layer is both more strongly coupled with the metallic layer and is more quickly traversed by the injected spin current, leading to a vanishing differences of the two traces. Unexpectedly however, the two systems showed opposite magnetization of the substrate, possibly related to the different character of the depletion layer. In fact, as the Fermi energy crosses the conduction bent band at the interface, the pocket that is created can be populated by minority carriers, leading to an opposite magnetic behavior of the substrate.

Following the findings on the low and high-doped systems, the static signal across the whole Si $L_{2,3}$ edge has been explored. The detected nonvanishing XMCD signal across the whole edge confirms without any doubt the presence of a static magnetization in the proximal layer of the semiconductor substrate. Moreover, these measurements represent an important result in the field of Spintronics, as they point out a possible relation between the doping and the magnetic behavior of Si, leading to the design of tunable spintronic devices with increased functionalities.

The static measurements additionally allowed to calculate a plausible form of the out-of-diagonal component of the dielectric tensor, which provides means of predicting magneto-optical effects of silicon-based devices. The results of the calculation have been tested to the observed amplitude of the measured MOKE amplitude across the Si $L_{2,3}$ edge, resulting in a good agreement. Finally, the experimental findings, as well as the calculations employed in this thesis, can call for more in-depth theoretical and experimental investigations aiming at modeling the equilibrium and non-equilibrium dynamics at the magnetic metal/silicon interfaces.

Bibliography

[1] S. Murakami, Naoto N., and S.-C. Zhang. Dissipationless Quantum Spin Current at Room Temperature. *Science*, 301(5638):1348–1351, 2003.

[2] I. Žutić, J. Fabian, and S. Das S. Spintronics: Fundamentals and applications. *Reviews of Modern Physics*, 76(2):323–410, 2004.

[3] B. Huang, D. J. Monsma, and I. Appelbaum. Coherent Spin Transport through a 350 Micron Thick Silicon Wafer. *Physical Review Letters*, 99(17):177209, 2007.

[4] A. M. Tyryshkin, S. Tojo, J. J. L. Morton, H. Riemann, N. V. Abrosimov, P. Becker, H.-J. Pohl, T. Schenkel, M. L. W. Thewalt, K. M. Itoh, and S. A. Lyon. Electron spin coherence exceeding seconds in high-purity silicon. *Nature Materials*, 11(2):143–147, 2012.

[5] I. Žutić and H. Dery. Taming spin currents. *Nature Materials*, 10(9):647–648, 2011.

[6] M. Battiato, K. Carva, and P. M. Oppeneer. Theory of laser-induced ultrafast superdiffusive spin transport in layered heterostructures. *Phys. Rev. B*, 86:024404, Jul 2012.

[7] M. Battiato and K. Held. Ultrafast and Gigantic Spin Injection in Semiconductors. *Physical Review Letters*, 116(19):196601, 2016.

[8] G. Schmidt, D. Ferrand, L. W. Molenkamp, A. T. Filip, and B. J. van Wees. Fundamental obstacle for electrical spin injection from a ferromagnetic metal into a diffusive semiconductor. *Phys. Rev. B*, 62:R4790–R4793, Aug 2000.

[9] E. I. Rashba. Theory of electrical spin injection: Tunnel contacts as a solution of the conductivity mismatch problem. *Phys. Rev. B*, 62:R16267–R16270, Dec 2000.

[10] A. Fert and H. Jaffrès. Conditions for efficient spin injection from a ferromagnetic metal into a semiconductor. *Physical Review B*, 64:184420, Oct 2001.

[11] N. W. Cheung, R. J. Culbertson, L. C. Feldman, P. J. Silverman, K. W. West, and J. W. Mayer. Ni on si(111): Reactivity and interface structure. *Phys. Rev. Lett.*, 45:120–124, Jul 1980.

[12] A. Hiraki. Low temperature reactions at Si/metal interfaces; What is going on at the interfaces? *Surface Science Reports*, 3(7):357–412, 1983.

[13] H. Ahn, C.-L. Wu, S. Gwo, C. M. Wei, and Y. C. Chou. Structure Determination of the Si_3N_4/Si(111)- (8×8) Surface: A Combined Study of Kikuchi Electron Holography, Scanning Tunneling Microscopy, and ab initio Calculations. *Physical Review Letters*, 86(13):2818–2821, 2001.

[14] R. Flammini, P. Allegrini, F. Wiame, R. Belkhou, F. Ronci, S. Colonna, D. M. Trucchi, F. Filippone, S. K. Mahatha, P. M. Sheverdyaeva, and P. Moras. Nearly-free electronlike surface resonance of a β-Si_3N_4(0001)/Si(111)-8×8 interface. *Physical Review B*, 91(7):075303, 2015.

[15] R. Flammini, S. Colonna, P. M. Sheverdyaeva, M. Papagno, A. K. Kundu, and P. Moras. Effect of a subnanometer thin insulator layer at the Ag/Si(111) interface through the observation of quantum well states. *Physical Review Materials*, 5:084604, Aug 2021.

[16] P. Rajak, R. Ciancio, A. Caretta, S. Laterza, R. Bhardwaj, M. Jugovac, M. Malvestuto, P. Moras, and R. Flammini. Evidence of silicide at the Ni/β-Si_3N_4(0001)/Si(111) interface. *Applied Surface Science*, 623:156986, 2023.

[17] E. Allaria, D. Castronovo, P. Cinquegrana, P. Craievich, M. Dal Forno, M. B. Danailov, G. D'Auria, A. Demidovich, G. De Ninno, S. Di Mitri, B. Diviacco, W. M. Fawley, M. Ferianis, E. Ferrari, L. Froehlich, G. Gaio, D. Gauthier, L. Giannessi, R. Ivanov, B. Mahieu, N. Mahne, I. Nikolov, F. Parmigiani, G. Penco, L. Raimondi, C. Scafuri, C. Serpico, P. Sigalotti, S. Spampinati, C. Spezzani, M. Svandrlik, C. Svetina, M. Trovo, M. Veronese, D. Zangrando, and M. Zangrando. Two-stage seeded soft-X-ray free-electron laser. *Nature Photonics*, 7(11):913–918, 10 2013.

[18] A. Caretta, S. Laterza, V. Bonanni, R. Sergo, C. Dri, G. Cautero, F. Galassi, M. Zamolo, A. Simoncig, M. Zangrando, A. Gessini, S. Dal Zilio, R. Flammini, P. Moras, A. Demidovich, M. Danailov, F. Parmigiani, and M. Malvestuto. A novel free-electron laser single-pulse Wollaston polarimeter for magneto-dynamical studies. *Structural Dynamics*, 8(3):034304, 2021.

[19] A. Caretta, S. Laterza, and M. Malvestuto. Apparatus for measuring the polarization of an electromagnetic radiation and corresponding method of use, Sep 2022.

[20] S. Laterza, A. Caretta, R. Bhardwaj, R. Flammini, P. Moras, M. Jugovac, P. Rajak, M. Islam, R. Ciancio, V. Bonanni, B. Casarin, A. Simoncig, M. Zangrando, P. R. Ribič, G. Penco, G. De Ninno, L. Giannessi, A. Demidovich, M. Danailov, F. Parmigiani, and M. Malvestuto. All-optical spin injection in silicon investigated by element-specific time-resolved Kerr effect. *Optica*, 9(12):1333–1338, Dec 2022.

[21] M. Faraday. I. On the magnetic relations and characters of the metals. *The London, Edinburgh, and Dublin Philosophical Magazine and Journal of Science*, 27(177):1–3, 1845.

[22] J. Kerr. XLIII. On rotation of the plane of polarization by reflection from the pole of a magnet. *The London, Edinburgh, and Dublin Philosophical Magazine and Journal of Science*, 3(19):321–343, 1877.

[23] W. Voigt. Zur theorie der magneto-optischen erscheinungen. *Annalen der Physik*, 303(2):345–365, 1899.

[24] P. Zeeman. Over de invloed eener magnetisatie op den aard van het door een stof uitgezonden licht. *Verslagen en Mededeelingen der Kon. Academie van Wetenschappen, Afd. Natuurkunde*, 5:181–184, 1896.

[25] H. R. Hulme and R. H. Fowler. The Faraday effect in ferromagnetics. *Proceedings of the Royal Society of London. Series A, Containing Papers of a Mathematical and Physical Character*, 135(826):237–257, 1932.

[26] J. L. Erskine and E. A. Stern. Calculation of the M_{23} magneto-optical absorption spectrum of ferromagnetic nickel. *Phys. Rev. B*, 12:5016–5024, Dec 1975.

[27] G. Schütz, W. Wagner, W. Wilhelm, P. Kienle, R. Zeller, R. Frahm, and G. Materlik. Absorption of Circularly Polarized X Rays in Iron. *Phys. Rev. Lett.*, 58:737–740, Feb 1987.

[28] G. van der Laan. Anisotropic X-ray Magnetic Linear Dichroism. In Eric Beaurepaire, Hervé Bulou, Loic Joly, and Fabrice Scheurer, editors, *Magnetism and Synchrotron Radiation: Towards the Fourth Generation Light Sources*, pages 239–256, Cham, 2013. Springer International Publishing.

[29] G. van der Laan, B. T. Thole, G. A. Sawatzky, J. B. Goedkoop, J. C. Fuggle, J.-M. Esteva, R. Karnatak, J. P. Remeika, and H. A. Dabkowska. Experimental proof of magnetic x-ray dichroism. *Phys. Rev. B*, 34:6529–6531, Nov 1986.

[30] D. P. Siddons, M. Hart, Y. Amemiya, and J. B. Hastings. X-ray optical activity and the Faraday effect in cobalt and its compounds. *Phys. Rev. Lett.*, 64:1967–1970, Apr 1990.

[31] K. Mori, K. Namikawa, Y. Koyama, and M. Ando. Observation of X-ray Magnetic Kerr Rotation at Gd L Absorption Edges. *Japanese Journal of Applied Physics*, 32(S2):323, jan 1993.

[32] T. Koide, T. Shidara, H. Fukutani, K. Yamaguchi, A. Fujimori, and S. Kimura. Strong magnetic circular dichroism at the $M_{2,3}$ edges in ferromagnetic Ni and ferrimagnetic Fe_3O_4. *Physical Review B*, 44(9):4697–4700, 1991.

[33] L. Onsager. Reciprocal Relations in Irreversible Processes. I. *Phys. Rev.*, 37:405–426, Feb 1931.

[34] W. H. Kleiner. Space-Time Symmetry of Transport Coefficients. *Phys. Rev.*, 142:318–326, Feb 1966.

[35] P. V. Pantulu and E. Sudarshan. Magnetic symmetry and Onsager relations. In *Proceedings of the Indian Academy of Sciences-Section A*, volume 69, pages 279–283. Springer India New Delhi, 1969.

[36] P.M. Oppeneer. Chapter 3 magneto-optical Kerr spectra. volume 13 of *Handbook of Magnetic Materials*, pages 229–422. Elsevier, 2001.

[37] S. J. Byrnes. Multilayer optical calculations, 2020. arXiv:1603.02720.

[38] S. Yamamoto and I. Matsuda. Measurement of the Resonant Magneto-Optical Kerr Effect Using a Free Electron Laser. *Applied Sciences*, 7(7), 2017.

[39] Katsuaki Sato and Takayuki Ishibashi. Fundamentals of magneto-optical spectroscopy. *Frontiers in Physics*, 10, 2022.

[40] J. Zak, E. R. Moog, C. Liu, and S. D. Bader. Magneto-optics of multilayers with arbitrary magnetization directions. *Phys. Rev. B*, 43:6423–6429, Mar 1991.

[41] T. Yoshino and S. Tanaka. Longitudinal Magneto-Optic Effect in Ferromagnetic Thin Films. I. *Japanese Journal of Applied Physics*, 5(11):989, nov 1966.

[42] C.-Y. You and S.-C. Shin. Derivation of simplified analytic formulae for magneto-optical Kerr effects. *Applied Physics Letters*, 69(9):1315–1317, 08 1996.

[43] E. Beaurepaire, J.-C. Merle, A. Daunois, and J.-Y. Bigot. Ultrafast Spin Dynamics in Ferromagnetic Nickel. *Phys. Rev. Lett.*, 76:4250–4253, May 1996.

[44] A. Einstein and W. J. De Haas. Experimental proof of the existence of Ampère's molecular currents. In *Proc. KNAW*, volume 181, page 696, 1915.

[45] B. Koopmans, J. J. M. Ruigrok, F. Dalla Longa, and W. J. M. de Jonge. Unifying ultrafast magnetization dynamics. *Phys. Rev. Lett.*, 95:267207, Dec 2005.

[46] M. Wietstruk, A. Melnikov, C. Stamm, T. Kachel, N. Pontius, M. Sultan, C. Gahl, M. Weinelt, H. A. Dürr, and U. Bovensiepen. Hot-Electron-Driven Enhancement of Spin-Lattice Coupling in Gd and Tb $4f$ Ferromagnets Observed by Femtosecond X-Ray Magnetic Circular Dichroism. *Phys. Rev. Lett.*, 106:127401, Mar 2011.

[47] M. Krauß, T. Roth, S. Alebrand, D. Steil, M. Cinchetti, M. Aeschlimann, and H. C. Schneider. Ultrafast demagnetization of ferromagnetic transition metals: The role of the coulomb interaction. *Phys. Rev. B*, 80:180407, Nov 2009.

[48] M. Battiato. *Superdiffusive Spin Transport and Ultrafast Magnetization Dynamics: Femtosecond spin transport as the route to ultrafast spintronics.* PhD thesis, University of Uppsala, 2013.

[49] Bert Koopmans. *Time-resolved Kerr-effect and Spin Dynamics in Itinerant Ferromagnets.* John Wiley & Sons, Ltd, 2007.

[50] Bert Koopmans. *Laser-Induced Magnetization Dynamics*, pages 256–323. Springer Berlin Heidelberg, Berlin, Heidelberg, 2003.

[51] M. Ikezawa. Temporary Bleaching of the M Band in KBr and KCl. *Journal of the Physical Society of Japan*, 19(4):529–539, 1964.

[52] J. Hohlfeld, E. Matthias, R. Knorren, and K. H. Bennemann. Nonequilibrium magnetization dynamics of nickel. *Phys. Rev. Lett.*, 78:4861–4864, Jun 1997.

[53] C. Stamm, T. Kachel, N. Pontius, R. Mitzner, T. Quast, K. Holldack, S. Khan, C. Lupulescu, M. Aziz, E. F.and Wietstruk, H. A. Dürr, and W. Eberhardt. Femtosecond modification of electron localization and transfer of angular momentum in nickel. *Nature Materials*, 6:740–743, 2007.

[54] S. Valencia, A. Gaupp, W. Gudat, H.-Ch. Mertins, P. M. Oppeneer, D. Abramsohn, and C. M. Schneider. Faraday rotation spectra at shallow core levels: 3p edges of Fe, Co, and Ni. *New Journal of Physics*, 8(10):254, oct 2006.

[55] Sh. Yamamoto, M. Taguchi, M. Fujisawa, R. Hobara, S. Yamamoto, K. Yaji, T. Nakamura, K. Fujikawa, R. Yukawa, T. Togashi, M. Yabashi, M. Tsunoda, S. Shin, and I. Matsuda. Observation of a giant Kerr rotation in a ferromagnetic transition metal by M-edge resonant magneto-optic Kerr effect. *Phys. Rev. B*, 89:064423, Feb 2014.

[56] C. Svetina, N. Mahne, L. Raimondi, A. Caretta, B. Casarin, M. Dell'Angela, M. Malvestuto, F. Parmigiani, and M. Zangrando. MagneDyn: the beamline for magneto dynamics studies at FERMI. *Journal of Synchrotron Radiation*, 23(1):98–105, 2016.

[57] M. Malvestuto, A. Caretta, R. Bhardwaj, S. Laterza, F. Parmigiani, A. Gessini, M. Zamolo, F. Galassi, R. Sergo, G. Cautero, M. B.

Danailov, A. Demidovic, P. Sigalotti, M. Lonza, R. Borghes, A. Contillo, A. Simoncig, M. Manfredda, L. Raimondi, and M. Zangrando. The MagneDyn beamline at the FERMI free electron laser. *Review of Scientific Instruments*, 93(11):115109, 2022.

[58] M. Donker. *Ultrafast optically-induced magnetization and conductivity dynamics in the europium chalcogenides.* PhD thesis, University of Groningen, 2014.

[59] J. Stöhr and H. C. Siegmann. Magnetism. *Solid-State Sciences. Springer, Berlin, Heidelberg*, 5:236, 2006.

[60] B. T. Thole and G. van der Laan. Sum rules for magnetic dichroism in rare earth 4f photoemission. *Phys. Rev. Lett.*, 70:2499–2502, Apr 1993.

[61] P. Carra, B. T. Thole, M. Altarelli, and X. Wang. X-ray circular dichroism and local magnetic fields. *Physical Review Letters*, 70:694–697, Feb 1993.

[62] M. Altarelli. Sum rules for x-ray magnetic circular dichroism. *Il Nuovo Cimento D*, 20:1067–1073, 1998.

[63] A. Scherz, H. Wende, C. Sorg, K. Baberschke, J. Minr, D. Benea, and H. Ebert. Limitations of integral XMCD sum-rules for the early 3d elements. *Physica Scripta*, 2005(T115):586, jan 2005.

[64] C. Piamonteze, P. Miedema, and F. M. F. de Groot. Accuracy of the spin sum rule in XMCD for the transition-metal L edges from manganese to copper. *Phys. Rev. B*, 80:184410, Nov 2009.

[65] F. M. F. de Groot, J. C. Fuggle, B. T. Thole, and G. A. Sawatzky. $L_{2,3}$ x-ray-absorption edges of d^0 compounds: K^+, Ca^{2+}, Sc^{3+}, and Ti^{4+} in O_h (octahedral) symmetry. *Phys. Rev. B*, 41:928–937, Jan 1990.

[66] G. Y. Guo. Spin- and orbital-polarized multiple-scattering theory of magneto-x-ray effects in Fe, Co, and Ni. *Phys. Rev. B*, 55:11619–11628, May 1997.

[67] C. T. Chen, Y. U. Idzerda, H.-J. Lin, N. V. Smith, G. Meigs, E. Chaban, G. H. Ho, E. Pellegrin, and F. Sette. Experimental Confirmation of the X-Ray Magnetic Circular Dichroism Sum Rules for Iron and Cobalt. *Phys. Rev. Lett.*, 75:152–155, Jul 1995.

[68] B. H. Frazer, B. Gilbert, B. R. Sonderegger, and G. De Stasio. The probing depth of total electron yield in the sub-keV range: TEY-XAS and X-PEEM. *Surface Science*, 537(1):161–167, 2003.

[69] R. Nakajima, J. Stöhr, and Y. U. Idzerda. Electron-yield saturation effects in L-edge x-ray magnetic circular dichroism spectra of Fe, Co, and Ni. *Phys. Rev. B*, 59:6421–6429, Mar 1999.

[70] S. Eisebitt, T. Böske, J.-E. Rubensson, and W. Eberhardt. Determination of absorption coefficients for concentrated samples by fluorescence detection. *Phys. Rev. B*, 47:14103–14109, Jun 1993.

[71] A. Derossi, F. Lama, M. Piacentini, T. Prosperi, and N. Zema. High flux and high resolution beamline for elliptically polarized radiation in the vacuum ultraviolet and soft x-ray regions. *Review of scientific instruments*, 66(2):1718–1720, 1995.

[72] H. A. Padmore. Optimization of soft x-ray monochromators (invited). *Review of Scientific Instruments*, 60(7):1608–1615, 07 1989.

[73] H. A. Kramers. Wellenmechanik und halbzahlige quantisierung. *Zeitschrift fur Physik*, 39:828–840, 1926.

[74] A. Sommerfeld and H. Bethe. *Elektronentheorie der metalle*, volume 19. Springer-Verlag, 2013.

[75] R. Holm. Der zeitliche verlauf der erwärmung eines metallischen kontaktes. *Archiv für Elektrotechnik*, 29:207–210, 1935.

[76] K. M. Chu and D. L. Pulfrey. An improved analytic model for the metal-insulator-semiconductor tunnel junction. *IEEE Transactions on Electron Devices*, 35(10):1656–1663, 1988.

[77] J. Maserjian. Tunneling in thin MOS structures. *Journal of Vacuum Science and Technology*, 11(6):996–1003, 11 1974.

[78] F.A. Padovani and R. Stratton. Field and thermionic-field emission in Schottky barriers. *Solid-State Electronics*, 9(7):695–707, 1966.

[79] J.P. Gambino and E.G. Colgan. Silicides and ohmic contacts. *Materials Chemistry and Physics*, 52(2):99–146, 1998.

[80] F. Braun. On the electrical conductivity of sulphides. *Poggendorff's Annalen*, 153:556–63, 1874.

[81] W. Schottky and W. Schottky. Einleitung: Entwicklung und aufgabe der thermodynamik. *Thermodynamik: Die Lehre von den Kreisprozessen den Physikalischen und Chemischen Veränderungen und Gleichgewichten Eine Hinführung zu den Thermodynamischen Problemen Unserer Kraft-und Stoffwirtschaft*, pages 1–4, 1929.

[82] W. Schottky. Halbleitertheorie der sperrschicht. *Naturwissenschaften*, 26(52):843–843, 1938.

[83] J. Bardeen. Surface States and Rectification at a Metal Semi-Conductor Contact. *Phys. Rev.*, 71:717–727, May 1947.

[84] J. D. Dow, R. E. Allen, and O. F. Sankey. *Intrinsic and Extrinsic Surface Electronic States of Semiconductors*, pages 483–500. Springer Berlin Heidelberg, Berlin, Heidelberg, 1984.

[85] J. H. Werner and H. H. Güttler. Barrier inhomogeneities at Schottky contacts. *Journal of Applied Physics*, 69(3):1522–1533, 02 1991.

[86] W Monch. On the physics of metal-semiconductor interfaces. *Reports on Progress in Physics*, 53(3):221, mar 1990.

[87] S. M. Sze, Y. Li, and K. K. Ng. *Physics of semiconductor devices*. John wiley & sons, 2021.

[88] W. Mönch. *Semiconductor surfaces and interfaces*, volume 26. Springer Science & Business Media, 2013.

[89] R. T. Tung. Recent advances in Schottky barrier concepts. *Materials Science and Engineering: R: Reports*, 35(1):1–138, 2001.

[90] E. H. Rhoderick. *Surfaces and Interfaces in Semiconductor Technology*, pages 3–28. Springer US, Boston, MA, 1978.

[91] G. Ottaviani. Review of binary alloy formation by thin film interactions. *Journal of Vacuum Science and Technology*, 16(5):1112–1119, 09 1979.

[92] K. N. Tu. Interdiffusion and reaction in thin films. *Electronic Thin-Film Reliability*, pages 170–191, 2010.

[93] H. Föll, P. S. Ho, and K. N. Tu. Transmission electron microscopy of the formation of nickel silicides. *Philosophical Magazine A*, 45(1):31–47, 1982.

[94] M. A. Sobolewski and C. R. Helms. Properties of ultrathin thermal nitrides in silicon Schottky barrier structures. *Applied Physics Letters*, 54(7):638–640, 1989.

[95] N. W. Ashcroft and N. D. Mermin. *Solid state physics*. Cengage Learning, 2022.

[96] K. Misiakos, E. Tsoi, and A. Neugroschel. Complete characterization of transport parameters in semiconductor substrates through lateral bipolar transistor measurements. *Journal of Applied Physics*, 72(5):1894–1900, 09 1992.

[97] G. Masetti, M. Severi, and S. Solmi. Modeling of carrier mobility against carrier concentration in arsenic-, phosphorus-, and boron-doped silicon. *IEEE Transactions on Electron Devices*, 30(7):764–769, Jul 1983.

[98] W. S. M. Werner, K. Glantschnig, and C. Ambrosch-Draxl. Optical constants and inelastic electron-scattering data for 17 elemental metals. *Journal of Physical and Chemical Reference Data*, 38(4):1013–1092, 2009.

[99] B.-H. Kim, M.-S. Cho, and H.-G. Woo. Si-Si/Si-C/Si-O/Si-N coupling of hydrosilanes to useful silicon-containing materials. *Synlett*, 2004(05):0761–0772, 2004.

[100] R. Flammini, R. Belkhou, F. Wiame, S. Iacobucci, and A. Taleb-Ibrahimi. Crystalline silicon nitride passivating the Si(111) surface: A study of the au growth mode. *Surface Science*, 579(2):188–196, 2005.

[101] A. C. Miller and G. W. Simmons. Nickel by XPS. *Surface Science Spectra*, 1(3):312–317, 09 1992.

[102] A. N. Mansour. Nickel Monochromated Al Ka XPS Spectra from the Physical Electronics Model 5400 Spectrometer. *Surface Science Spectra*, 3(3):221–230, 07 1994.

[103] J. B. Malherbe. Sputtering of compound semiconductor surfaces. I. Ion-solid interactions and sputtering yields. *Critical Reviews in Solid State and Materials Sciences*, 19(2):55–127, 1994.

[104] V. P. Zhukov, E. V. Chulkov, and P. M. Echenique. Lifetimes and inelastic mean free path of low-energy excited electrons in Fe, Ni, Pt,

and Au: Ab initio GW + T calculations. *Phys. Rev. B*, 73:125105, Mar 2006.

[105] M. Battiato, K. Carva, and P. M. Oppeneer. Superdiffusive Spin Transport as a Mechanism of Ultrafast Demagnetization. *Physical Review Letters*, 105(2):027203, 2010.

[106] D. D. Awschalom and M. E. Flatté. Challenges for semiconductor spintronics. *Nature Physics*, 3(3):153–159, 2007.

[107] K. L. Wang, J. G. Alzate, and P. K. Amiri. Low-power non-volatile spintronic memory: STT-RAM and beyond. *Journal of Physics D: Applied Physics*, 46(7):074003, 2013.

[108] D. Rudolf, C. La-O-Vorakiat, M. Battiato, R. Adam, J. M. Shaw, E. Turgut, P. Maldonado, S. Mathias, P. Grychtol, H. T. Nembach, T. J. Silva, M. Aeschlimann, H. C. Kapteyn, M. M. Murnane, C. M. Schneider, and P. M. Oppeneer. Ultrafast magnetization enhancement in metallic multilayers driven by superdiffusive spin current. *Nature Communications*, 3(1):1037, 2012.

[109] T. Kampfrath, M. Battiato, P. Maldonado, G. Eilers, J. Nötzold, S. Mährlein, V. Zbarsky, F. Freimuth, Y. Mokrousov, S. Blügel, M. Wolf, I. Radu, P. M. Oppeneer, and M. Münzenberg. Terahertz spin current pulses controlled by magnetic heterostructures. *Nature Nanotechnology*, 8(4):256–260, 04 2013.

[110] X.-P. He, P.-H. Huang, X.-Y. Yang, Z.-M. Jin, S.-T. Lou, X.-L. Zhang, and Q.-Y. Jin. Comparative study of coherent terahertz emission from Fe/Pt ferromagnetic heterostructures. *Chin. Opt. Lett.*, 17(8):081601, Aug 2019.

[111] T. Seifert, S. Jaiswal, U. Martens, J. Hannegan, L. Braun, P. Maldonado, F. Freimuth, A. Kronenberg, J. Henrizi, I. Radu, E. Beaurepaire, Y. Mokrousov, P. M. Oppeneer, M. Jourdan, G. Jakob, D. Turchinovich, L. M. Hayden, M. Wolf, M. Münzenberg, M. Kläui, and T. Kampfrath. Efficient metallic spintronic emitters of ultrabroadband terahertz radiation. *Nature Photonics*, 10(7):483–488, 2016.

[112] K. Lee, D.-K. Lee, D. Yang, R. Mishra, D.-J. Kim, S. Liu, Q. Xiong, S. K. Kim, K.-J. Lee, and H. Yang. Superluminal-like magnon propagation in antiferromagnetic NiO at nanoscale distances. *Nature Nanotechnology*, 16(12):1337–1341, 2021.

[113] A. M. Tyryshkin, S. A. Lyon, A. V. Astashkin, and A. M. Raitsimring. Electron spin relaxation times of phosphorus donors in silicon. *Physical Review B*, 68(19):193207, 2003.

[114] V. Sverdlov and S. Selberherr. Silicon spintronics: Progress and challenges. *Physics Reports*, 585:1–40, 2015.

[115] R. Jansen. Silicon spintronics. *Nature Materials*, 11(5):400–408, 2012.

[116] X. Liu, A. Merhe, E. Jal, R. Delaunay, R. Jarrier, V. Chardonnet, M. Hennes, S. G. Chiuzbaian, K. Légaré, M. Hennecke, I. Radu, C. Von Korff Schmising, S. Grunewald, M. Kuhlmann, J. Lüning, and B. Vodungbo. Sub-15-fs X-ray pump and X-ray probe experiment for the study of ultrafast magnetization dynamics in ferromagnetic alloys. *Opt. Express*, 29(20):32388–32403, Sep 2021.

[117] M. B. Danailov, F. Bencivenga, F. Capotondi, F. Casolari, P. Cinquegrana, A. Demidovich, E. Giangrisostomi, M. P. Kiskinova, G. Kurdi, M. Manfredda, C. Masciovecchio, R. Mincigrucci, I. P. Nikolov, E. Pedersoli, E. Principi, and P. Sigalotti. Towards jitter-free pump-probe measurements at seeded free electron laser facilities. *Optics Express*, 22(11):12869, 2014.

[118] Y. Liu, M. M. Aziz, A. Shalini, C. D. Wright, and R. J. Hicken. Crystallization of Ge2Sb2Te5 films by amplified femtosecond optical pulses. *Journal of Applied Physics*, 112(12):123526, 2012.

[119] M. Polyanskiy. Refractive index database. http://refractiveindex.info, 2008. Accessed: 2021-06-28.

[120] A. Eschenlohr, M. Battiato, P. Maldonado, N. Pontius, T. Kachel, K. Holldack, R. Mitzner, A. Föhlisch, P. M. Oppeneer, and C. Stamm. Ultrafast spin transport as key to femtosecond demagnetization. *Nature Materials*, 12(4):332–336, 2013.

[121] A. Dankert, R. S. Dulal, and S. P. Dash. Efficient Spin Injection into Silicon and the Role of the Schottky Barrier. *Scientific Reports*, 3(1):3196, 2013.

[122] A. Dahal, J. Gunasekera, L. Harringer, D. K. Singh, and D. J. Singh. Metallic nickel silicides: Experiments and theory for NiSi and first principles calculations for other phases. *Journal of Alloys and Compounds*, 672:110–116, 2016.

[123] L. Ma, J. Zhao, J. Wang, B. Wang, and G. Wang. Magnetic properties of transition-metal impurities in silicon quantum dots. *Physical Review B*, 75:045312, Jan 2007.

[124] M Battiato. Spin polarisation of ultrashort spin current pulses injected in semiconductors. *Journal of Physics: Condensed Matter*, 29(17):174001, 2017.

[125] S. P. Dash, S. Sharma, R. S. Patel, M. P. de Jong, and R. Jansen. Electrical creation of spin polarization in silicon at room temperature. *Nature*, 462(7272):491–494, 2009.

[126] R. C. Myers, A. C. Gossard, and D. D. Awschalom. Tunable spin polarization in III-V quantum wells with a ferromagnetic barrier. *Physical Review B*, 69(16):161305, 2004.

[127] M. A. Pankov, B. A. Aronzon, V. V. Rylkov, A. B. Davydov, E. Z. Meĭlikhov, R. M. Farzetdinova, E. M. Pashaev, M. A. Chuev, I. A. Subbotin, I. A. Likhachev, B. N. Zvonkov, A. V. Lashkul, and R. Laiho. Ferromagnetic transition in GaAs/Mn/GaAs/In x Ga 1- x As/GaAs structures with a two-dimensional hole gas.. *Journal of Experimental & Theoretical Physics*, 109(2), 2009.

[128] V. L. Korenev, M. Salewski, I. A. Akimov, V. F. Sapega, L. Langer, I. V. Kalitukha, J. Debus, R. I. Dzhioev, D. R. Yakovlev, D. Müller, C. Schröder, H. Hövel, G. Karczewski, M. Wiater, T. Wojtowicz, Yu. G. Kusrayev, and M. Bayer. Long-range p–d exchange interaction in a ferromagnet–semiconductor hybrid structure. *Nature Physics*, 12:85–91, 2016.

[129] R. K. Kawakami, Y. Kato, M. Hanson, I. Malajovich, J. M. Stephens, E. Johnston-Halperin, G. Salis, A. C. Gossard, and D. D. Awschalom. Ferromagnetic imprinting of nuclear spins in semiconductors. *Science*, 294(5540):131–134, 2001.

[130] R. J. Epstein, I. Malajovich, R. K. Kawakami, Y. Chye, M. Hanson, P. M. Petroff, A. C. Gossard, and D. D. Awschalom. Spontaneous spin coherence in n-GaAs produced by ferromagnetic proximity polarization. *Phys. Rev. B*, 65:121202, Mar 2002.

[131] T. Dietl. A ten-year perspective on dilute magnetic semiconductors and oxides. *Nature Materials*, 9:965–974, 2010.

[132] H. Höchst, D. Zhao, and D. L. Huber. $M_{2,3}$ magnetic circular dichroism (MCD) measurements of Fe, Co and Ni using a newly developed quadruple reflection phase shifter. *Surface science*, 352:998–1002, 1996.

[133] F. Willems, S. Sharma, C. v. Korff Schmising, J. K. Dewhurst, L. Salemi, D. Schick, P. Hessing, C. Strüber, W. D. Engel, and S. Eisebitt. Magneto-Optical Functions at the $3p$ Resonances of Fe, Co, and Ni: Ab initio Description and Experiment. *Phys. Rev. Lett.*, 122:217202, May 2019.

[134] F. C. Brown, R. Z. Bachrach, and M. Skibowski. $L_{2,3}$ threshold spectra of doped silicon and silicon compounds. *Physical Review B*, 15:4781–4788, May 1977.

[135] M. Kasrai, W. N. Lennard, R. W. Brunner, G .M. Bancroft, J. A. Bardwell, and K. H. Tan. Sampling depth of total electron and fluorescence measurements in Si L-and K-edge absorption spectroscopy. *Applied Surface Science*, 99(4):303–312, 1996.

[136] Y. F. Hu, R. Boukherroub, and T. K. Sham. Near edge x-ray absorption fine structure spectroscopy of chemically modified porous silicon. *Journal of electron spectroscopy and related phenomena*, 135(2-3):143–147, 2004.

[137] G. E. van Dorssen, M. D. Roper, H. A. Padmore, A. D. Smith, and G. N. Greaves. Core excitons in silicon and silicon oxides. *Review of scientific instruments*, 66(2):1480–1482, 1995.

[138] G. Lucovsky. Multiplet Theory for Conduction Band Edge and O-Vacancy Defect States in SiO_2, Si_3N_4, and Si Oxynitride Alloy Thin Films. *Japanese Journal of Applied Physics*, 50(4S):04DC09, apr 2011.

[139] S. Leitch, A. Moewes, L. Ouyang, W. Y. Ching, and T. Sekine. Properties of non-equivalent sites and bandgap of spinel-phase silicon nitride. *Journal of Physics: Condensed Matter*, 16(36):6469, 2004.

[140] L. Aballe, L. Gregoratti, A. Barinov, M. Kiskinova, T. Clausen, S. Gangopadhyay, and J. Falta. Interfacial interactions at $Au/Si_3N_4/Si(111)$ and $Ni/Si_3N_4/Si(111)$ structures with ultrathin nitride films. *Applied Physics Letters*, 84(24):5031–5033, 05 2004.

[141] P. L. Tam and L. Nyborg. Sputter deposition and XPS analysis of nickel silicide thin films. *Surface and Coatings Technology*, 203(19):2886–2890, 2009.

[142] A. Bianconi, R. Del Sole, A. Selloni, P. Chiaradia, M. Fanfoni, and I. Davoli. Partial density of unoccupied states and $L_{2,3}$-x-ray absorption spectrum of bulk silicon and of the Si(1 1 1) 2×1 surface. *Solid State Communications*, 64(10):1313–1316, 1987.

[143] R. Wu and A. J. Freeman. Limitation of the Magnetic-Circular-Dichroism Spin Sum Rule for Transition Metals and Importance of the Magnetic Dipole Term. *Physical Review Letters*, 73:1994–1997, Oct 1994.

[144] C. Antoniak, H. C. Herper, Y. N. Zhang, A. Warland, T. Kachel, F. Stromberg, B. Krumme, C. Weis, K. Fauth, W. Keune, P. Entel, R. Q. Wu, J. Lindner, and H. Wende. Induced magnetism on silicon in Fe_3Si quasi-Heusler compound. *Physical Review B*, 85(21):214432, 2012.

[145] M. Emmel, A. Alfonsov, D. Legut, A. Kehlberger, E. Vilanova, I.P. Krug, D.M. Gottlob, M. Belesi, B. Büchner, M. Kläui, P.M. Oppeneer, S. Wurmehl, H.J. Elmers, and G. Jakob. Electronic properties of Co_2FeSi investigated by X-ray magnetic linear dichroism. *Journal of Magnetism and Magnetic Materials*, 368:364–373, 2014.

[146] S. S. Dhesi, H. A. Dürr, G. van der Laan, E. Dudzik, and N. B. Brookes. Electronic and magnetic structure of thin Ni films on Co/Cu(001). *Physical Review B*, 60:12852–12860, Nov 1999.

[147] H.-E. Schaefer, H. Kisker, H. Kronmüller, and R. Würschum. Magnetic properties of nanocrystalline nickel. *Nanostructured Materials*, 1(6):523–529, 1992.

[148] P. Blaha, K. Schwarz, F. Tran, R. Laskowski, G. K. H. Madsen, and L. D. Marks. WIEN2k: An APW+lo program for calculating the properties of solids. *The Journal of Chemical Physics*, 152(7), 02 2020. 074101.

[149] B.L. Henke, E.M. Gullikson, and J.C. Davis. X-Ray Interactions: Photoabsorption, Scattering, Transmission, and Reflection at E = 50-30,000 eV, Z = 1-92. *Atomic Data and Nuclear Data Tables*, 54(2):181–342, 1993.

[150] N. Mainkar, D. A. Browne, and J. Callaway. First-principles LCGO calculation of the magneto-optical properties of nickel and iron. *Phys. Rev. B*, 53:3692–3701, Feb 1996.

[151] T. G. Mackay and A. Lakhtakia. The transfer-matrix method in electromagnetics and optics. *Synthesis lectures on electromagnetics*, 1(1):1–126, 2020.

[152] S Macke and E Goering. Magnetic reflectometry of heterostructures. *Journal of Physics: Condensed Matter*, 26(36):363201, aug 2014.

[153] M. Mansuripur. Analysis of multilayer thin-film structures containing magneto-optic and anisotropic media at oblique incidence using 2×2 matrices. *Journal of Applied Physics*, 67(10):6466–6475, 05 1990.

[154] J. Zak, E. R. Moog, C. Liu, and S. D. Bader. Fundamental magneto-optics. *Journal of Applied Physics*, 68(8):4203–4207, 10 1990.

[155] M. Sacchi and A. Mirone. Resonant reflectivity from a Ni(110) crystal: Magnetic effects at the Ni $2p$ edges using linearly and circularly polarized photons. *Phys. Rev. B*, 57:8408–8415, Apr 1998.

[156] H.-Ch. Mertins, D. Abramsohn, A. Gaupp, F. Schäfers, W. Gudat, O. Zaharko, H. Grimmer, and P. M. Oppeneer. Resonant magnetic reflection coefficients at the Fe $2p$ edge obtained with linearly and circularly polarized soft x rays. *Phys. Rev. B*, 66:184404, Nov 2002.

[157] D. Franta. Symmetry of linear dielectric response tensors: Dispersion models fulfilling three fundamental conditions. *Journal of Applied Physics*, 127(22), 06 2020. 223101.

List of publications

- Antonio Caretta, **Simone Laterza**, Valentina Bonanni, Rudi Sergo, Carlo Dri, Giuseppe Cautero, Fabio Galassi, Matteo Zamolo, Alberto Simoncig, Marco Zangrando, Alessandro Gessini, Simone Dal Zilio, Roberto Flammini, Paolo Moras, Alexander Demidovich, Miltcho Danailov, Fulvio Parmigiani, and Marco Malvestuto, *A novel free-electron laser single-pulse wollaston polarimeter for magnetodynamical studies*, Structural Dynamics, 8(3):034304 (2021)

- Marco Malvestuto, Antonio Caretta, Richa Bhardwaj, **Simone Laterza**, Fulvio Parmigiani, Alessandro Gessini, Matteo Zamolo, Fabio Galassi, Rudi Sergo, Giuseppe Cautero, Miltcho Boyanov Danailov, Alexander Demidovic, Paolo Sigalotti, Marco Lonza, Roberto Borghes, Adriano Contillo, Alberto Simoncig, Michele Manfredda, Lorenzo Raimondi, and Marco Zangrando, *The MagneDyn beamline at the FERMI free electron laser*, Review of Scientific Instruments, 93(11):115109 (2022)

- **Simone Laterza**, Antonio Caretta, Richa Bhardwaj, Roberto Flammini, Paolo Moras, Matteo Jugovac, Piu Rajak, Mahabul Islam, Regina Ciancio, Valentina Bonanni, Barbara Casarin, Alberto Simoncig, Marco Zangrando, Primož Rebernik Ribič, Giuseppe Penco, Giovanni De Ninno, Luca Giannessi, Alexander Demidovich, Miltcho Danailov, Fulvio Parmigiani, and Marco Malvestuto, *All-optical spin injection in silicon investigated by element-specific time-resolved kerr effect*, Optica, 9(12):1333–1338 (2022)

- Piu Rajak, Regina Ciancio, Antonio Caretta, **Simone Laterza**, Richa Bhardwaj, Matteo Jugovac, Marco Malvestuto, Paolo Moras, and Roberto Flammini, *Evidence of silicide at the Ni/β-Si$_3$N$_4$(0001)/Si(111) interface*, Applied Surface Science, 623:156986 (2023)

- **Simone Laterza**, Antonio Caretta, Richa Bhardwaj, Paolo Moras, Nicola Zema, Roberto Flammini, and Marco Malvestuto, *Harnessing the magnetic proximity effect: induced spin polarization in Ni/Si interfaces*, submitted

Acknowledgements

This thesis would not have been possible without the kind support, patience and dedication of many people, to whom my warmest thanks are directed.

I thank my family, my sun, my moon and the sky that lies in between, for their presence in my highs and my lows.

I thank my friends: the laughs, the complicities, the memorable times shared in cultivating friendship brought pure joy in my life.

I thank the MagneDyn group, Marco, Antonio and Richa, for offering valuable perspectives on the magnetic dynamics and for guiding my critical discernment in the correct path. I especially thank Marco for his mentoring, encouragement and incitement during my research, and Antonio for our many productive conversations and for envisioning, designing and operating the TONIX polarimeter, without which nothing in this work would have been achieved.

Thanks to Marco Battiato for providing the scientific case and for the useful insights on the spin injection topic.

Thanks to Roberto Flammini, Matteo Jugovac (VuV beamline) and Paolo Moras (CNR-ISM) for devising and then realizing the samples at the core of this work.

Thanks to Piu Rajak, Mahabul Islam and Regina Ciancio (CNR-IOM) for providing the expertise and the means to perform the characterization of the interfaces.

Thanks to Nicola Zema (CiPo beamline) for the involvement and the support with the XMCD measurements.

Thanks to the FERMI team, whose contribution to the success of the experiments at MagneDyn in these last three years gave me the opportunity to accomplish my research project.

Thanks to Valentina, Barbara, Roberta and all the actors who were involved in the MagneDyn collaboration, and to all the users who visited MagneDyn during these years, for providing insightful inspirations during my learning journey.